Materials & Design 234 (2023) 112356

Contents lists available at ScienceDirect

Materials & Design

journal homepage: www.elsevier.com/locate/matdes

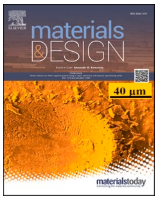

Additive friction stir deposition of metallic materials: Process, structure and properties

Jiayun Shao [a], Arash Samaei [a], Tianju Xue [b], Xiaoyu Xie [a], Shengmin Guo [c], Jian Cao [a], Eric MacDonald [d,e], Zhengtao Gan [d,*]

[a] Department of Mechanical Engineering, Northwestern University, Evanston 60208, IL, USA
[b] Department of Civil and Environmental Engineering, The Hong Kong University of Science and Technology, Clear Water Bay, Hong Kong SAR, China
[c] Department of Mechanical and Industrial Engineering, Louisiana State University, Baton Rouge 70803, LA, USA
[d] Department of Aerospace and Mechanical Engineering, The University of Texas at El Paso, El Paso 79968, TX, USA
[e] Manufacturing Science Division, Oak Ridge National Laboratory, 37831 TN, USA

ARTICLE INFO

Keywords:
Additive manufacturing
3D printing
Grain growth
Metallic materials
Defects
Friction-based manufacturing

ABSTRACT

Additive friction stir deposition (AFSD) is a relatively new additive manufacturing technique to fabricate parts in solid state below the melting temperature. Due to the solid-state nature, AFSD benefits from lower residual stresses as well as significantly lower susceptibility to porosity, hot-cracking, and other defects compared to conventional fusion-based metallic additive manufacturing. These unique features make AFSD a promising alternative to conventional forging for fabricating large structures for aerospace, naval, nuclear, and automotive applications. This review comprehensively summarizes the advances in AFSD, as well as the microstructure and properties of the final part. Given the rapidly growing research in AFSD, we focus on fundamental questions and issues, with a particular emphasis on the underlying relationship between AFSD-based processing, microstructure, and mechanical properties. The implications of the experimental and modeling research in AFSD will be discussed in detail. Unlike the columnar structure in fusion-based additive manufacturing, fully dense material with a fine, fully-equiaxed microstructure can be fabricated in AFSD. The as-wrought structure brings the as-printed parts with comparable properties to wrought parts. The fundamental difference between AFSD and fusion-based metallic additive manufacturing will be summarized. Furthermore, the existing challenges and possible future research directions are explored.

1. Introduction

Unlike conventional subtractive material technologies, additive manufacturing (AM) is founded on a novel philosophy known as “material increment”, enabling the design and production of intricate and customized metallic components without the constraints of traditional processing techniques. Metal AM is now widely recognized as a new paradigm for designing and manufacturing high-performance components for a variety of applications in aerospace, automotive, medical, and energy industries [1]. Several metal additive manufacturing techniques, such as Binder Jetting, Directed Energy Deposition (DED), Laser Powder Bed Fusion (LPBF), Sheet Lamination, and Material Extrusion, have been used to create parts for various applications that differ in terms of system configuration, power resource, and the processing approach. Most of these techniques are receiving considerable attention because of process flexibility, and a diversity of applications.

Yet, there are major limitations that prevent these AM techniques from being widely adopted in industry, including the need for a sealed chamber in LPBF, limited build volume, defect controllability, scalability, and a limited range of materials. In addition, AM techniques that use laser and electron beam as a power source for in situ melting of materials result in major defects (e.g., porosity and cracks) in the final part due to rapid cooling and resolidification of the melt pools [1–3]. The crack formation problem limits the number of printable metals and alloys that prevents metal-AM from reaching its full potential [4].

Friction-based additive manufacturing techniques have recently been introduced to print metallic materials in solid state without the need for melting and solidification. The material range for printing is expanded and the production of nearly crack- and pore-free parts for a variety of applications is enabled [5]. These techniques are divided into

---

* Corresponding author.
E-mail address: zgan@utep.edu (Z. Gan).

https://doi.org/10.1016/j.matdes.2023.112356
Received 17 July 2023; Received in revised form 18 September 2023; Accepted 23 September 2023

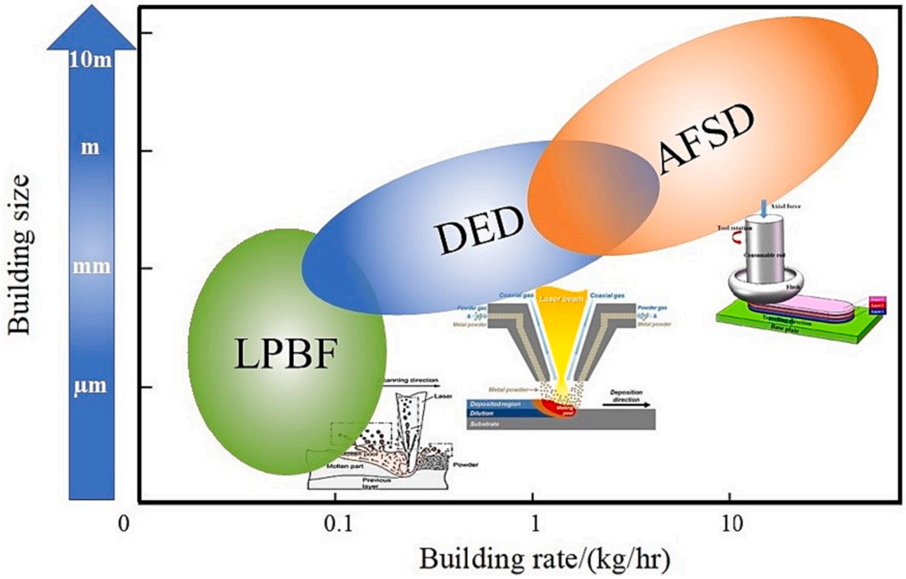

Fig. 1. Comparison of the building size and building rate between fusion-based and friction-based AM technologies. The data used here is a generic representation of literature. The inset schematics are associated with LPBF, DED, and AFSD from bottom to top, respectively [8–10].

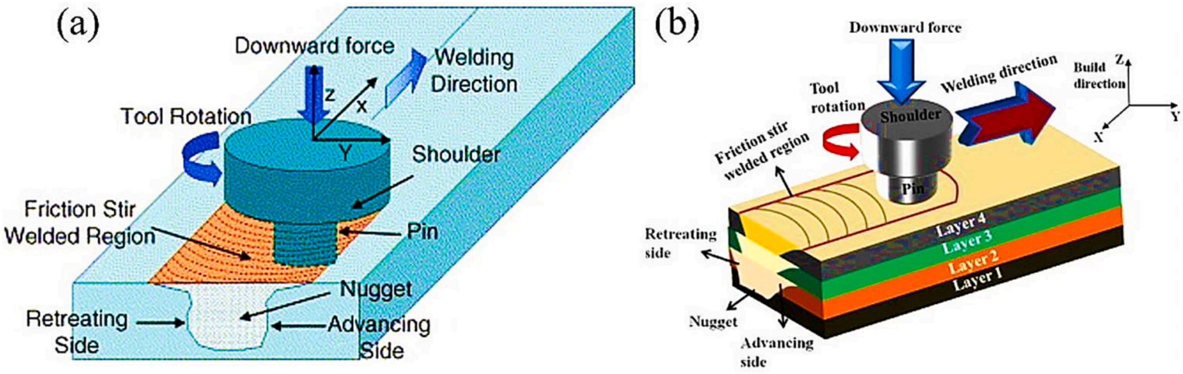

Fig. 2. Schematic drawing of two processes: (a) FSW [23] and (b) FSAM [24].

two main categories: friction stir additive manufacturing (FSAM) and additive friction stir deposition (AFSD). While FSAM is a hybrid process that requires both additive and subtractive steps to fabricate the components, AFSD, the focus of this review, is purely additive.

Aeroprobe Corporation (now MELD Manufacturing) [6,7] developed and patented AFSD, which combines the friction stirring concept with a material feeding process to fabricate site-specific components [5]. AFSD, as a solid-state, low-temperature AM technique, has several advantages over fusion-based AM. This technique operates in an open environment without a chamber or a powder bed system, resulting in no size limit for the final structure bounding volume. Furthermore, AFSD equipment, which is similar to traditional CNC and milling machines, can be scaled up as required. Both characteristics make AFSD a suitable choice for large-part fabrication. Unlike other AM technologies, AFSD typically does not require any additional post-processing such as hot isostatic pressing (HIP), reducing production time and energy use.

In contrast to the columnar grains resulting from fusion-based AM caused by rapid melting and solidification, fine and full-equiaxed microstructure can be obtained using AFSD, allowing for the printing of isotropic components. Another advantage of AFSD is the dramatically improved building rate. Fig. 1 depicts a comparison of building size and building rate between AFSD and laser additive manufacturing. AFSD can deposit material more than ten times faster than other AM processes.

Despite all of the benefits listed above, AFSD is still in its early stages. AFSD was first patented in 2014 [6] and has been in use for less than ten years, with growing interest in research of AFSD for creating defect-free parts. Several reviews are available about friction stir additive manufacturing [11–16] with focus on its market, innovations, potential, tooling and design strategies. An in-depth review on processes, microstructure and properties is needed. Also, as this technology is under rapid development, a periodic update of our understanding is needed. This review focuses on the AFSD of metallic materials, specifically the processes, microstructure, and properties of manufactured components. The distinctions between AFSD and fusion-based additive manufacturing will also be discussed to understand the relative current state of the technique and potential for future applications. The aim of the present review is to promote the application of AFSD and bridge the gap between the academia and industrial practices.

2. Process

The AFSD technique combines the friction stir concept with a material feeding process to additively manufacture metal components at low temperatures [17]. There are also other names for AFSD in literature including MELD (named after the corporation) [18], additive friction stir (AFS) [19], friction stir fabrication (FSF) [6], friction stir metal deposition (FSMD) [20], friction deposition (FD) [21], friction surfacing additive manufacturing [10], and friction stir deposition (FSD) [22].

The AFSD approach shows great potential for fabricating large-scale (in meters), crack-free metallic components with fully-equiaxed microstructure. Yet, a thorough understanding of AFSD and effective process parameters is imperative to fabricate metallic structures with the desired geometries and properties. This fundamental knowledge is critical for understanding the underlying physical mechanisms and the origin of defects. This section introduces AFSD processes, with a focus on defects, potential defect mechanisms, and remedies.

2.1. *Classification*

To the best of our knowledge, we have not found a standard for categorizing AFSD processes. In this section, we did our best to identify and categorize all of the published AFSD processes.

In contrast to friction stir welding (Fig. 2(a)) [23] and friction stir additive manufacturing (Fig. 2(b)) [24], AFSD does not use a solid pin tool or probe. Instead, key components that generate friction heat are a rotating hollow shoulder of the system or the feedstock material rod itself. The AFSD processes are classified into two types based on these configurations: those that use a hollow tool and those that use the feedstock rod itself as a tool. As shown in Fig. 3, the feedstock material is delivered through the hollow shoulder and rotates with the tool during the AFSD process. Dynamic contact friction generates frictional heat at the tool-material and material-substrate interfaces, raising the temperature of the feedstock material and tool [17]. The feedstock material softens as the temperature rises, promoting plastic deformation. The heat generated by the plastic deformation of the feedstock material and the substrate also facilitates solid-state material bonding. Metallic components with tailored geometrical properties are manufactured through the continuous flow of feedstock material and motion along the predefined scanning path. In order to promote material deformation, a protrusion is added to the bottom of the tool [7], surrounding the feeding inlet in the shape of radiation (Fig. 4(a)), helix (Fig. 4(b)), circle (Fig. 4(d, e)), or others (Fig. 4(c, f, g)). The tools used in this process are cylindrical and conical. Specifically, in order to fabricate tubes, a hollow tool with a hollow cylindrical punch is used (Fig. 5), and this process is also known as friction-forging tubular additive manufacturing (FFTAM) [25].

As shown in Fig. 6, the alternative AFSD approach includes a rotating consumable rod pushed out under the exerted axial force in the AFSD process without a hollow cylindrical tool. Friction and plastic deformation are heat generation mechanisms, similar to the AFSD process with a tool. A further distinction can be made based on the shape of the feedstock material, which includes the cavity of the hollow tool as well as the feedstock itself. The filler can be circular, square, or elliptical in shape. Without the use of a tool, circular feedstock material is typically used. The main difference is that in the AFSD process without a tool, the feedstock material is not constrained by the hollow shoulder, resulting in severe flash defects, as discussed in Section 2.4.

The feedstock materials can be introduced in different forms including powder, rod, and recycled chips in an AFSD process, as shown in Fig. 7. Furthermore, the feedstock rod for AFSD can be obtained by

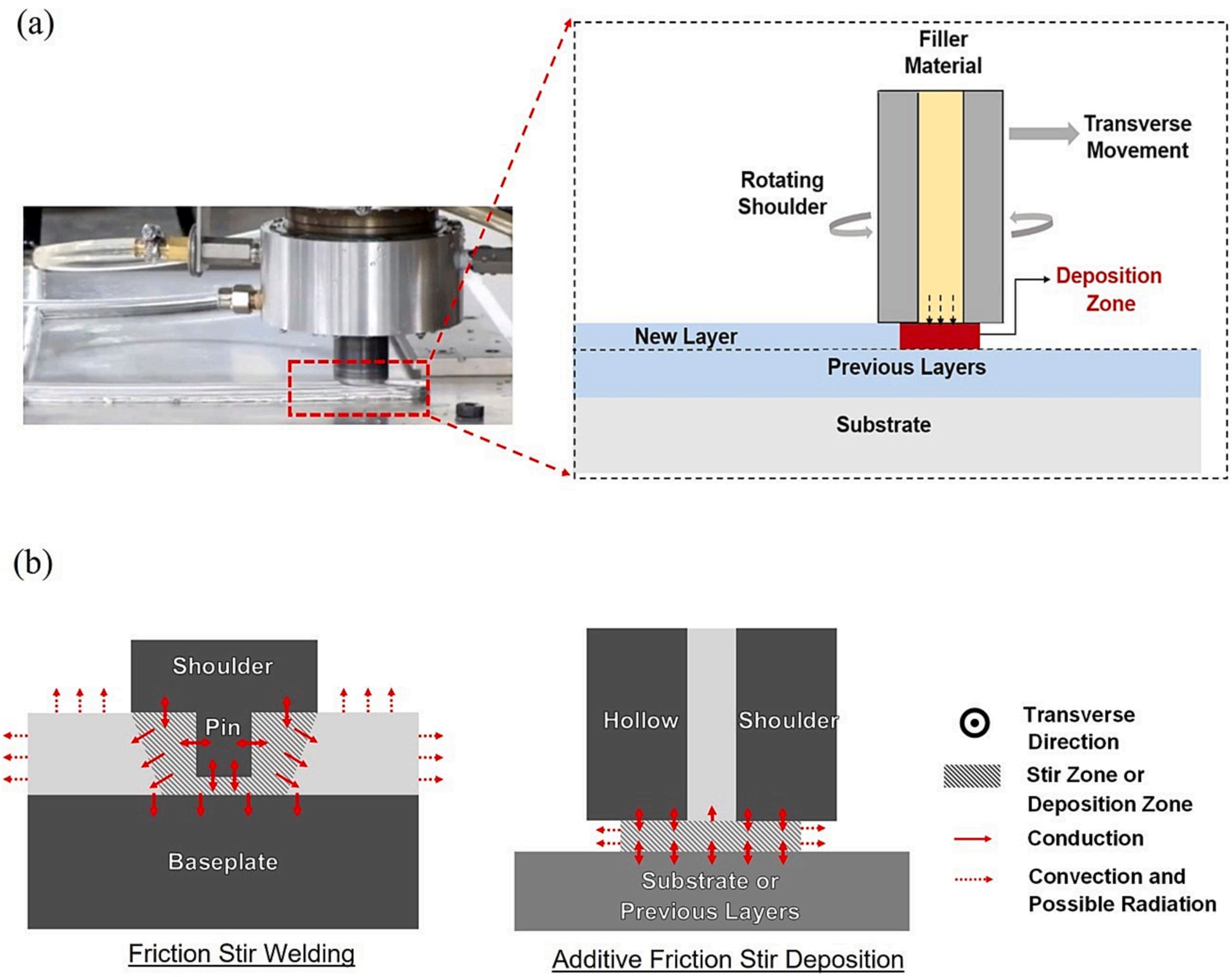

Fig. 3. (a) A picture showing AFSD equipped with a hollow tool and an illustrative diagram highlighting some fundamental physical processes in the local region of deposition. (b) A comparison of thermal boundary conditions between FSW and AFSD [17].

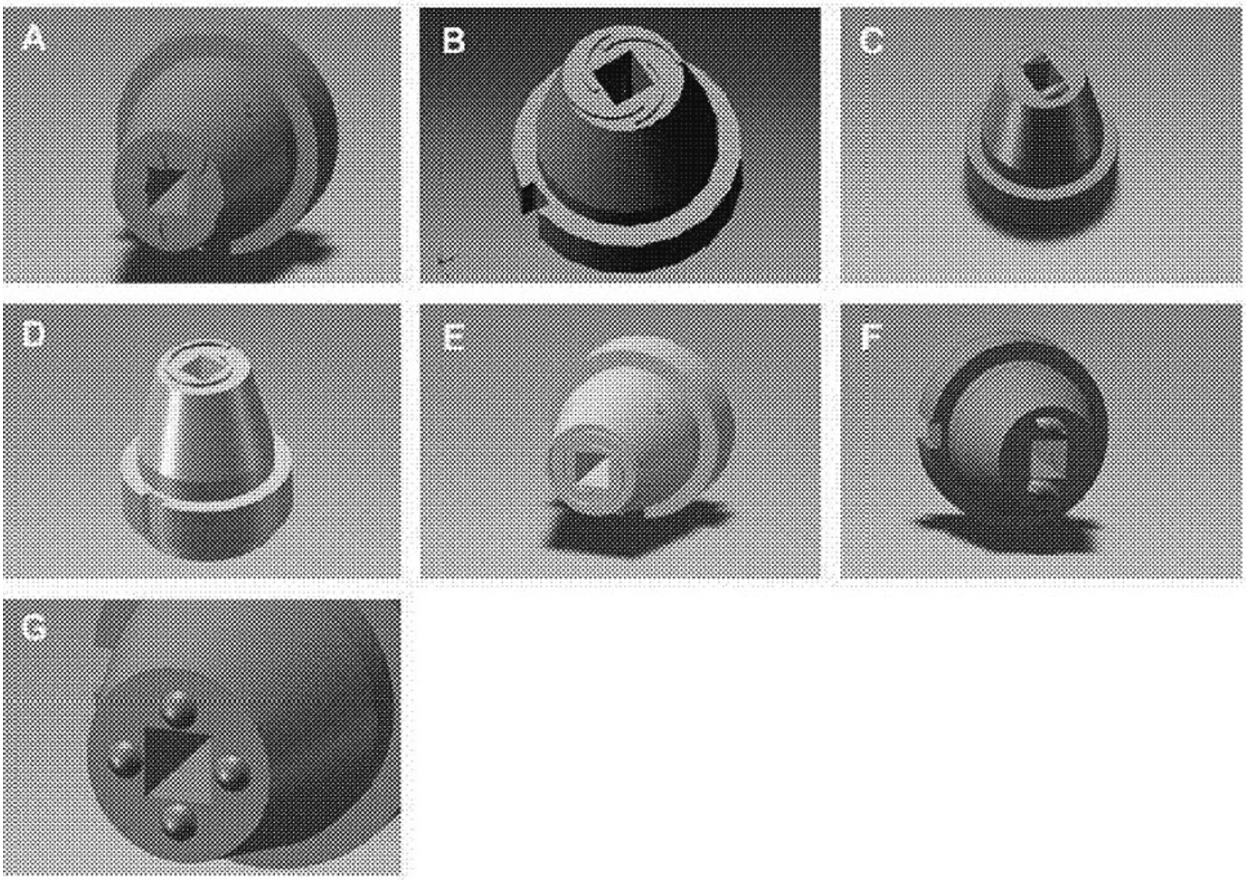

Fig. 4. Different protrusion shapes in AFSD with a hollow tool [7].

compacting the metal chips into the feedstock dimensions, according to [27]. Powder is another common form of feedstock material in AFSD. Metal matrix composites are typically created with matrix and reinforcement powders [5]. Only the AFSD process with a hollow tool can be adapted in this case. Another feedstock material combination is rod with reinforcement powder [22].

2.2. Materials

The printable alloys from the AFSD processes are essentially limitless due to the solid-state nature of the process, and any wrought or cast alloy can be used as a feedstock material. Although this process is still in its early stages, quite a few metallic materials - aluminum alloys, titanium alloys, magnesium alloys, copper alloys, nickel alloys, and steels - have been reported to be manufactured by AFSD.

One of the most significant advantages of AFSD over fusion-based AM is the ability to produce non-weldable alloys. Many aluminum alloys are highly-crack-susceptible in fusion-based AM processes due to their high reflectivity and large solidification interval [4]. AFSD has enabled the fabrication of crack-free aluminum alloys. AA6061 [28], Al-Mg-Si [29], Al-Si [30] and AA7075 alloys [31] have been successfully manufactured through this technique; no cracks or pores in these samples are present, and the substrate and manufactured materials have a strong metallurgical bond. Aluminum alloys with reinforced particles are also successfully manufactured, including Al-SiC, AA6061-Mo, AA6061-W [5], and Aluminum matrix nano Al_2O_3 composites [22]. Aluminum and magnesium alloys are both lightweight with many physical properties in common. The AFSD process also produced defect-free magnesium parts with full density, such as AZ31 [28] and WE43 [32] alloys.

In addition to lightweight alloys, superalloys such as nickel alloys and titanium alloys are manufactured using AFSD. As illustrated in Fig. 8 (a), a well-bonded, 40-layered Inconel 718 sample was manufactured. Another nickel superalloy used in AFSD is Inconel 625 [33]. A Ti-6Al-4 V sample has been fabricated from recycled metal chips using AFSD and is completely dense with no visible cracks, as shown in Fig. 8(b) [27]. Other materials fabricated using AFSD techniques include pure copper [29,34] and steels [20,35]. Steels such as SS304 [20] and mild steel [35] have been reported to be used in AFSD. Alloys used in friction stir welding, such as Cu-Zn alloy [36] and mild steel [37], can also be potentially used as feedstock material in AFSD.

2.3. Heat and deformation mechanisms in AFSD process

The AFSD process involves three processing stages: (1) depositing preparation, (2) initial deposition, and (3) steady-state deposition, as shown in Fig. 9. Prior to deposition, the tool/rod moves downward at a very low feeding rate and a high rotation rate. Due to frictional heating, the feed-rod reaches an elevated temperature shortly after contacting the substrate. Once the required temperature is reached, the second stage begins. At this point, the tool is raised to the height that defines the deposition layer thickness and then translated in-plane along a predefined path. Deposition begins with the continuous extrusion of the feed rod and transverse motion. At this stage, severe plastic deformation and contact friction are initiated. The steady-state deposition process begins once the actuation force and torque have stabilized. Similar to the second stage, in the third stage, heat is generated by contact friction and plastic deformation.

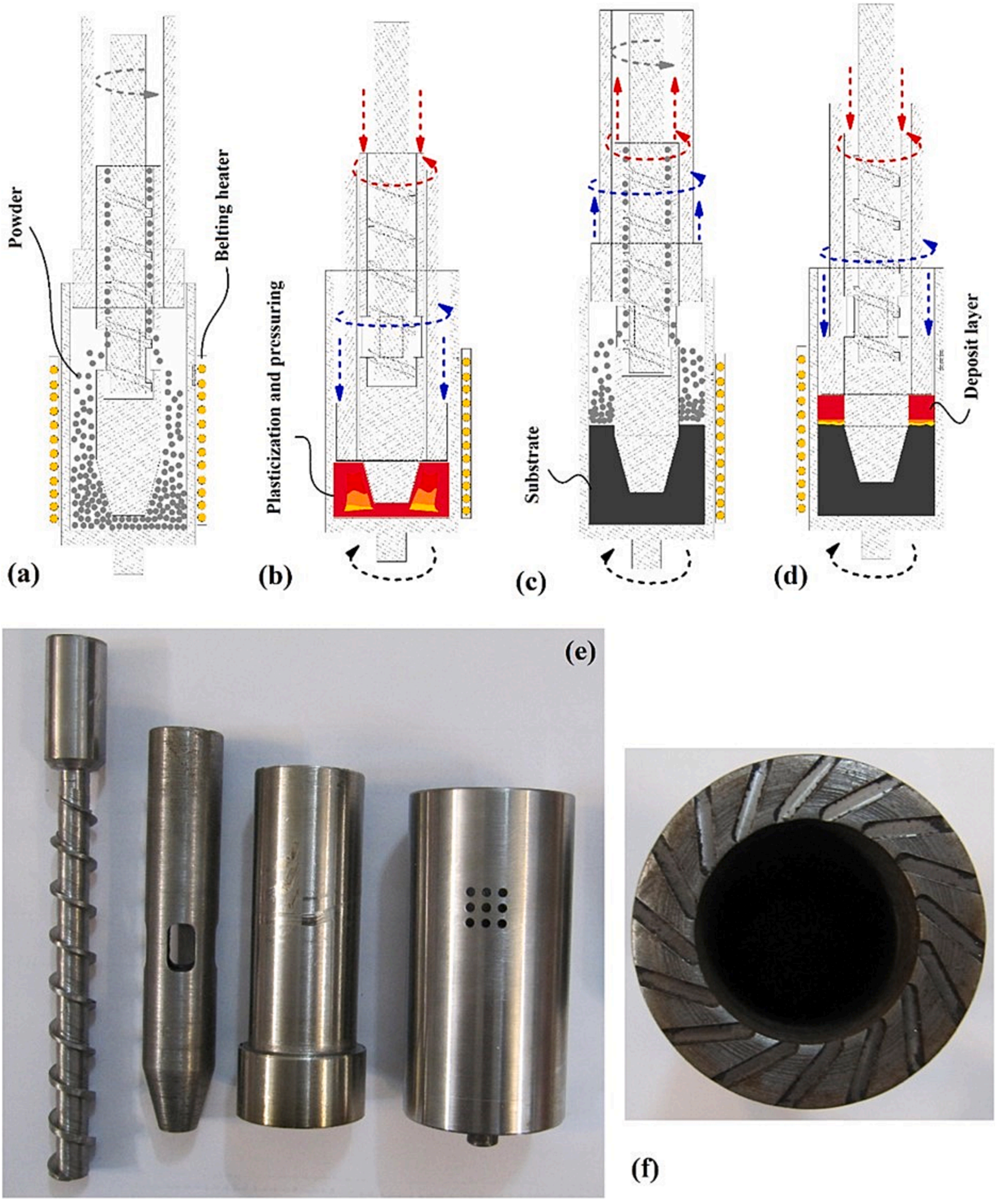

Fig. 5. (a-d) Schematic representation of different processing stages for FFTAM technology: (a) introduction of metal chips, (b) friction-forging consolidation of the first layer, (c) continuing the deposition process by feeding the next layer required chips, and (d) subsequent deposition of the new layer. (e) Different parts of the FFTAM tool. (f) Cross-section of a FFTAM shoulder [7].

During the steady-state deposition step, the as-deposited morphology and microstructure, as well as subsequent properties, are highly dependent on temperature evolution and deformation behaviors. Heat generation in AFSD has a strong influence on temperature evolution. Interfacial friction and plastic deformation produce heat during this process. The heat generated by plastic deformation is often referred to as volumetric heat generation, which is dependent on the shear strain rate and shear stress at yielding [39].

It has been reported that frictional heat accounts for 54.4 % of the overall heat produced by friction stir engineering [40]. However, others argue that this proportion varies with different processing stages and materials [41]. This proportion is thought to be strongly related to the

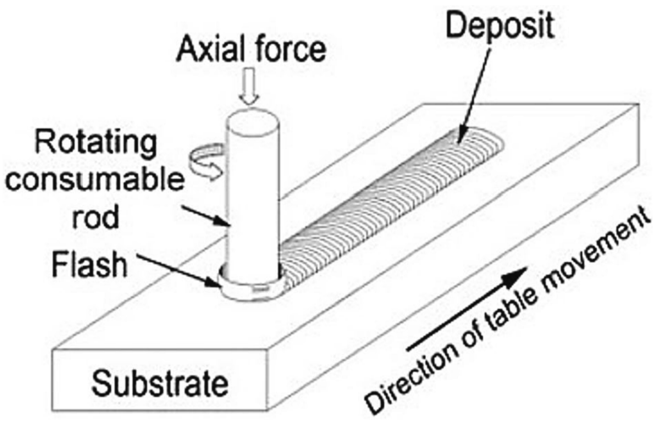

Fig. 6. Schematic diagram showing the processing of an AFSD system without a hollow cylindrical tool [26].

interfacial contact states (or conditions) between the material and the tool head. There are three main types of contact conditions: full sticking, partial sticking and partial slipping, and full slipping.

The fractional slip, $\delta(r)$, specifically denoting the spatially variable fractional slip, is frequently used to quantify these three conditions, while $1 - \delta(r)$ is the sticking coefficient [42]. $1 - \delta(r)$ is expected to decrease along the radial direction due to the linear velocity of the tool head increasing as r increases, causing difficulties for the deposited material to maintain sufficient deposition. When $1 - \delta(r) = 1$, the contact condition is full sticking, and when $1 - \delta(r) = 0$, the contact condition is full slipping.

It has been reported that $1 - \delta(r)$ strongly depends on the material [43]. As illustrated in Fig. 10, the sticking coefficient (Fig. 10(e)) difference between Cu and Al-Mg-Si is deduced from the experimental observations of deformation behaviors along the radial direction (Fig. 10 (c) and (d)). This difference in $1 - \delta(r)$ results in different heat generation mechanisms in different zones, as shown in Fig. 11. The Cu system has the most significant volumetric heat generation directly beneath the feed rod, whereas the Al-Mg-Si system has a large volumetric heat generation zone due to significant material flow. Fig. 11 appears to underestimate the heat generation at the feedstock rod/substrate interface. This lack of reconciliation calls for closer collaborations between computational scientists and experimentalists.

The results of in situ temperature monitoring (Fig. 12) demonstrate the impact of different heat generation mechanisms in these two materials. T_{peak} for successful Cu depositions is in the range of 49 % ~ 79 % of the melting temperature (T_M), while T_{peak} for successful Al-Mg-Si depositions is in the range of 76 % ~ 92 % of T_M. Further studies have revealed that T_{peak} has a power law relationship with Ω/V in Cu but with Ω^2/V in Al-Mg-Si while Ω is the rotation rate and V is the in-plane velocity. The exposure time, heating rate, and cooling rate for AFSD are approximately on the order of 10^1 s, $10^1 \sim 10^2$ K/s, and 10^1 K/s, respectively [43]. Other researchers have stated that T_{peak} in the range of 60 % ~ 90 % of T_M guarantees successful deposition for FSW of steels [44].

While difficulties exist to experimentally monitor the temperatures inside the deposition, numerical simulation efficiently provides insights. As shown in Fig. 13, the temperature contours for deposition under different process variables are simulated using a meshfree computational framework. In general, the processing temperature rises as the feeding rate increases. For the starved case in Fig. 13(a), the lower feed rate is insufficient to fill the deposition zone. The overfed case in Fig. 13 (c) raises the temperature, which may result in local melting of the deposition (detailed information can be found in Section 2.4). The reason why feeding rate strongly influences deposition appearance and substrate material properties is that the temperature evolution during the AFSD process is dependent on feeding rate results [45]. Others have used commercial CFD software to capture the thermal characteristics at the tool-substrate interface [46]. The results show that the highest temperature occurs near the cladding/processing zone at the tool-substrate interface, and significant thermal gradients exist in proximity.

In addition to the temperature evolution, deformation behaviors have a significant impact on the success of deposition in the AFSD process. The different deformation behaviors at different stages of the AFSD process are studied using X-ray computed tomography. As shown in Fig. 14, at least two strain components at the initial material feeding have been identified, which are the (1) extrusion strain due to compression force and (2) torsional strain due to the rotation rate gradient along the material feeding direction. Extrusion strain causes cross-sectional area changes, while torsion strain results in the helix shape shown in Fig. 14(f). At steady state, the millimeter-scale cylinder transforms into ~ 10 μm micro-ribbons, as shown in Fig. 15. These micro-ribbons indicate a significant thinning process caused by large shear deformation [38].

Plastic strain contours (Fig. 16) have been simulated to demonstrate material mixing and deformation behaviors. The results show that insufficient deformation caused by low feeding rate (Fig. 16(a)) correlates to the experimentally observed surface voids/galling [45]. Consequently, feeding rates above the optimal threshold (Fig. 16(c)) would not promote material mixing, but conversely, would result in waste due to excessive flashing [45]. The plastic strain simulated is on

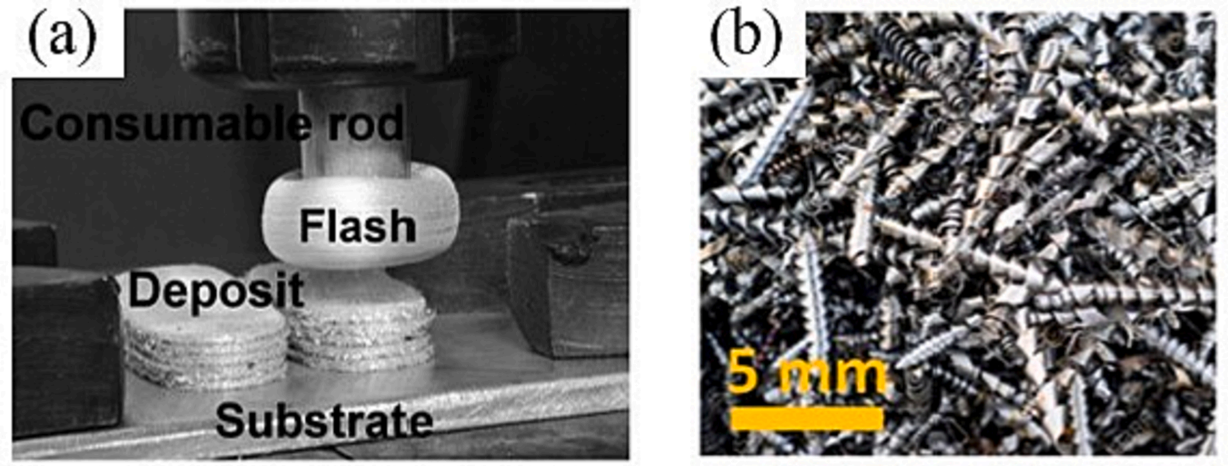

Fig. 7. Feedstock material forms for the AFSD-based processing: (a) material rod [26], (b) machine chips.

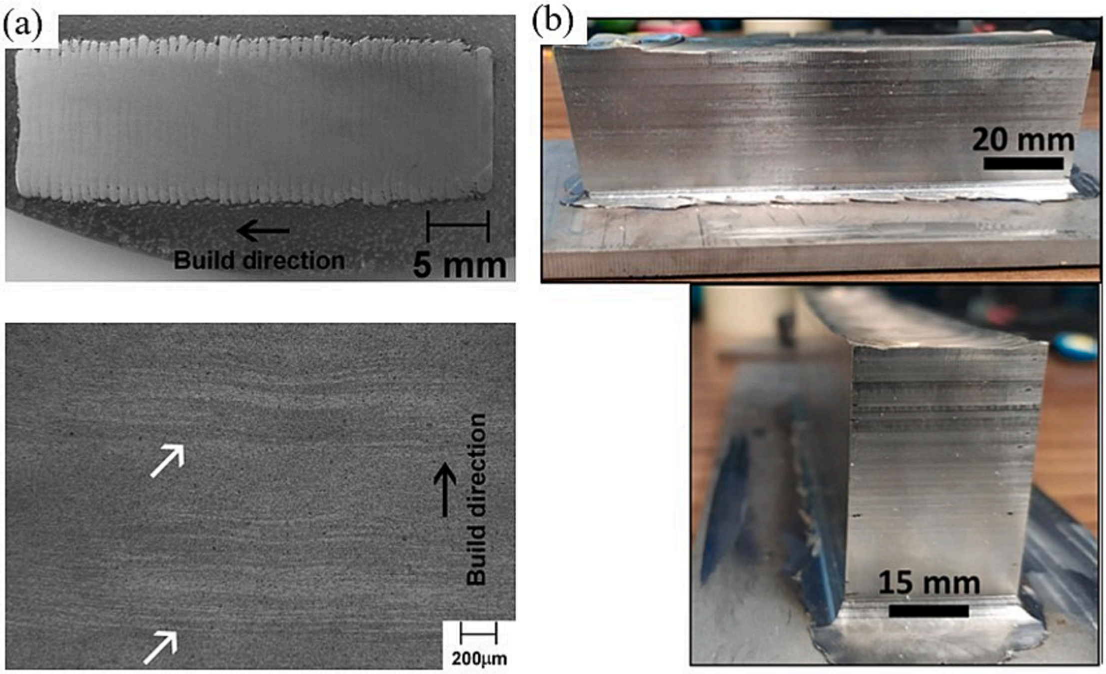

Fig. 8. Parts built of different materials using AFSD. (a) A macrograph of the Inconel 718 deposit (longitudinal and building direction), containing more than 40 layers and demonstrating excellent layer bonding with white arrows indicating layer interfaces [33]. (b) Ti-6Al-4 V built part with dimensions of 30 *mm* × 135 *mm* × 25 *mm* with no obvious defects [27].

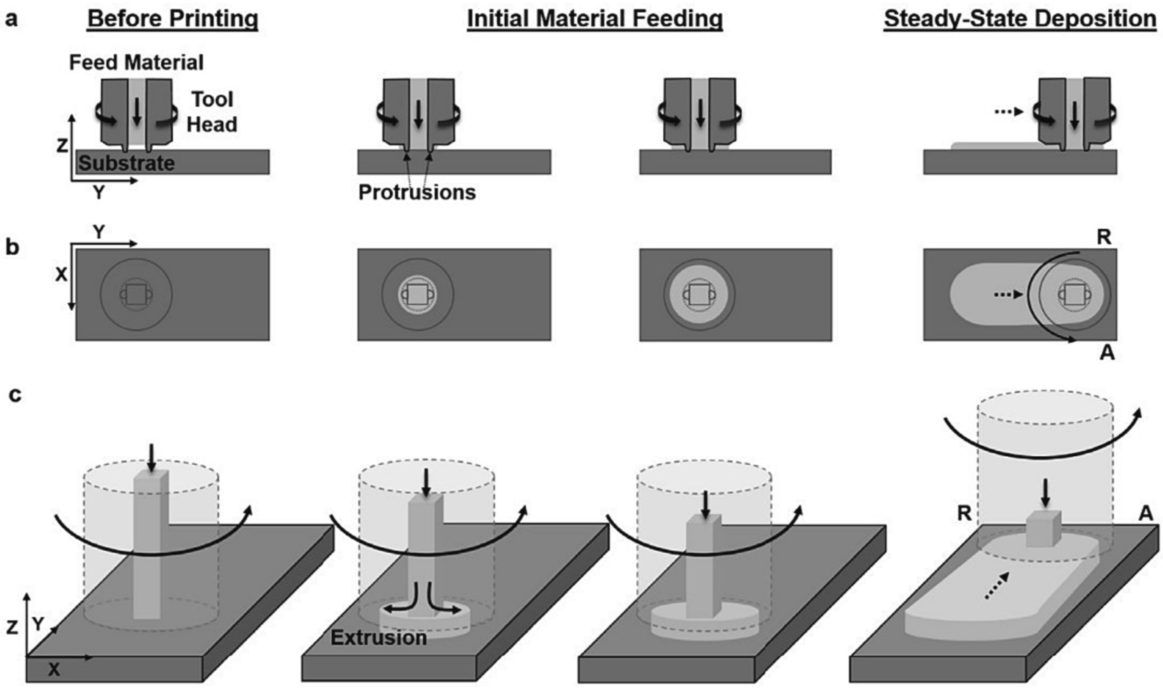

Fig. 9. Schematic diagrams showing the main AFSD processing steps (from left to right): before processing, initial material feeding, and steady-state deposition. This includes (a) side view, (b) top view, and (c) isometric view [38].

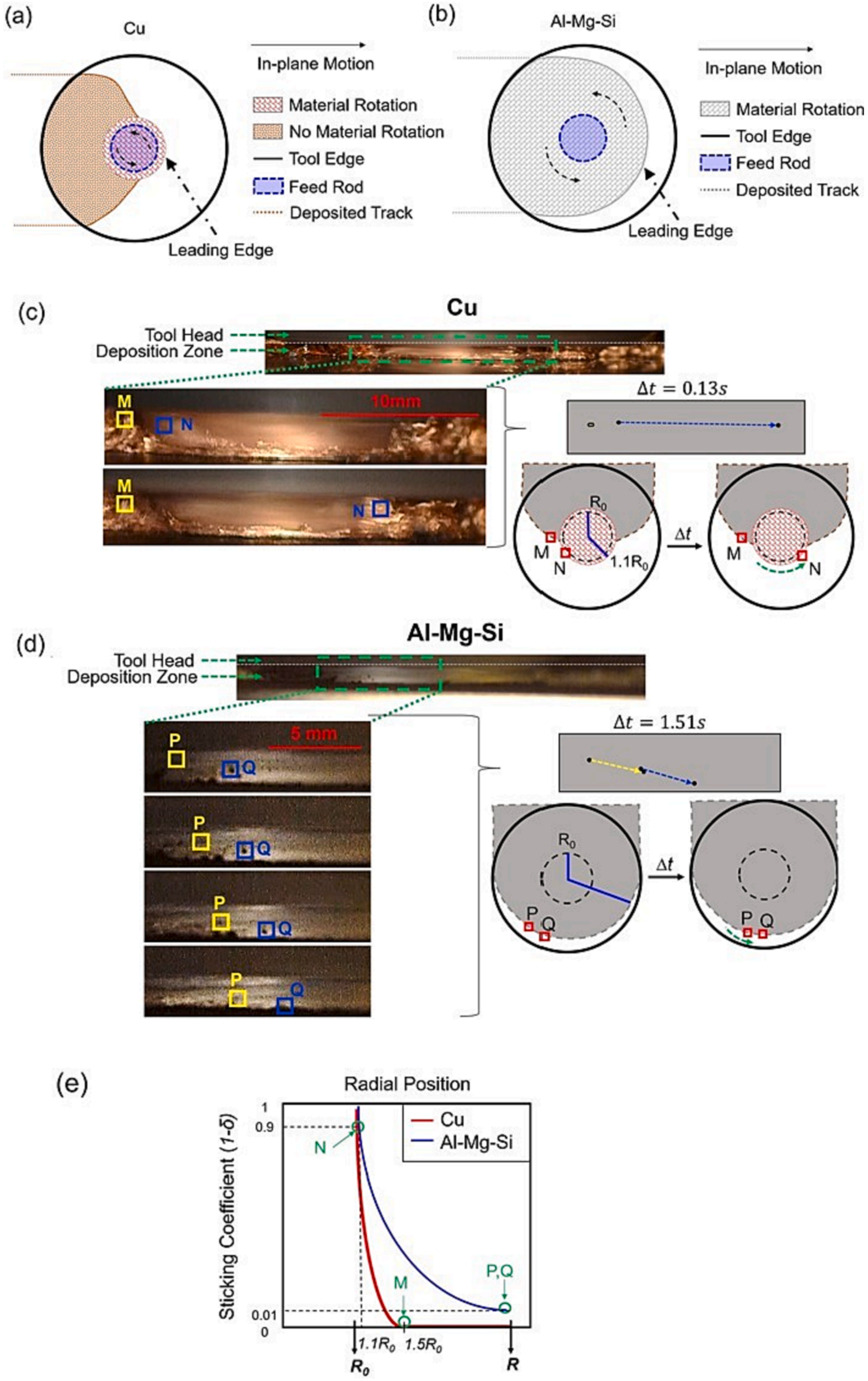

Fig. 10. Material flow features observed with (a) Cu and (b) Al-Mg-Si deposition footprints. Material flow snapshots for (c) Cu and (d) Al-Mg-Si at 300 RPM and 2 mm/s in-plane velocity. The Cu snapshots show two distinct regions where Point M remains stationary while Point N rotates with the tool head. The Al-Mg-Si snapshots show the entire deposition zone rotating. (e) A diagram illustrating the differences in the observed sticking coefficient as a function of radial position between Cu and Al-Mg-Si [43].

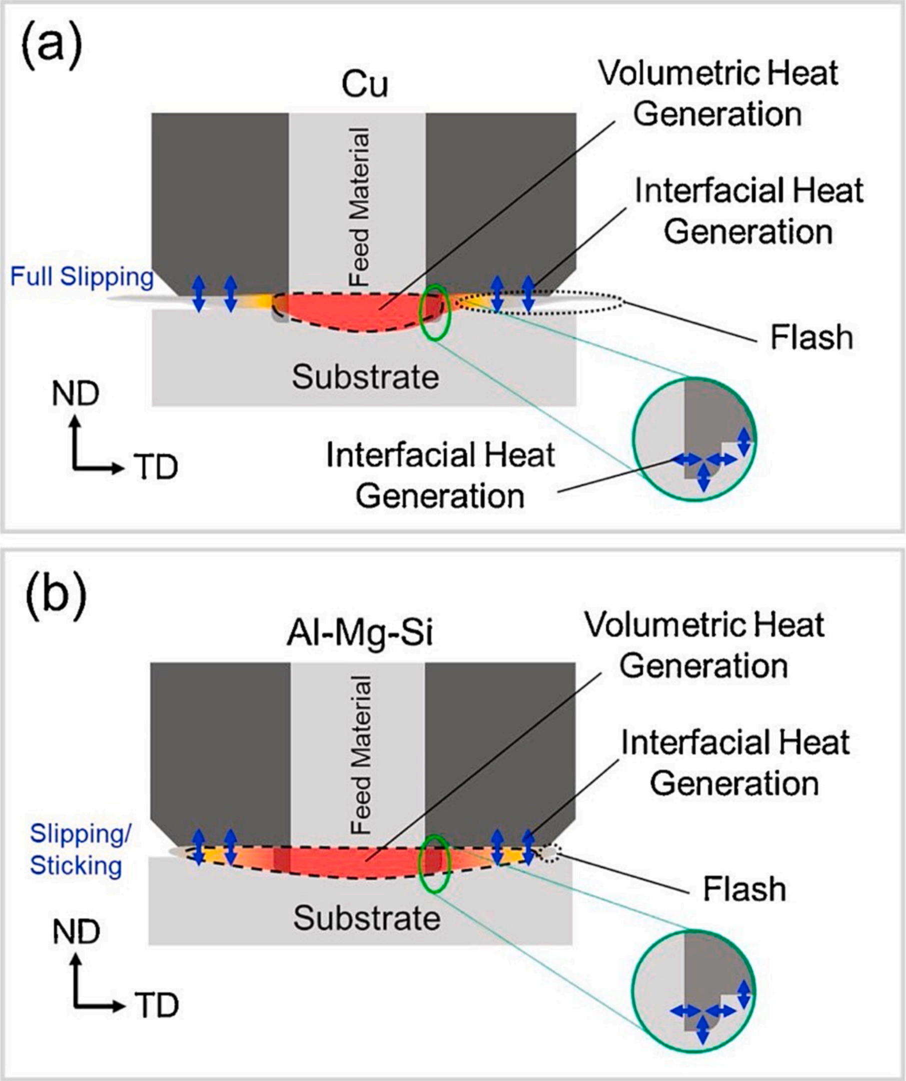

Fig. 11. A schematic illustration of the heat generation mechanisms for (a) Cu and (b) Al-Si-Mg. The regions of volumetric heat generation are highlighted in red, and the regions of interfacial friction are highlighted in blue arrows [43].

the order of ~ 100. According to other simulations [47], the velocity beneath the tool is on the order of ~ 100 mm/s, which is comparable to traditional friction stir welding [48,49].

2.4. Defects

2.4.1. Low dimensional accuracy

Despite the fact that AFSD has many advantages with regard to the manufacturing of large-scale components, dimensional accuracy, including surface roughness, has been a major issue. Currently, nearly all manufactured components require post-CNC machining [35]. Several samples prepared using the AFSD process are shown in Fig. 17. Whether a single-layer and single-track sample (Fig. 17(a)), a single-layer and multi-track sample (Fig. 17(b)), a multi-layer and single-pass sample (Fig. 17(c)), multi-layer and multi-pass samples in cross (Fig. 17(d)) or cylindrical shapes (Fig. 17(e)), all prepared samples have rough surfaces and post-machining steps are required to meet application requirements.

The main cause of surface roughness along the building direction is flash. As illustrated in Fig. 18, the material flows rotationally and laterally during material deposition. Excess flash at the edge of the tool/rod is formed when excess feed material exits the deposition zone and weakly bonds with the substrate of the previously deposited material [29]. Under similar processing conditions, the flash in the Cu sample (Fig. 18(b)) is more severe than the flash in the Al-Mg-Si sample (Fig. 18(a)). According to in-situ observations of material flow behaviors [43], this is because rotational motion is rare in the Cu deposition zone, characterizing the tool-material interface as the full slipping condition. While the exterior surface of Al-Mg-Si is seen to rotate with the tool, this suggests that some slipping/sticking at the tool-material interface exists.

Further investigation into the heat generation mechanisms indicates that the interfacial heat generation is limited in the deposition zone in Cu but is significant in the material-tool shoulder zone in Al-Si-Mg. The differences in material flow and thermal history between Cu and Al-Si-Mg result in different flash phenomena. The flash phenomenon accumulates layer by layer along the building direction, resulting in a weak bond and a rough surface, as shown in Fig. 19, which requires further machining. It is worth noting that the excess flash in AFSD is more controllable with a hollow tool. As illustrated in Fig. 20, compared with AFSD without a tool, the excess material flow under AFSD with a hollow tool is constrained by the tool shoulder, alleviating the flash phenomenon. Furthermore, whether in AFSD with a hollow tool (Fig. 21(a)) or in AFSD without a tool (Fig. 21(b)), the flash occurs at the bottom of the feedstock rod.

Other surface characteristics, such as an onion ring pattern, galling, surface scratch, and edge cracking, have a significant impact on the performance and dimensional accuracy of the parts. These are the other

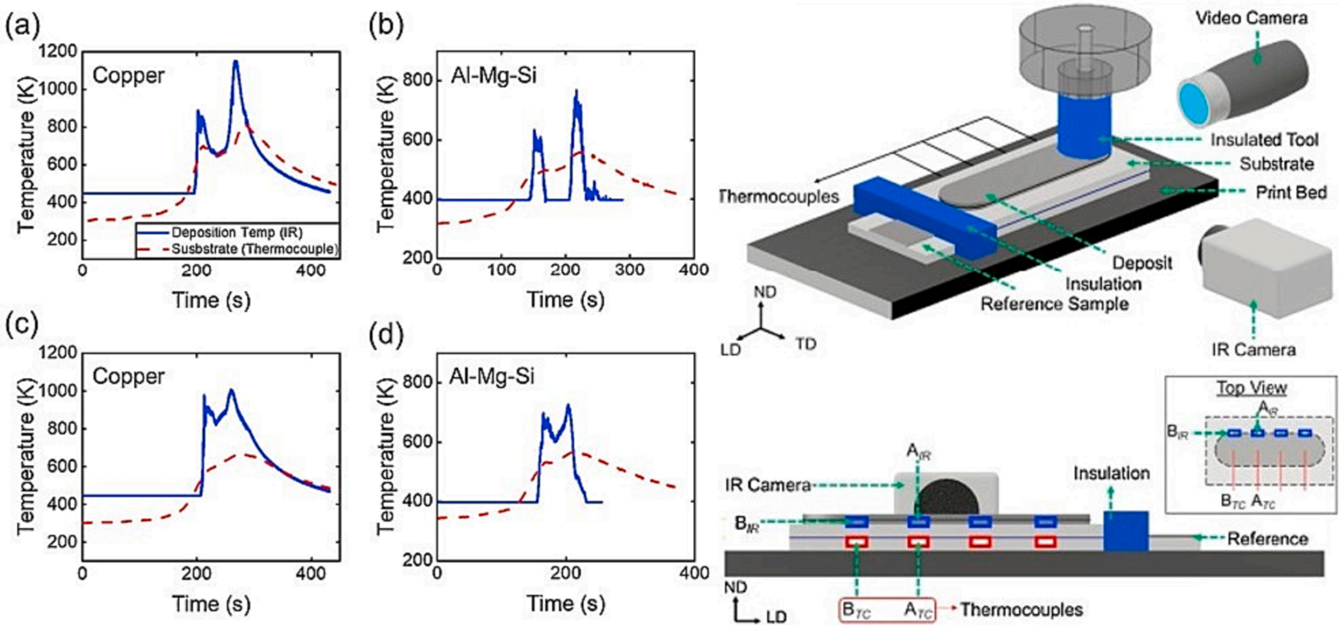

Fig. 12. Plots showing temperature as a function of time at spots A_{TC} and A_{IR} for (a) Cu at 300 RPM and 1 mm/s in-plane velocity and (b) Al-Mg-Si at 300 RPM and 2 mm/s in-plane velocity. Plots showing temperature as a function of time at spots B_{TC} and B_{IR} for (c) Cu and (d) Al-Mg-Si, respectively. The positions of A_{TC}, A_{IR}, B_{TC}, and B_{IR} are indicated on the schematic diagram on the right [43].

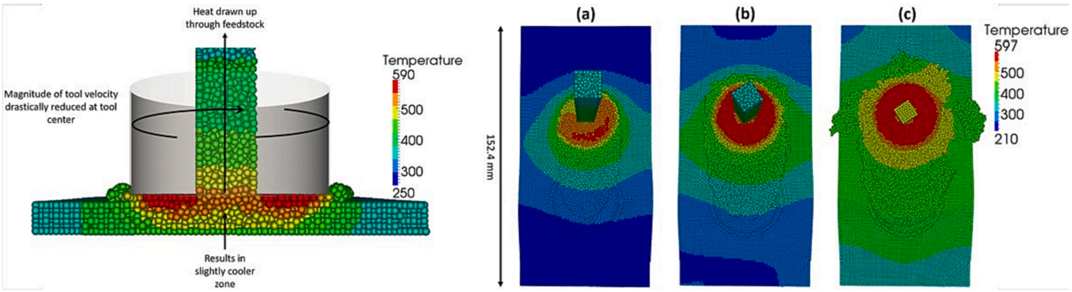

Fig. 13. Simulated temperature (°C) contour plots of AFSD of AA6061-T651: (a) starved at a feeding rate of 63.5 mm/min, (b) optimal at a feeding rate of 127 mm/min, and (c) overfed at a feeding rate of 254 mm/min [45].

causes of surface roughness in the as-built parts. The onion ring pattern, which resembles fish scale in welding (Fig. 22(c)) and chevron in LPBF (Fig. 22(b)), is the unique surface feature in AFSD, as shown in Fig. 22 (a). According to [52], the onion ring pattern results from the interaction between the tool trailing edge and the top surface of the deposited layer with each tool revolution, as illustrated in Fig. 23. Thus, the spacing of the onion ring pattern corresponds well with the calculated advance per revolution V/Ω.

Another macroscopic surface defect is galling. As shown in Fig. 24, galling can be inferred from uneven spacing or even breakdown of the onion ring pattern, which could be caused by adhesion between the feedstock rod and the deposited material. When processing a new alloy with AFSD, a thorough optimization is needed to identify the suitable processing window for fabricating parts without macroscopic defects.

It is worth noting that the protruding tool head has significant impact on surface morphology. When comparing Fig. 25(1–3) to Fig. 25(4–6), it appears that the flat tool produces a higher surface quality deposited layer than a protruding tool, hypothesized to be due to insufficient heating and deformation of the feedstock material as a result of the thicker deposited layer. As a result, more material is involved and less heat is generated per material volume in the case of a protruding tool [51]. However, with proper optimization, both flat surface tools and tools with protrusions are capable of producing parts with no macroscopic defects. As shown in Fig. 26, other surface defects, such as surface scratching and edge cracking, occur as a result of improper layer sticking or an incorrect match between axial pressure and rotation speed while manufacturing tubular samples [25].

2.4.2. Poor material bonding and local melting

Another type of defect in AFSD is related to the thermal input and characteristics. As illustrated in Fig. 27, poor material bonding (weak bonding or even delamination between deposited material and the substrate) occurs as a result of reduced material mixing and flow caused by insufficient thermal input. Another defect is local melting. The peak tempera ture of the AFSD process typically ranges between 60 % ~ 90 % of the melting temperature. However, as stated in [57], adiabatic heating caused by a low shoulder transverse speed or high shoulder rotation frequency causes the local temperature to exceed the melting temperature, resulting in local melting. And the local melting and the subsequent solidification may result in the occurrence of porosity and cracks in the deposited components.

2.4.3. Other defects

The AFSD operates in an ambient environment. Without the constraint of a vacuum or oxygen-free chamber, the deposition size has no limit but with a disadvantage - the oxidation of alloys, particularly for

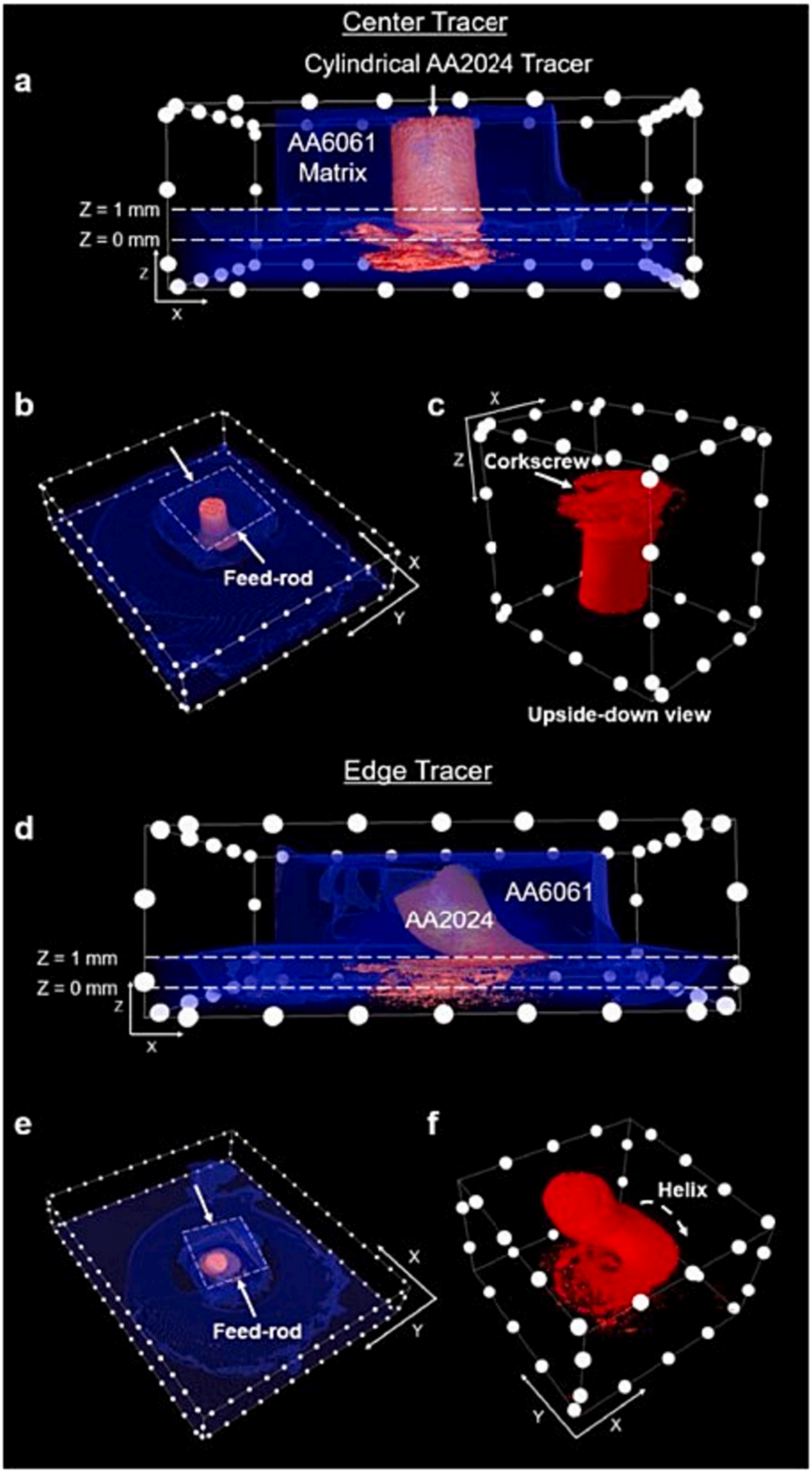

Fig. 14. X-ray computed tomography results after initial material feeding for the ((a)-(c)) center tracer and ((d)-(f)) edge tracer. The AA2024 tracer is shown in red, while the surrounding AA6061 matrix is either blue or transparent. Each pair of white dots is 2.5 mm apart [38].

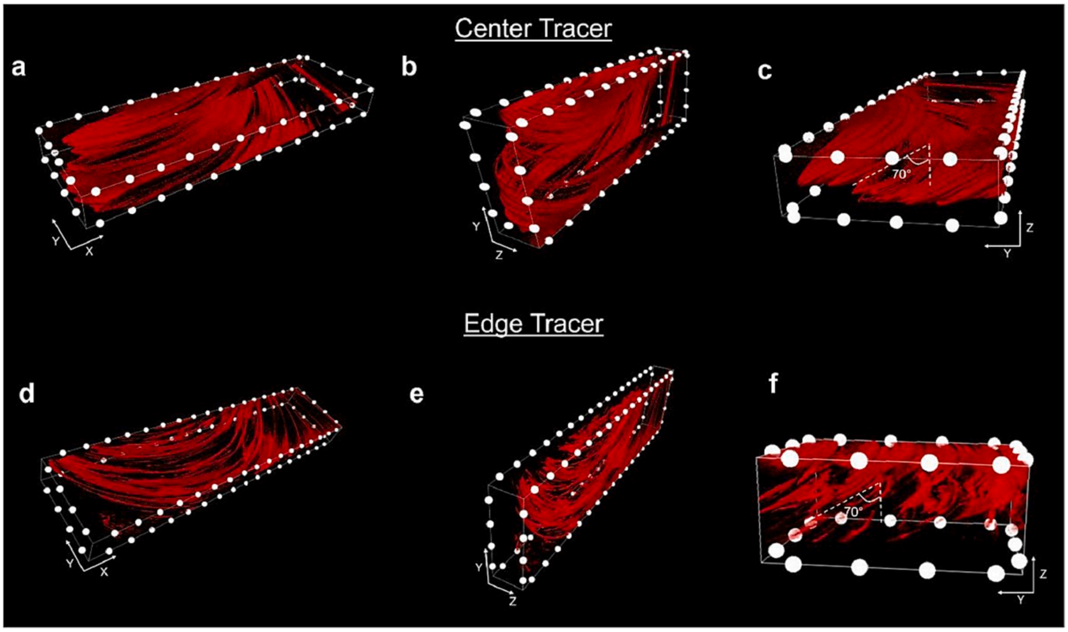

Fig. 15. High resolution X-ray computed tomography results for ((a)-(c)) center tracer and ((d)-(f)) edge tracer after steady-state deposition of AA2024. Each pair of dots is 1.25 mm apart [38].

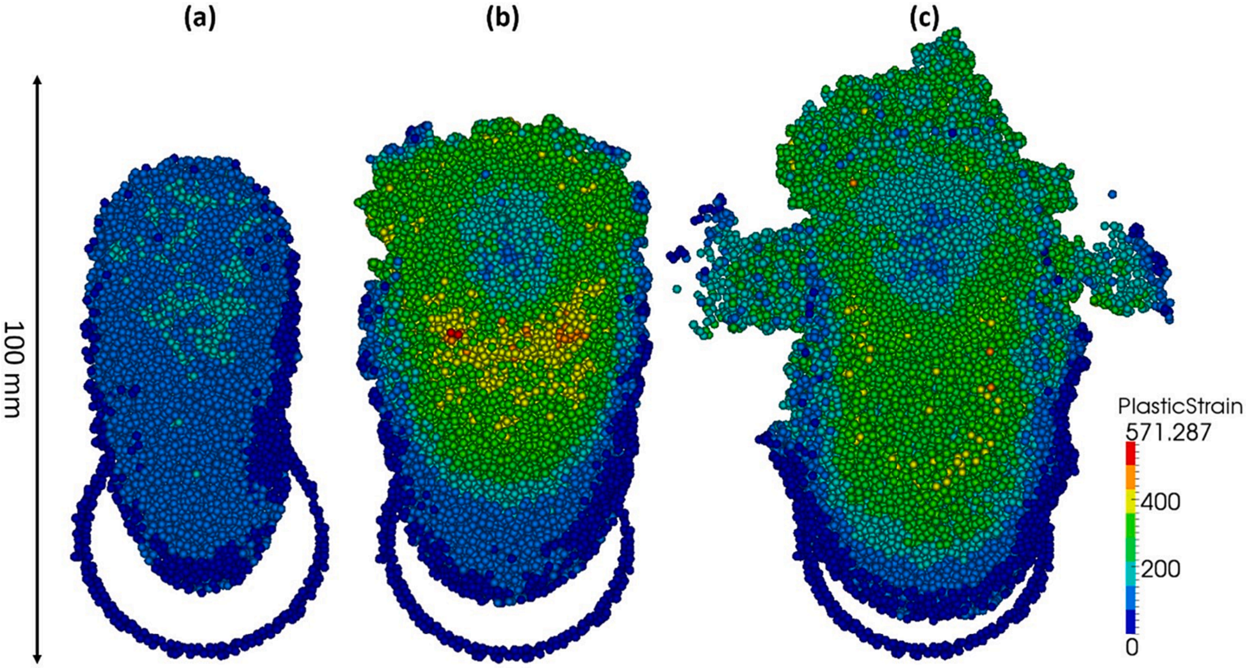

Fig. 16. Effective plastic strain contours of AFSD of AA6061 for (a) starved at a feeding rate of 63.5 mm/min, (b) optimal at a feeding rate of 127 mm/min, and (c) overfed at a feeding rate of 254 mm/min [45].

titanium or aluminum alloys, in the form of oxides or oxide layers. Aluminum oxide particles (Al_2O_3) were the first reported source of contamination in AFSD aluminum alloys, according to [59]. As shown in Fig. 28, Al_2O_3 particles and trace film are observed in cracks, indicating that alloy oxidation can be a potential initial site of cracks in AFSD processing. The oxide layer, on the other hand, can interfere with the subsequent layer bonding. As a result, the oxidation behaviors in AFSD can degrade the properties of manufactured parts and must be avoided. In some studies [26], the top surface of the layer was machined flat and even to the extent necessary to remove the oxide layer on the deposited layers. Furthermore, although it is highly possible for AFSD to fabricate components without pores, small pores below 3 μm have been observed in the AFSD of Alloy 110 Cu [34] and AA1060 [60].

Overall, the defects listed above are caused by process variables, and the construction of processing windows to produce fully-dense and defect-free parts has long been a source of concern for researchers. Fig. 29 shows a schematically constructed feasible processing window. For example, outside the window, intense heating can cause tool head damage, feed material jamming inside the hollow channel, or local melting at very high rotation rates (Ω). Inadequate heat generation at low Ω or high feeding rates (*F*), a lack of material flow, and plastic deformation can result in flash or galling. Insufficient feedstock material

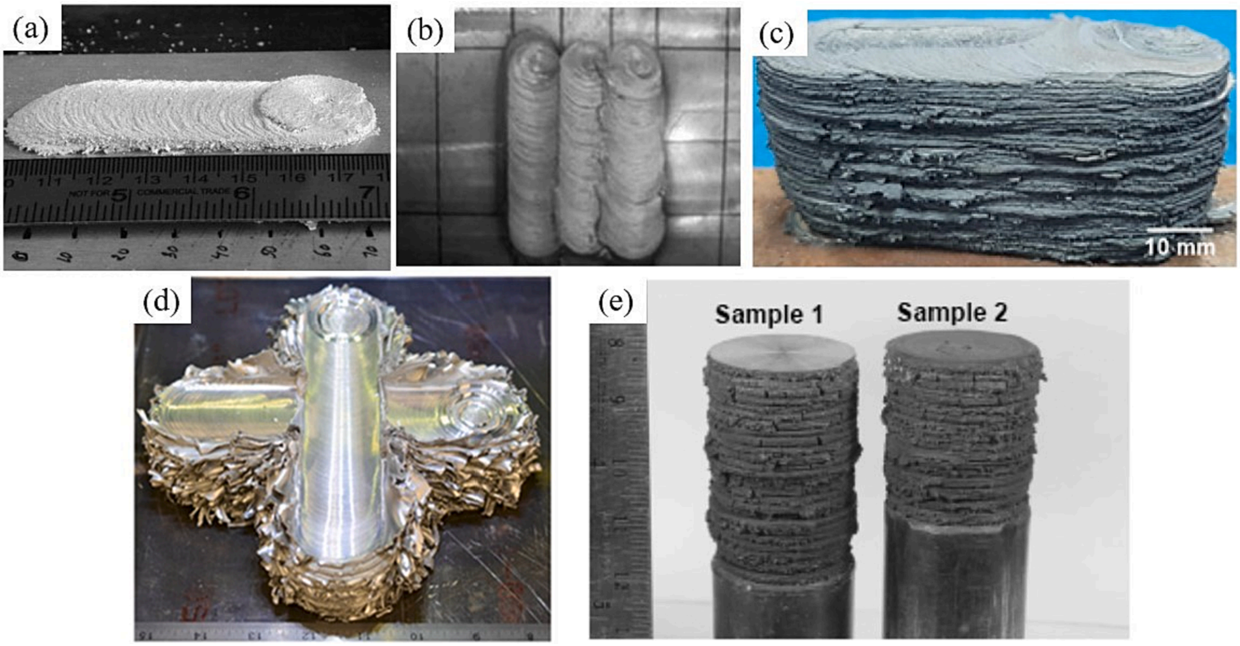

Fig. 17. AFSDed samples: (a) single layer and single-pass AA2014 deposit [26], (b) single-layer and multi-pass mild steel deposit [35], (c) multiple-layer and single-pass SS304 deposit [20], (d) cross structure aluminum deposit [50], (e) cylindrical AISI304 deposit [21].

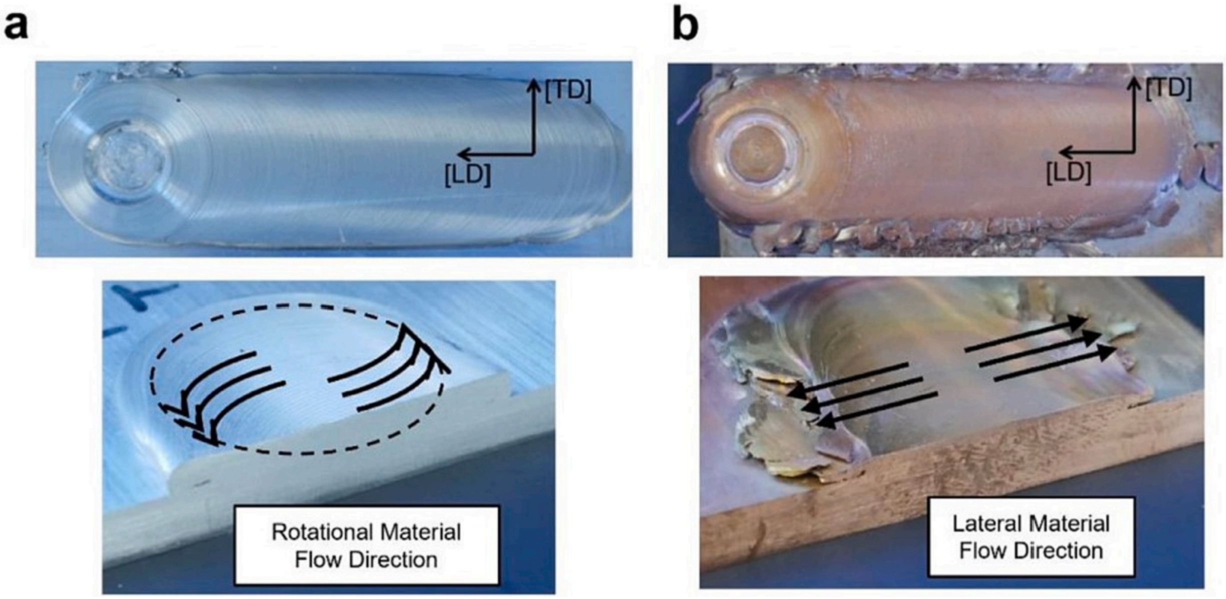

Fig. 18. Material flow during AFSD of (a) Al-Mg-Si and (b) Cu [29].

is supplied for deposition at low *F* and high *V*, resulting in pore formation or poor surface quality.

3. Structure

Although there is no melting or solidification in AFSD techniques, the material is severely deformed due to the frictional heating and rotating effect, providing driving forces for microscopic and macroscopic evolution. Structure evolution in AFSD under severe plastic deformation is quite different from fusion-based AM techniques, and more akin to forging processes. This section focuses on structure evolution in order to elucidate the Process-Structure-Property relationship in AFSD. Furthermore, a thorough understanding of structure evolution is critical in understanding the development of defects, microstructure, macrostructure, and properties. Possible evolution mechanisms that control the deformed structure, such as grain structure and size, precipitates, and texture, are discussed in detail in the following sections.

3.1. *Microstructure subjected to severe plastic deformation*

In AFSD, the feeding material is rotated at a speed of ~100 rpm. Heat is generated by dynamic contact friction at the tool/rod-substrate/deposited material interface and plastic deformation. In AFSD, softened materials undergo large plastic deformation at a high strain-rate and elevated temperatures, resulting in a deformed structure. The residual energy provides the thermodynamic and kinetic conditions for

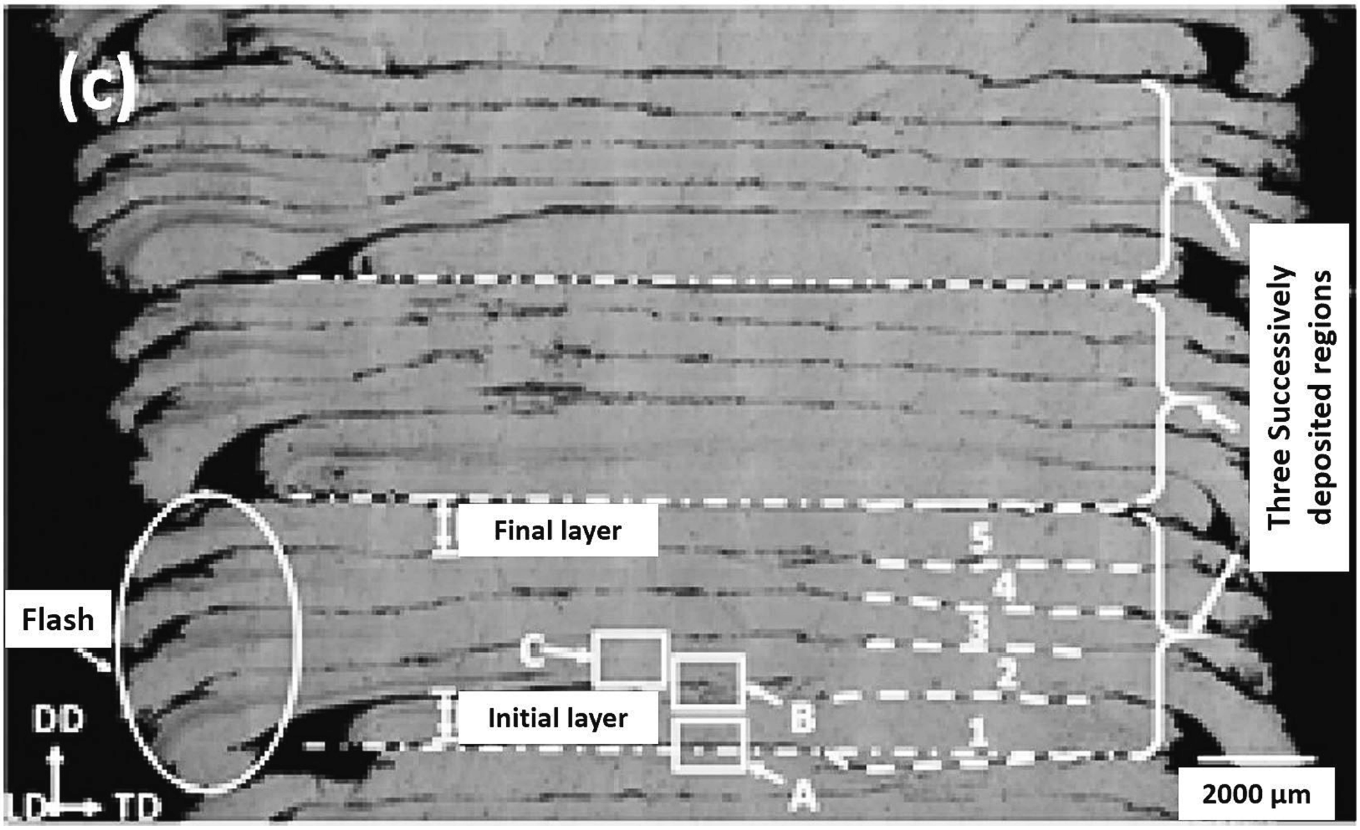

Fig. 19. Flash phenomena along building direction of deposited SS304 [20].

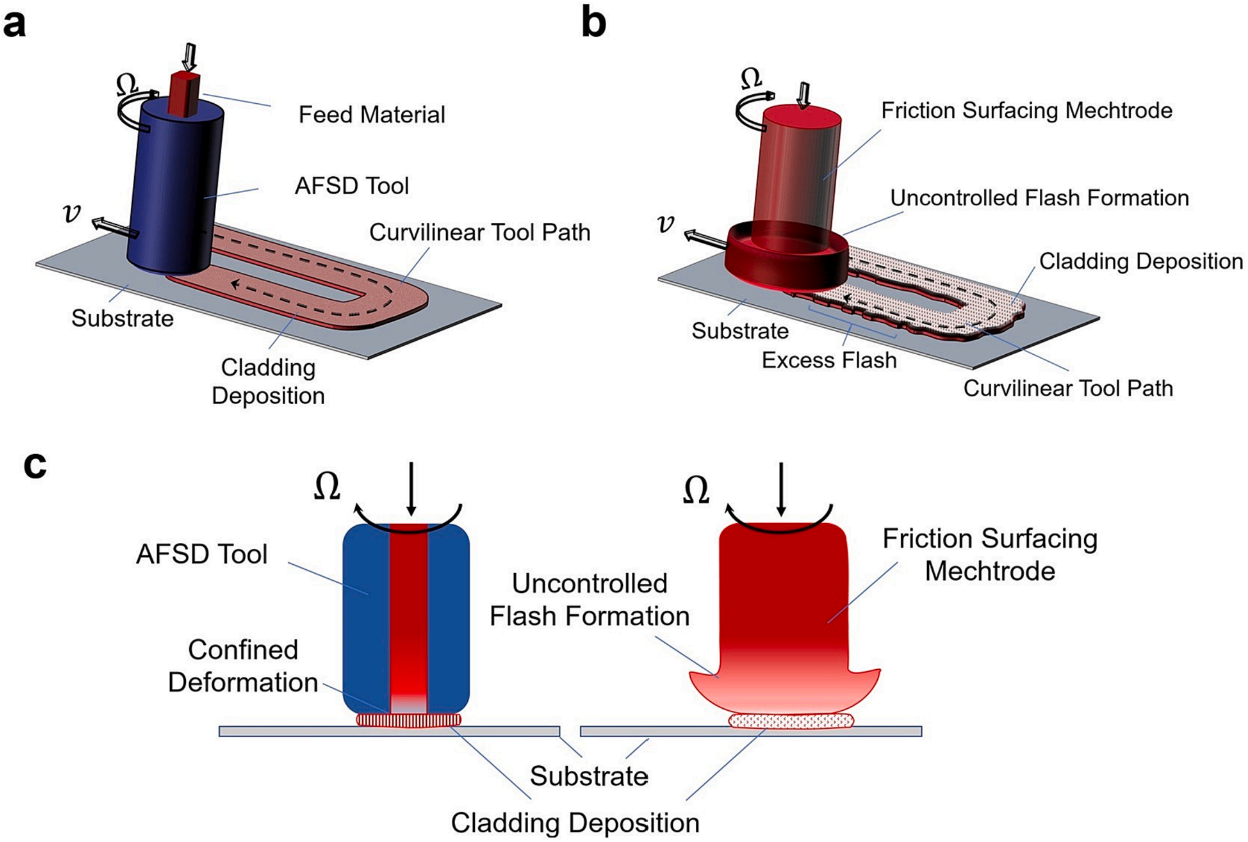

Fig. 20. Flash phenomena under different AFSD processes: (a) with a hollow tool, (b) without hollow tool, and (c) 2D views [51].

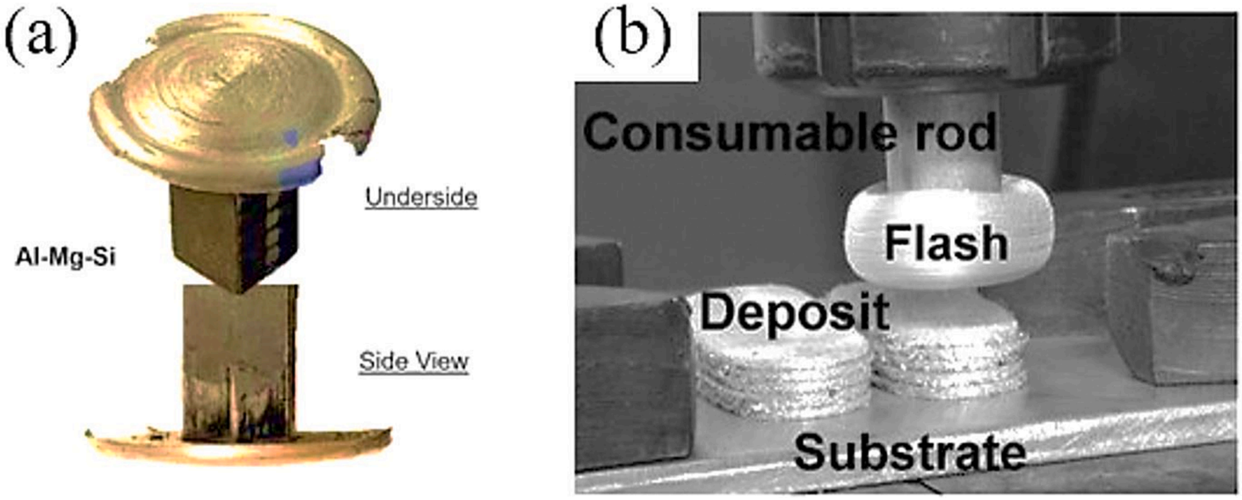

Fig. 21. The residual consumable rod in AFSD (a) with a hollow tool (Al-Mg-Si alloy) [29] and (b) without a hollow tool (AA2014 alloy) [26].

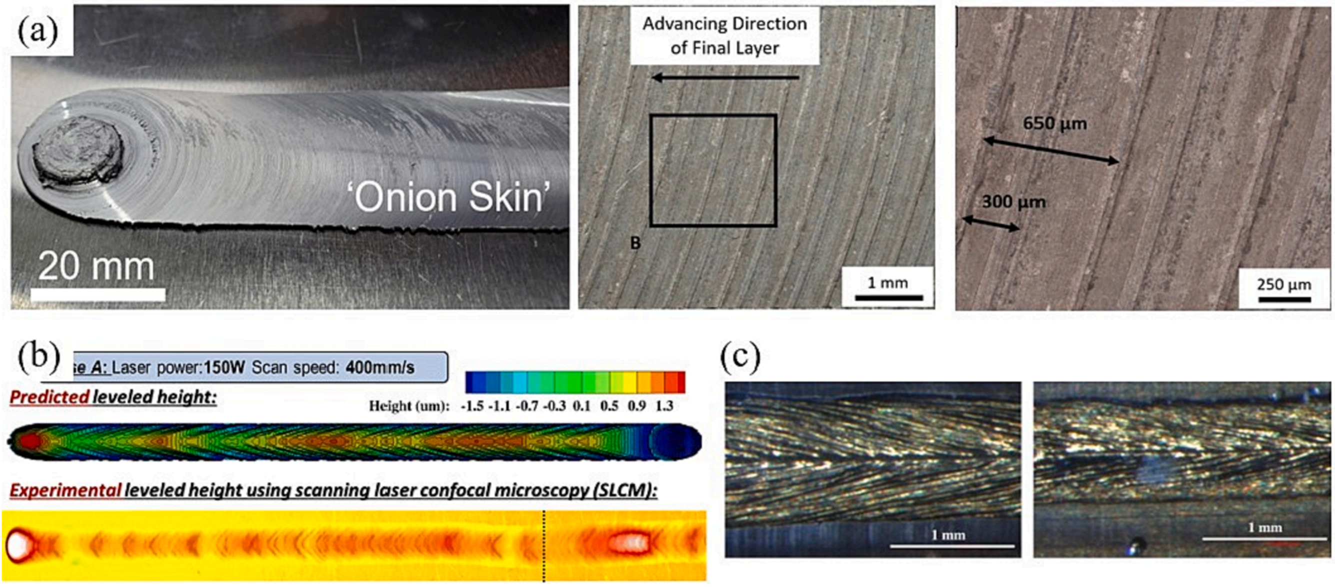

Fig. 22. (a) Macroscopic images of the onion skin in AFSD [51,53]. (b) Experimental and numerical surface morphology in LPBF [54,55]. (c) Typical surface morphology in laser welding [56].

recovery and recrystallization following deformation. The dislocation density of the material greatly increases during the plastic deformation in the AFSD process. During dynamic recovery and dynamic recrystallization, dislocations within a grain rearrange to form cells, sub-grains, and so on. First, the dislocations tangle, merge, and annihilate, forming cells. As more dislocations are generated as a result of continuous deformation, they are absorbed by sub-grain boundaries, transforming into low-angle grain boundaries and then into high-angle grain boundaries. Thus, the deformed grains are pinched-off, and the grains are refined in AFSD in this manner.

The generation of dislocations and their subsequent accumulation at grain boundaries, sub-grains, and particles nucleating defect-free crystallites govern recrystallization behavior [61]. Recrystallization can be classified into two types: static recrystallization (SRX) and dynamic recrystallization (DRX). SRX frequently occurs during annealing and DRX occurs during hot deformation, both of which occur in the AFSD process. During deformation, there are three types of DRX: continuous dynamic recrystallization (CDRX), discontinuous dynamic recrystallization (DDRX), and geometrical dynamic recrystallization (GDRX). DDRX is distinguished by the nucleation and growth of dislocation-free grains, whereas CDRX is distinguished by the progressive accumulation, annihilation, and reorganization of dislocations in the absence of discrete nucleation and growth events [62,63].

The grains are elongated along with the deformation direction during the initial stage of AFSD, as shown schematically in (Fig. 30(1)). Substructures form inside the grains as shear strain increases due to dynamic recovery. The dislocation density increases with material deformation during deposition. The dislocation tangles, annihilates, rearranges into sub-grains, and cell formation occurs at this stage. Only low-angle grain boundaries (LAGBs) are involved at this stage (Fig. 30(2)). Dynamic recrystallization and high-angle grain boundary (HAGB) movement occur as strain is increased continuously. When the strain reaches a critical value, the HAGB spacing approaches the sub-grain size and the adjacent grain boundaries pinch off, forming a roughly equiaxed microstructure (Fig. 30(3)) [38,62,64].

With further deformation, dynamic recovery and recrystallization continue, resulting in a reduction in grain size. However, as the strain increases, the most equilibrium state is not reached, even though

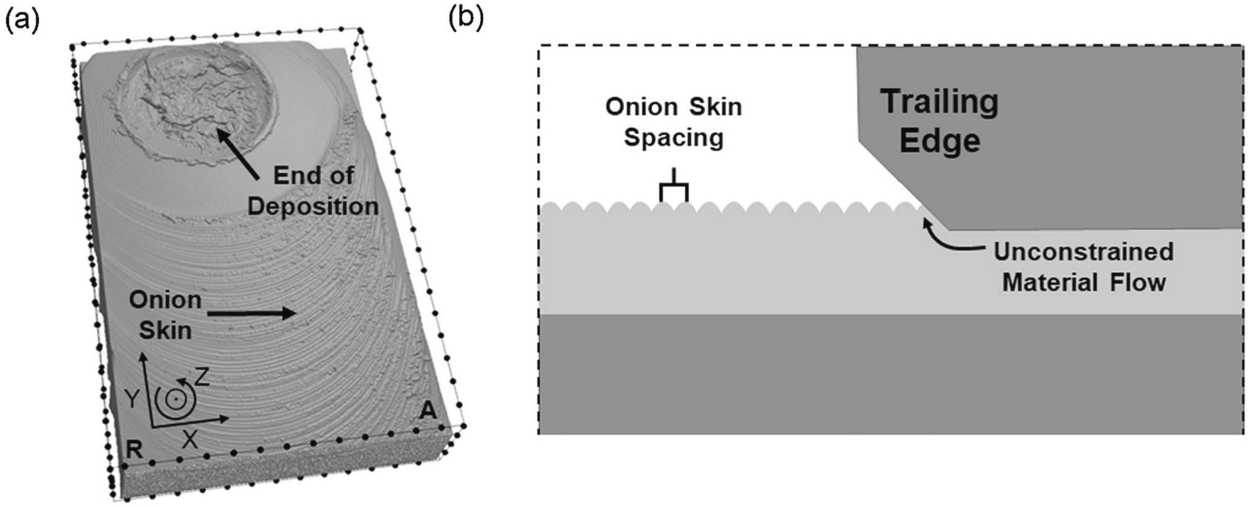

Fig. 23. (a) A top-down view of the deposit based on X-ray computed tomography of AFSD of AA2024. (b) Illustration of the onion skin formation [52].

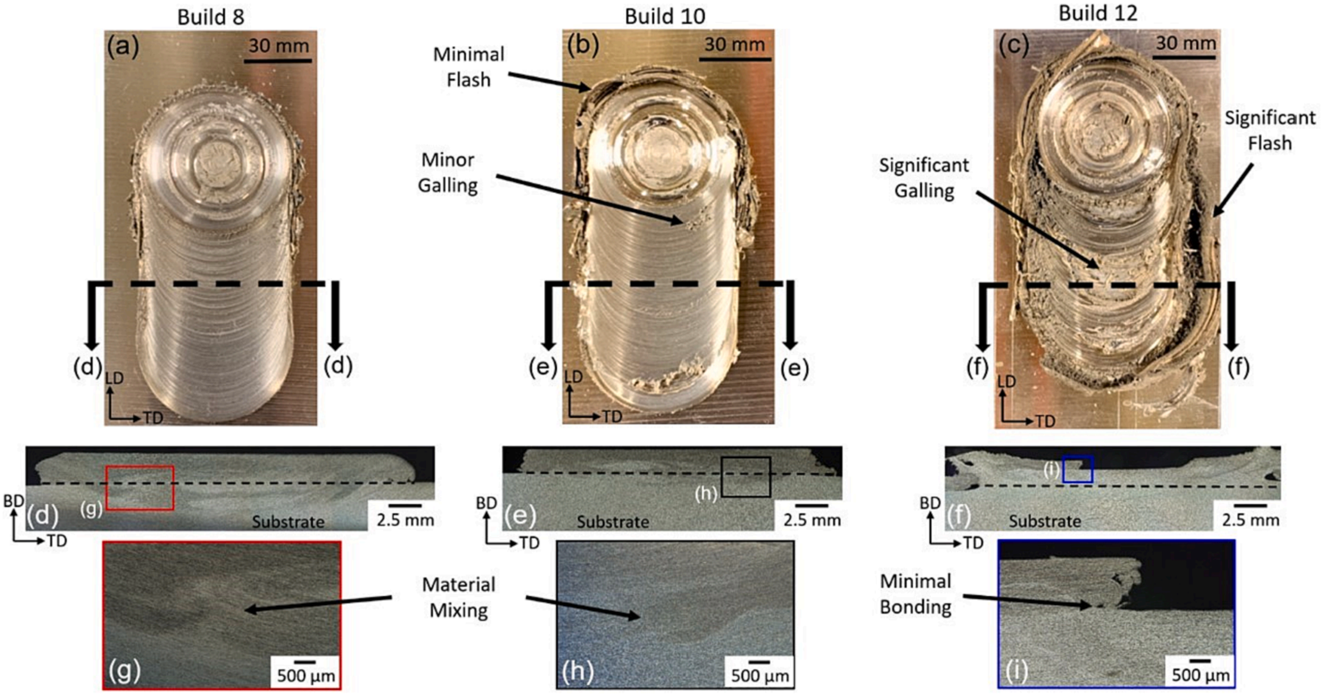

Fig. 24. Morphologies of the WE43 AFSD material deposits with (a) no macro defects and well consolidated build, (b) minor galling and flash, and (c) significant galling and macro defects [32].

recrystallization is complete. At high temperatures, the grains continue to grow in order to minimize total interface energy, as shown in Fig. 30 (4). The stacking fault energy (SFE) of alloys is important in microstructure evolution during and after deformation because it explains how dislocations resolve, which has an impact on DRX behaviors. The SFE of Al-Mg-Si is high ($>160\ mJ/m^2$ [65]), whereas Cu has a low SFE ($\sim 78\ mJ/m^2$) [65,66]. Griffiths et al. [29] conducted comparative studies on the microstructure of Al-Mg-Si and Cu after deformation. The results show that grain size reduction is much greater in alloys with high SFE than in alloys with low SFE.

3.2. Grain morphology: Structure and size

In contrast to the columnar solidified structure of fusion-based AM, AFSD processes produce small and equiaxed grains. Due to recovery and recrystallization, the deformed microstructure evolves into fine, full-equiaxed grains after severe plastic deformation. The evolution of grain structure is closely related to strain. At this stage, there is a critical strain level for achieving fully equiaxed microstructure, and grain size decreases with increasing strain. By comparing the grain size of Fig. 31 (f) and (g), it can be concluded that the grain size following this stage increases. In Fig. 31(e), the pinch-off of the deformed structure can be identified and transforms the deformed structure into a full-equiaxed microstructure [61,62,67].

This evolution of grain structure can also be seen at the tip of an used consumable rod. Refined and equiaxed grains are shown at the tip of the consumable rod in Fig. 32, indicating that recrystallization occurs before the deposited material is transferred to the substrate. Although AFSD allows for the production of components with a fully equiaxed microstructure, the fraction of equiaxed grains is highly dependent on process

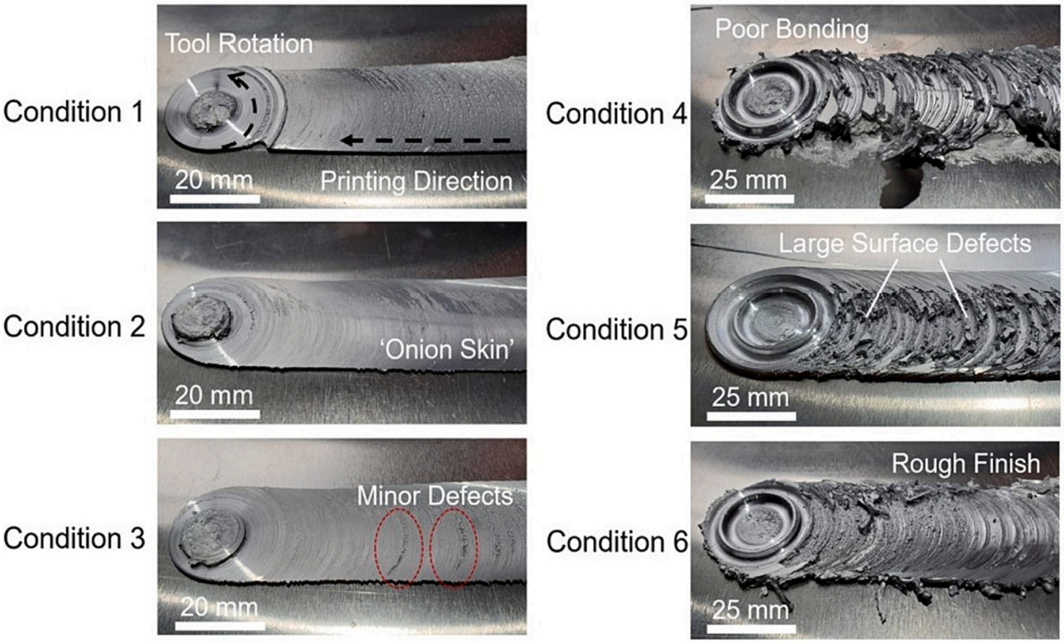

Fig. 25. Surface quality of AFSD Al-Mg-Si deposits using different tools: the surface morphologies of the deposits that are produced when the flat tool is used under conditions 1–3 and when the protruding tool is used under conditions 4–6 [51].

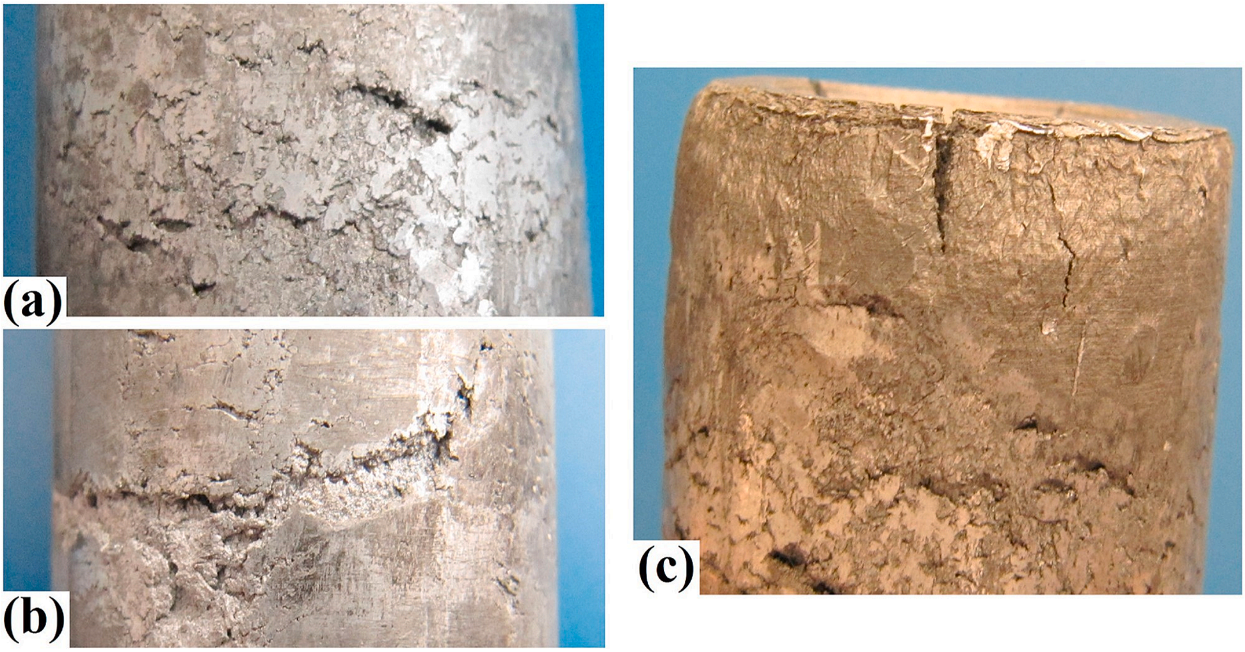

Fig. 26. The side views of the manufactured AA2024-Al_2O_3 tube showing different defects: (a) surface scratches, (b) metal deposition lock between layers, and (c) edge cracking at the top of the tube [25].

variables. When subjected to process variables that ensure more complete recrystallization, more equiaxed grains form [29,68].

As previously stated, when the proper processing variables are used, full and equiaxed grains can be obtained in AFSD. The typical Electron backscattered diffraction (EBSD) maps of as-received feedstock and AFSDed samples are shown in Fig. 33. The wrought AA7075 feedstock has a typical rolled microstructure of large "pancake-like" grains on the transverse and longitudinal planes with a size of 100 μm, as shown in Fig. 33(a). The as deposited EBSD maps (Fig. 33(b-d)) show the refined equiaxed microstructure throughout the build with a height of 65 mm. In this study, the average grain size decreases slightly from 5.05 μm of initial layers to 4.33 μm of final layers [69]. This slight decrease is thought to be strongly related to the reduced number of thermal cycles performed at the final layers compared to the initial layers.

A similar reduction in grain size due to reduced thermal cycles is shown in [50]. Titanium alloys, on the other hand, exhibit completely different trends in terms of grain size variation along the building direction. The β grain size at the top layer (26 ± 0.5 μm) is larger than the grain size at the bottom layer (17 ± 1.0 μm) due to the faster cooling rate at the bottom layer, as shown in Fig. 34. This spatial difference in grain size between aluminum and titanium alloys is due to the fact that Al alloys respond totally different to thermal input from Ti64 since

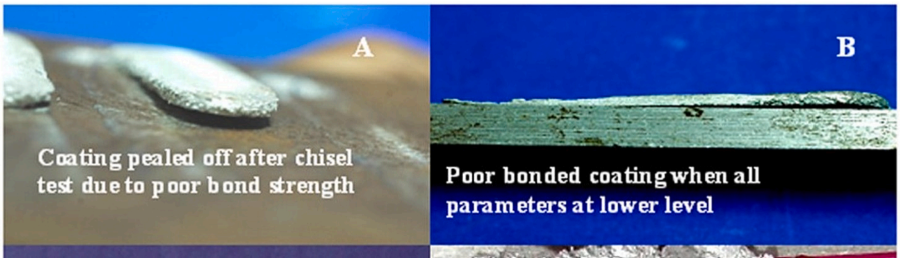

Fig. 27. (a) Delamination between deposit (AA6063) and substrate (mild steel) and (b) poor bonded deposit [58].

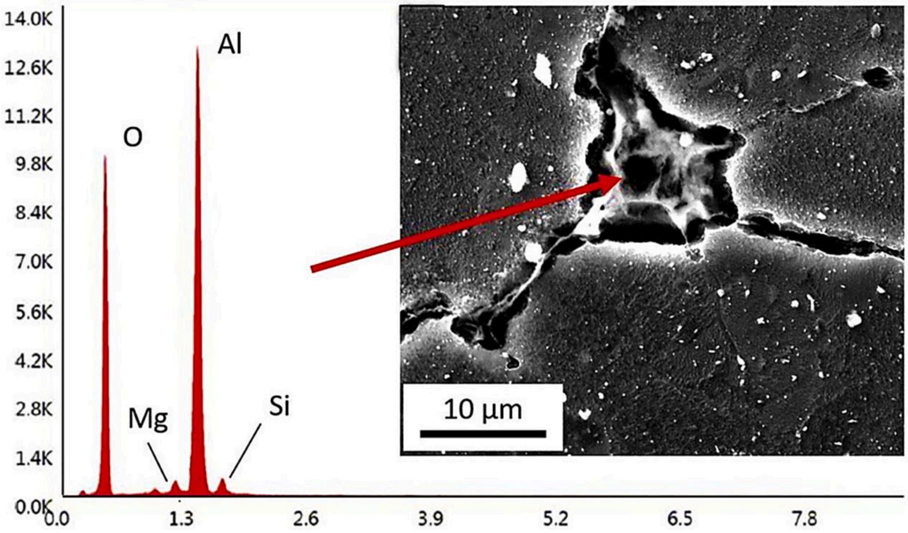

Fig. 28. EDS analysis and SEM image of trapped oxides in a crack [59].

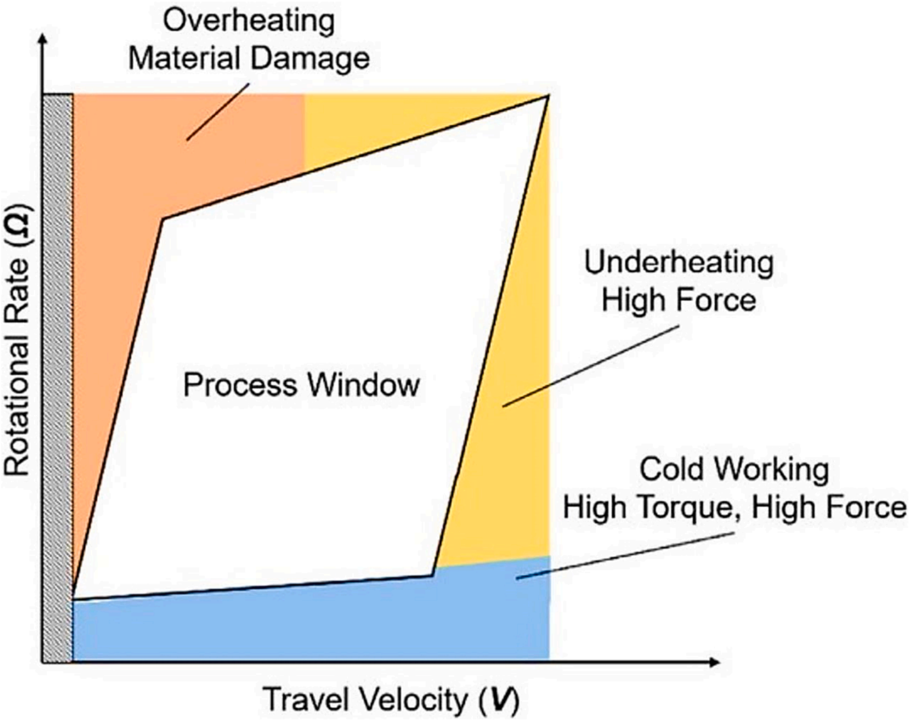

Fig. 29. A possible processing window determined by rotation rate (Ω) and travel velocity (*V)* [29].

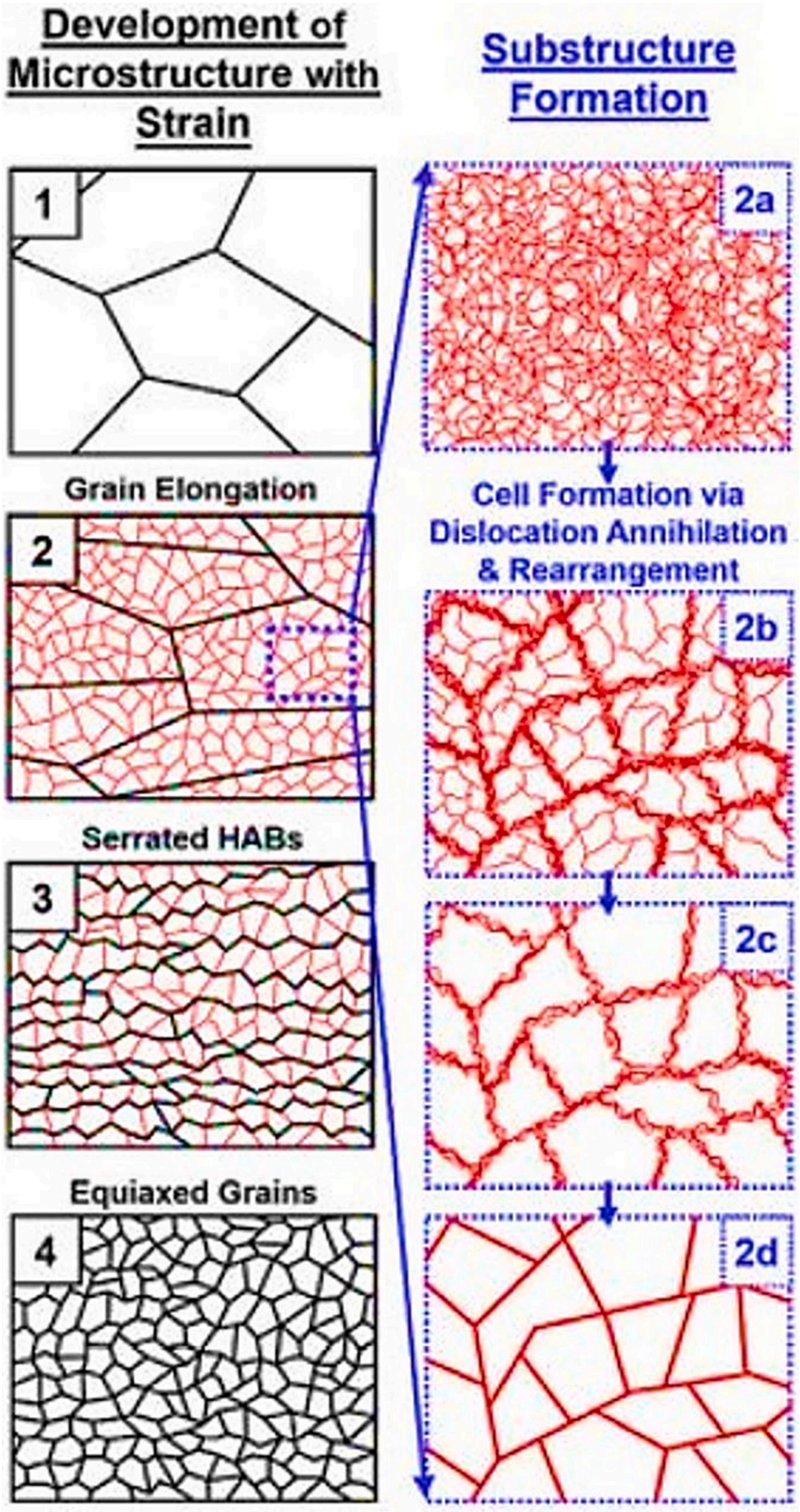

Fig. 30. Schematic diagrams showing the evolution of grain structure during deposition/deformation process [38].

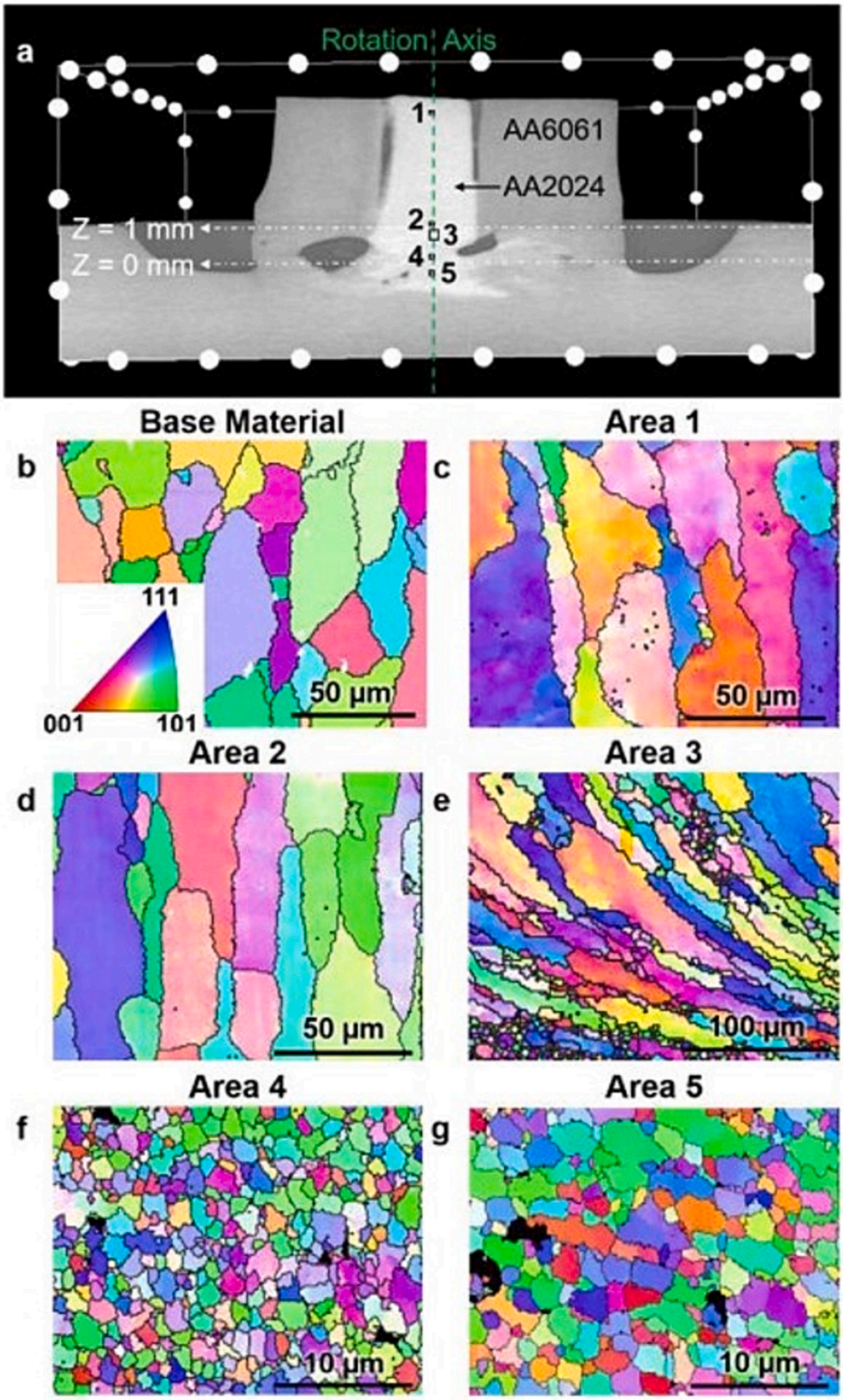

Fig. 31. Grain structure at different strain levels. (a) A cross-section of a feedstock rod with areas of interest labeled. Each white dot is 2.5 mm apart. Inverse pole figures (IPFs) of the AA2024 tracer for (b) before AFSD, (c) area 1 (Z = 4.2 mm), (d) area 2 (Z = 1.1 mm), (e) area 3 (Z = 0.9 mm), (f) area 4 (Z = 0.26 mm), and (g) area 5 (Z = -0.2 mm) [38].

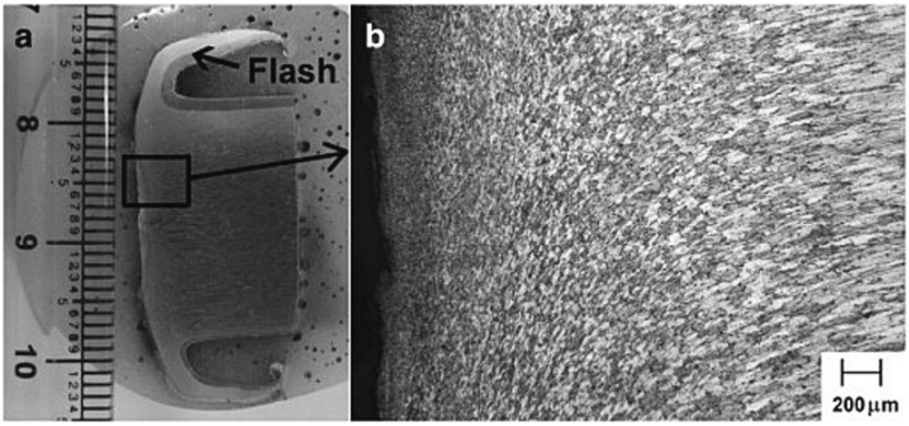

Fig. 32. (a) A residual AA2014 rod after deposition. (b) The microstructure features at the tip of the rod. The fine, recrystallized grains show near the tip [26].

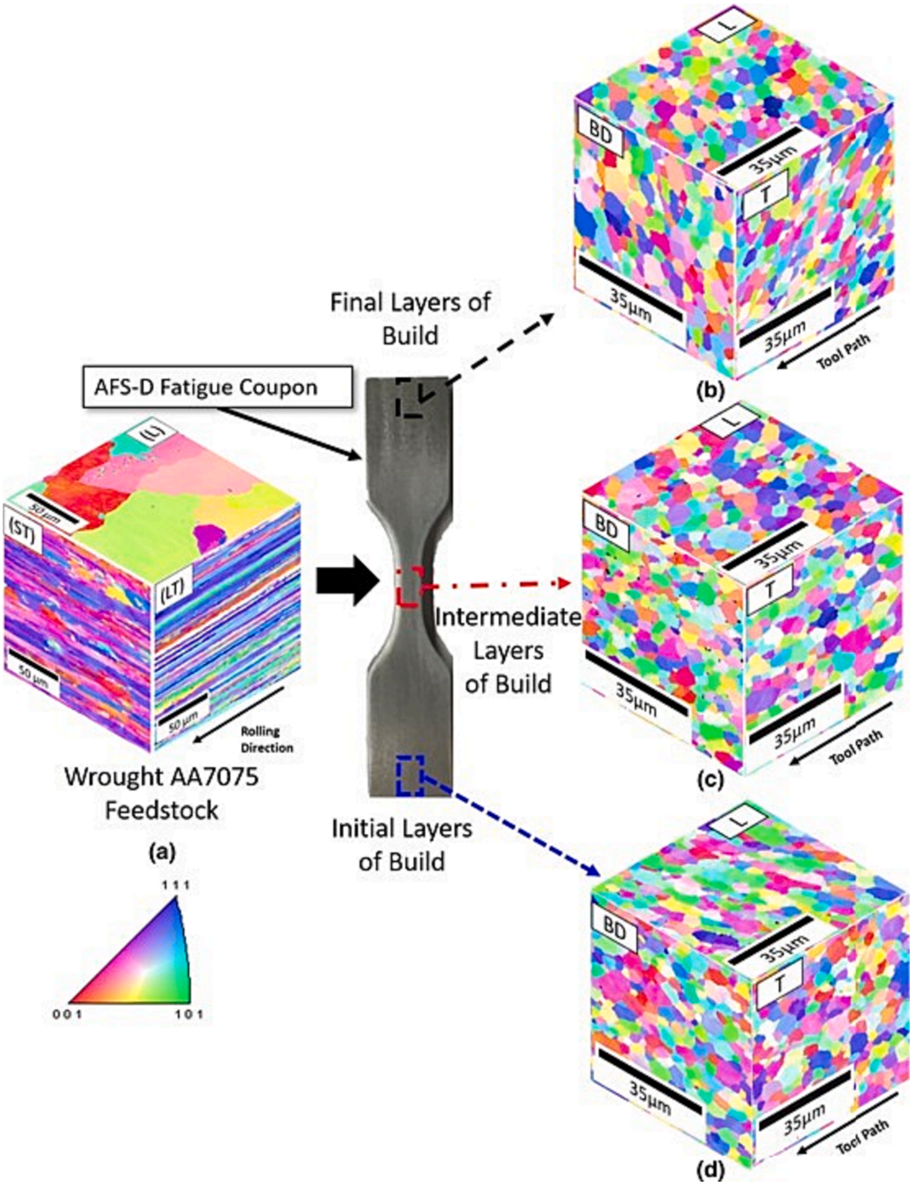

Fig. 33. Three-dimensional IPFs showing the microstructure of the (A) AA7075 material and (B-D) as deposited AA7075 material at different layers [69].

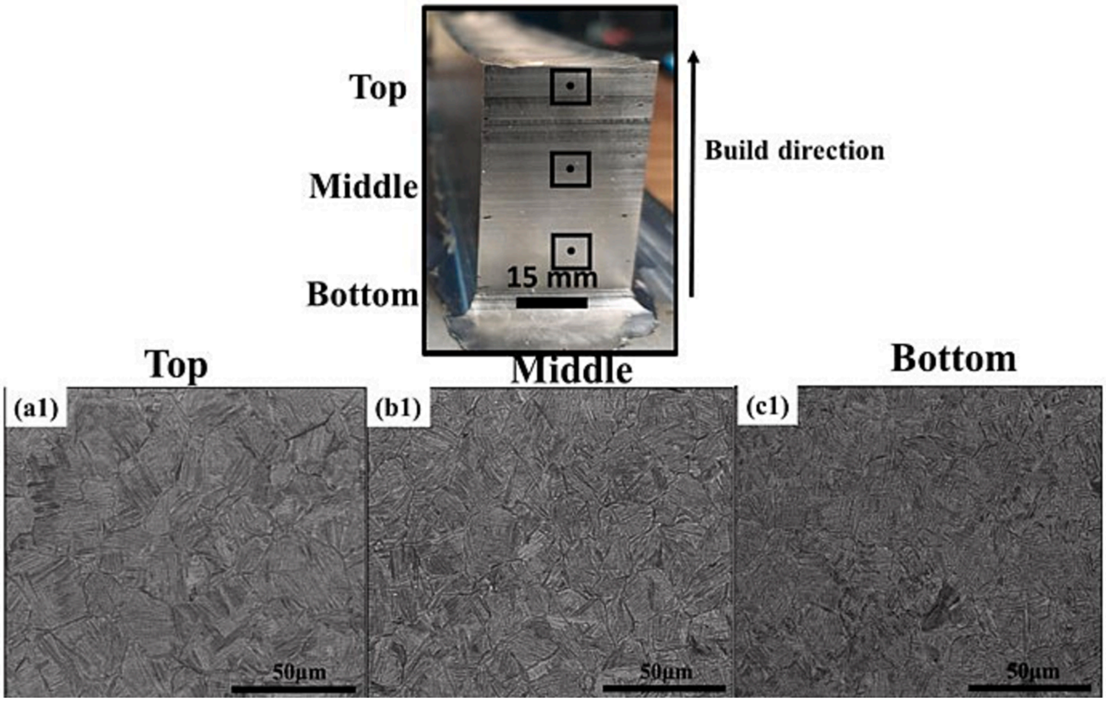

Fig. 34. Ti-6Al-4 V alloy part built by the AFSD technique: (a1)–(c1) low magnification back-scattered electron (BSE) images [27].

Aluminum alloys have very high thermal conductivity and are age-hardenable [27]. The lower thermal conductivity ensures sufficient heat for Ti64 without causing local overheating. Despite these clear grain size trends along building direction, the as-deposited Inconel 625 samples exhibit grain size fluctuation, as shown in Fig. 35 [70].

In addition to the variation along the building direction, the grain size difference along the transverse direction for aluminum alloys is investigated in [71]. The grain size is larger at the periphery than at the center of the deposit, as shown in Fig. 36, because the grains at the periphery are deformed along the mass flow direction. Notably, the deformed structure at the periphery occurs concurrently with the flash defects, implying that defect control and structure evolution are strongly related to material flow and deformation behaviors. The observation of grain of the deformed feedstock demonstrates both material flow and grain size along the radial direction. The grain size decreases from the periphery to the consumable tip, as shown in Fig. 37. Interestingly, the grain size near the center of this consumable rod (Fig. 37(b)) is smaller than the average size (8.5 ± 3.1 μm) of deposited samples, indicating grain growth in the as-deposited samples after deposition [71].

In general, the as-deposited microstructure reduces average grain size by 90 % ~ 97 % for aluminum alloys part created using AFSD [69,72]. This grain refinement is caused by DRX due to the severe plastic deformation and high strain rate of the AFSD process in alloys with high SFE, such as aluminum alloys [73]. The AFSD of Inconel 625, Titanium alloys, and magnesium alloys also show similar grain refinement results. The grain size of as-received and as-deposited samples for these metallic alloys is summarized in Table 1. These three alloys appear to have a significant reduction in grain size. The as-deposited Cu samples, on the other hand, show only minor grain refinement or even grain coarsening. This is due to the fact that dynamic recovery, GDRX, and CDRX control the continuous types of microstructure evolution in alloys with high SPE, such as aluminum alloys, whereas competition between dynamic recovery and DDRX controls the discontinuous type of microstructure evolution in alloys with moderate SPE, such as copper alloys [29]. Furthermore, it is possible that the pre-deformed state of Cu, rather than the annealed state, shifts the balance between recrystallization and recovery [34].

Aside from grain size, the grain boundary distribution in the as-received and as-deposited samples is similar. Traditionally, boundary misorientations between 2° and 15° are classified as LAGB, while misorientations above 15° are classified as HAGB. The misorientation angle distributions of the AA 2024 feedstock material and as-deposited material are shown in Fig. 38. More grains with LAGBs are found in the deposit [52]. Critically, the kinetics of microstructure evolution in AFSD processes are affected by process variables such as rotation rate Ω, in-plane scanning velocity V, and material feeding rate F. The thermal history and deformation behaviors are controlled by these variables. Thus, in addition to governing the processing window, these variables heavily influence microstructure evolution.

3.3. Precipitates and intermetallic particles

Precipitate strengthening is a crucial mechanism for alloys, particularly for precipitation hardening alloys like aluminum alloys. Most precipitates in the feedstock material are likely to solutionize and dissolve into the matrix during the AFSD process due to severe plastic deformation at elevated temperatures [74]. Re-precipitation begins during cooling, but the resulting precipitate size and number density are far from the peak strengthening condition [51]. Fig. 39(a)-(f) shows transmission electron microscope (TEM) graphs of the feedstock AA2014 rod and as-deposited samples. Plate-shaped strengthening precipitates γ' ($Al_5Cu_2Mg_8Si_5$) and θ' (Al_2Cu) are found in the feedstock rod sample (Fig. 39(c)), and over-aged precipitates corresponding to γ and θ phases are found in the as-deposited samples (Fig. 39(d)), causing microhardness degradation [26]. The absence of θ' precipitates in as-deposited samples is also observed during AFSD of AA2219 [72].

Different heat treatments are applied to the deposits in order to increase their hardness, and TEM graphs of the deposits after heat treatment are shown in Fig. 39(g)-(i). There is little difference in the deposit after direct aging (Fig. 39(g)). After solution treatment and aging, the deposit exhibits proper strengthening precipitation (Fig. 39(h)). However, high temperature solution treatment causes grain coarsening, as shown in Fig. 39(i). The needle shapes β'' precipitates in as-received rod [75] dissolve and re-precipitate into Mg-Si solute clusters [68]. The

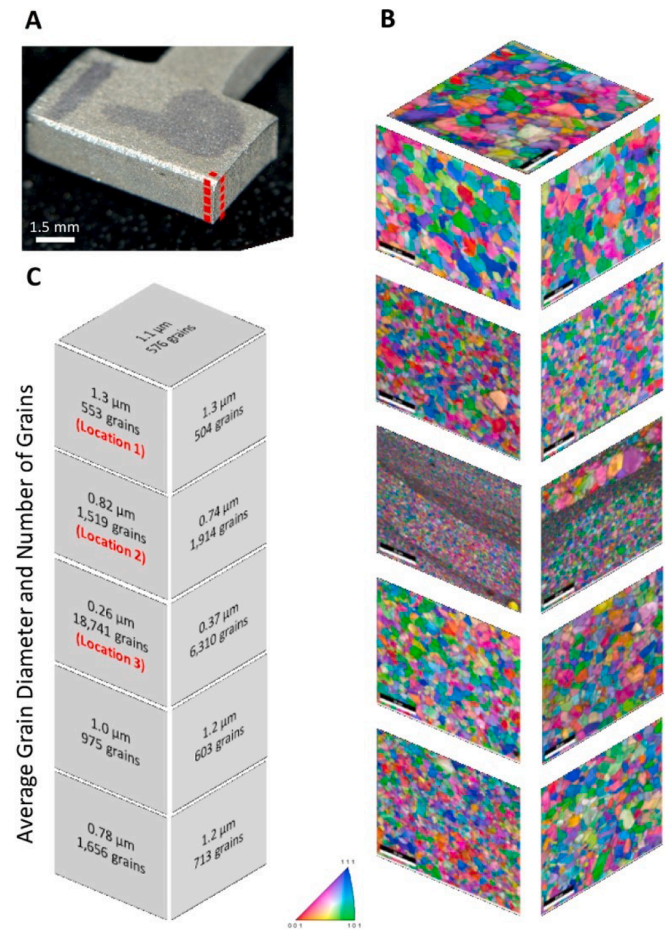

Note: All scale bars are 10 micron

Fig. 35. Inconel 625 alloy part built by the AFSD technique. (A) Deposited part with a red color dashed line indicating the Euler EBSD mapping region of interest. (B) Euler EBSD mapping of five locations along the building direction. Each image has the same magnification and is located along the same axis. (C) Average grain size and number (location matches the EBSD map in (B)) [70].

return of these dispersed and needle-like β’’ precipitates can be achieved through proper solution, rapid quenching, and an artificial aging heat treatment (SQA) [76]. These findings are supported by the XRD results for AA6061 (Fig. 40) [71]. Other precipitates such as η and η’ in needle-like structures can be found in the AA7050 deposit [50]. Precipitates evolve similarly in nickel superalloys. The plate-like δ precipitates and disk-shaped γ’’ strengthening precipitates in the Inconel 718 rods disappear in the deposit, as shown in Fig. 41(a-b), and the γ’’ precipitates appear again after direct aging (Fig. 41(e-f)) [33].

In the AFSD process, second-phase particles are also discovered to evolve. As shown in Fig. 39(b), feedstock samples of aluminum AA2014 alloys contain highly elongated grains with a large number of undissolved second-phase Al_2Cu (black arrows) and $Fe - Mn - Al$ (white arrows) particles (5 μm ∼ 10 μm in size). Finer and more uniformly distributed second-phase particles (<1 μm in size) are observed in the as-deposited samples, as shown in Fig. 39(f). The plate-like Si particles are found to be broken into finer particles during AFSD of die cast aluminum A356 alloy, as observed in (Fig. 42) [77], caused by the action of tool stirring [41,78]. Similarly, fine carbide particles with a uniform distribution can be found in the Inconel 718 deposit [33]. Due to the shear stirring effect during AFSD, fracture and dispersion of large particles have also been reported in magnesium alloys [28].

3.4. *Texture*

The preferential orientation of the grains in a polycrystalline material is referred to as crystallographic texture. The texture of as-received and as-deposited samples differs due to plastic deformation and concomitant recovery and recrystallization in AFSD. However, different alloys react to it in different ways.

Fig. 38 shows the texture of as-received and as-deposited AA2024 alloys for aluminum alloys. Both cases have a misorientation distribution that is similar to the Mackenzie distribution [79,80]. The texture density of both samples is low and increases slightly for the as-deposited samples. For as-deposited samples, the texture also varies along the building direction. The texture plots of the as-deposited AA2219 samples are shown in Fig. 43. The PF and orientation distribution figure (ODF) of the common texture components typically found in aluminum alloys are shown in Fig. 44. All samples have a combination of fiber A and C texture. Furthermore, the $\{\overline{1}11\ 11\} < \overline{11}0 >$ fiber component and a split of the $\{1\overline{11}\} < 110 >$ fiber component are visible, and the highest texture density is seen at the top of the samples (Fig. 43(a)).

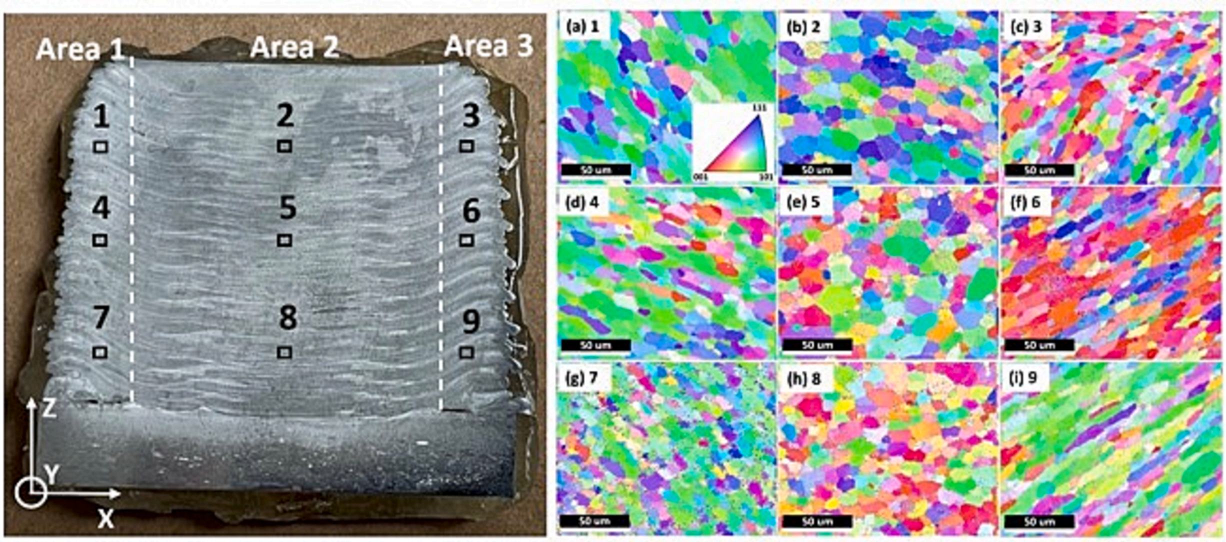

Fig. 36. EBSD IPFs of the as-deposited Al6061 alloy part at different locations. (a–i) Numbers 1–9 correspond to the nine locations depicted in the diagram [71].

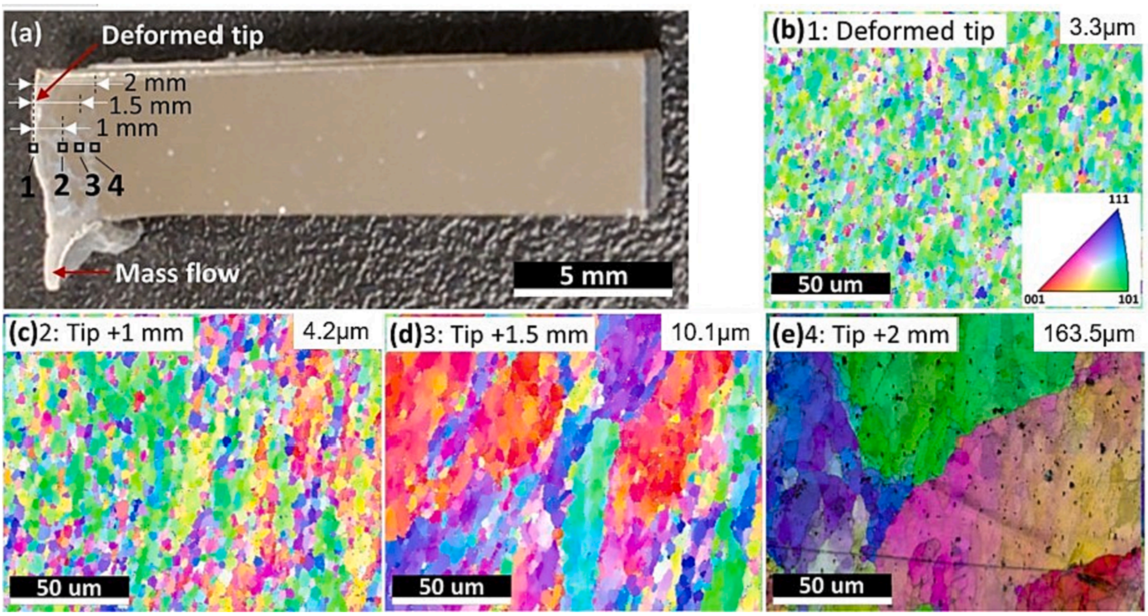

Fig. 37. Images of the residual Al6061 feedstock and its microstructure. (a) The quarter residual feedstock rod, with spots 1, 2, 3, and 4 representing the microstructural characterization regions. Spot 1 is on the deformed tip, while spots 2, 3, and 4 are 1 mm, 1.5 mm, and 2 mm vertically away from the tip, respectively. (b–e) EBSD IPFs at the spots 1–4 [71].

Table 1
The grain size of as-received and as-deposited samples of the reported metallic alloys.

Alloys	Grain size for feedstock/μm	Grain size for deposit/μm	Reference
AA6061	163.5 ± 96.2	8.5 ± 3.1	[71]
AA2024	57.2	4.9	[52]
Al-Mg-Si	113	13 ± 3	[29]
AA7075	15.2 ± 20.8	1.70 ± 0.89	[69]
AA5083	105.3	3.16	[51]
AA2219	30	2.5	[72]
WE43	45 ± 5	2.7 ± 2	[32]
Inconel 625	30	0.5	[70]
Inconel 718	50	5	[26]
Ti-6Al-4 V	not reported	26 ~ 64	[27]

Strong texture in as-deposited samples may result in anisotropic properties, and heat treatment such as annealing frequently reduces this anisotropy. The texture is also strongly related to process variables in AFSD. When low rotation rate and transverse speed are used, due to low shear strain, a weak C-type shear texture and a strong $B/\overline{B}$ texture are observed [29,67]. Aside from deformation behaviors, thermal input can cause differences in texture density and texture components throughout the deposited structures [50].

Another alloy that shows promise for AFSD techniques is magnesium alloy. Fig. 45 depicts typical texture plots of the WE43-T5 (a) feedstock and (b) top, (c) middle, and (d) bottom regions of WE43 deposition. The basal plane $< 0001 >$ has the highest texture intensity in all of the areas examined, which is common among magnesium alloys [83]. The texture changes from a more randomized texture in the feedstock to a banded texture in the depositions for the planes $< 1010 >$ and $< 1120 >$. Friction stir processed WE43 [84] and FSAMed WE43 [24] both showed similar banding texture. This texture change is thought to be the result of severe plastic deformation in AFSD.

Here, the texture of other alloys is discussed besides lightweight alloys such as magnesium and aluminum alloys. Fig. 46 shows the PFs for the feedstock and deposit for Cu. The texture of the feedstock is close to $\{ 111 \} < 011 >$ (Fig. 46). Although a strong pole near (111) is shown in Fig. 46, the deposit does not appear to have a well-defined texture. Similar weak texture density results are shown in [29]. Fig. 47 shows the PFs and IPFs for the as-deposited titanium alloy Ti-6Al-4V. Regardless of the different combinations of process variables, there is no preferential selection of any particular α variant. When compared to the feedstock samples, the texture density of $B2$ and $B3$ increases [27].

In summary, the deposited microstructure is governed by plastic deformation and resultant recovery and recrystallization, which are highly dependent on process variables and chemical composition of deposited alloys. Generally, the AFSDed samples exhibit more equiaxed grains with reduced grain size due to dynamic recovery and recrystallization. Meanwhile, the precipitate resolves and re-precipitates, which affects the shape, size, and distribution of the precipitates. As a result, the properties of the deposited components are significantly affected by the microstructure, which will be discussed in detail in the following section.

4. Mechanical properties

The strength, ductility, fatigue behaviors, and impact toughness of metallic AFSDed components are discussed in this section, with an emphasis on property homogeneity. Because of the high-temperature gradients and cooling rates in fusion-based AM, dendrites grow closely aligned with the maximum heat flow direction at the solid–liquid interface, resulting in columnar crystal solidified structure in the manufactured parts [85,86]. The anisotropy of mechanical behaviors in fusion-based AM processes is caused by the solidified columnar

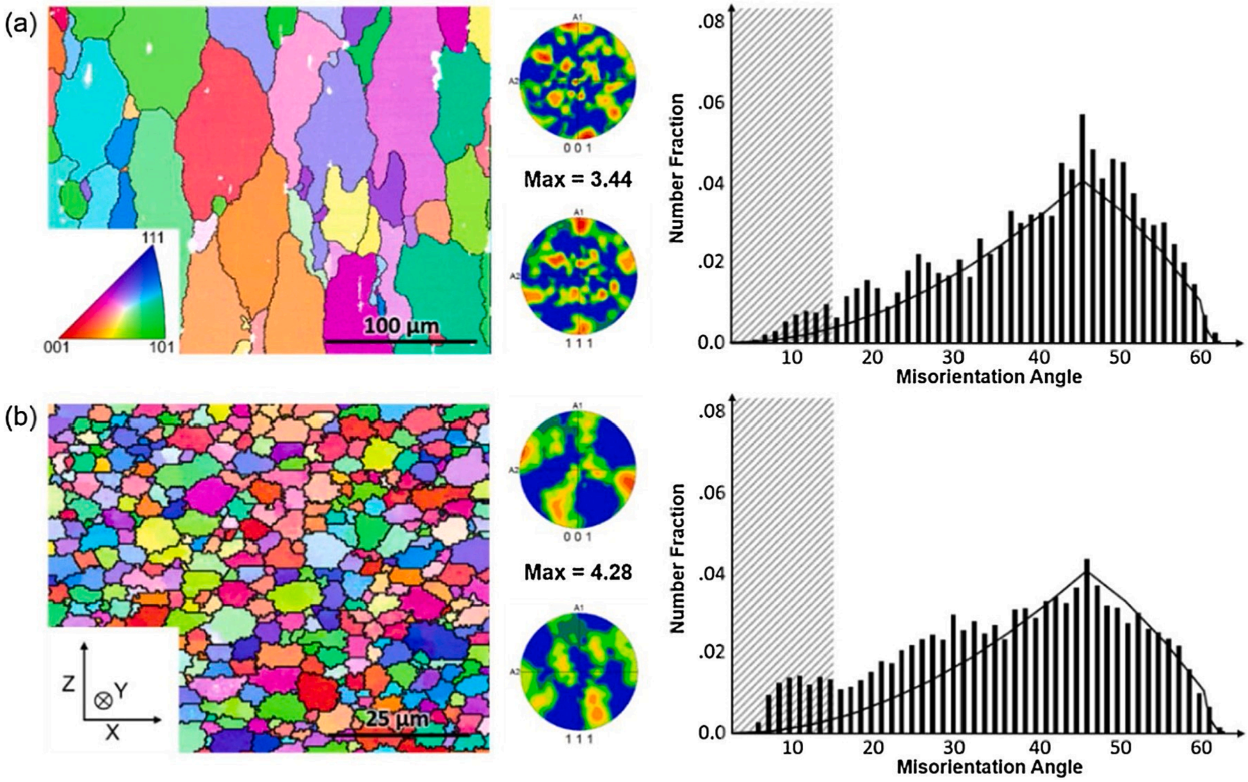

Fig. 38. IPFs, pole figures (PFs), and misorientation angle distribution of (a) as-received AA 2024 feedstock material and (b) as-deposited AA 2024 [52].

structure. Furthermore, the cast-like microstructure and defects in fusion-based AM reduce property. As stated in Section 3, full equiaxed structure can be obtained in the AFSD process, resulting in deposited parts with homogeneous properties and possibly comparable properties to wrought parts.

4.1. Microhardness

Despite the grain boundary strengthening associated with grain refinement in AFSD processes, precipitates such as Mg_2Si are solutionized and dissolve into the aluminum matrix under elevated temperature and dislocation shearing [74], causing the deposited material to soften. As a result of the softening effects caused by the change in precipitate size and number density described in Section 3.3, the as-deposited samples have much lower hardness. The microhardness increases significantly after proper solution and aging treatment. For example, the microhardness of as-deposited AA6061 samples is 75 ± 6 HV while the microhardness of feedstock rod is 135 ± 4 HV. Because of the proper precipitate strengthening, the microhardness of the deposit increases to 130 ± 5 HV after solution treatment and aging [26].

However, high temperature solution treatment may cause grain coarsening, weakening the grain boundary strengthening effect. Similar hardness reduction has been observed [51], as shown in Fig. 48. Such effects have also been observed in AFSD of other aluminum alloys [29,69], and magnesium alloys [87]. However, for non-precipitation hardening materials such as St-52 low carbon steel, the microhardness of the deposit (~ 400 HV) is much higher than the as-received feedstock (~ 235 HV) due to the martensitic phase transformation [88].

Location and process variables are two other important factors that influence the microhardness of AFSDed samples. It has been reported that a radial drop in hardness at the deposit's cross section deviates outward from the center [89]. The correlation between varying process variables for Al-Mg-Si alloys during AFSD is shown in Fig. 49. The microhardness of the deposit varies differently with location under different process variables, as shown in Fig. 49(c) and (d). The average hardness increases as the rotational speed and transverse velocity increase (Fig. 49(a)). There is no obvious relationship between microhardness and deposition feeding rate (Fig. 49(b)) [68].

4.2. Tensile strength

Although only a few aluminum alloys are weldable in fusion-based AM, due to the solid-state nature of AFSD, many more aluminum alloys are usable. Aluminum alloys are currently the most frequently investigated alloy in AFSD. Fig. 50 shows true stress–strain curves for as-received, as-deposited, and heat treated (HT) AA6061. Due to the lack of strengthening precipitates, the deposits have lower yield strength (YS) and ultimate tensile strength (UTS) than the wrought samples. However, the deposits have higher ductility due to increased dislocation motion under less β'' pinning. Significant property improvements can be obtained after proper heat treatment [76]. Other aluminum alloys have shown similar property reduction in the deposit and property improvement after heat treatment, as summarized in Table 2.

Aside from overall properties, researchers have been particularly concerned about property homogeneity. The stress–strain curve for AFSD AA5083 deposits is depicted in Fig. 51 along longitudinal direction and building direction. The reduction in strength and ductility along building direction is thought to be related to interfacial microstructural inhomogeneity and defects present in the layer-by-layer process [53]. Aside from the differences in property along different directions, samples obtained from the top, middle, and bottom layers differ in tensile behaviors (Table 3). The inhomogeneous texture and precipitates along building direction cause an increase of YS and UTS with a slight decrease in elongation present from the top to the bottom layer [72]. However, other research shows the hardness drops from the top surface to the bottom and after about 20 mm (~ 13 layers), the

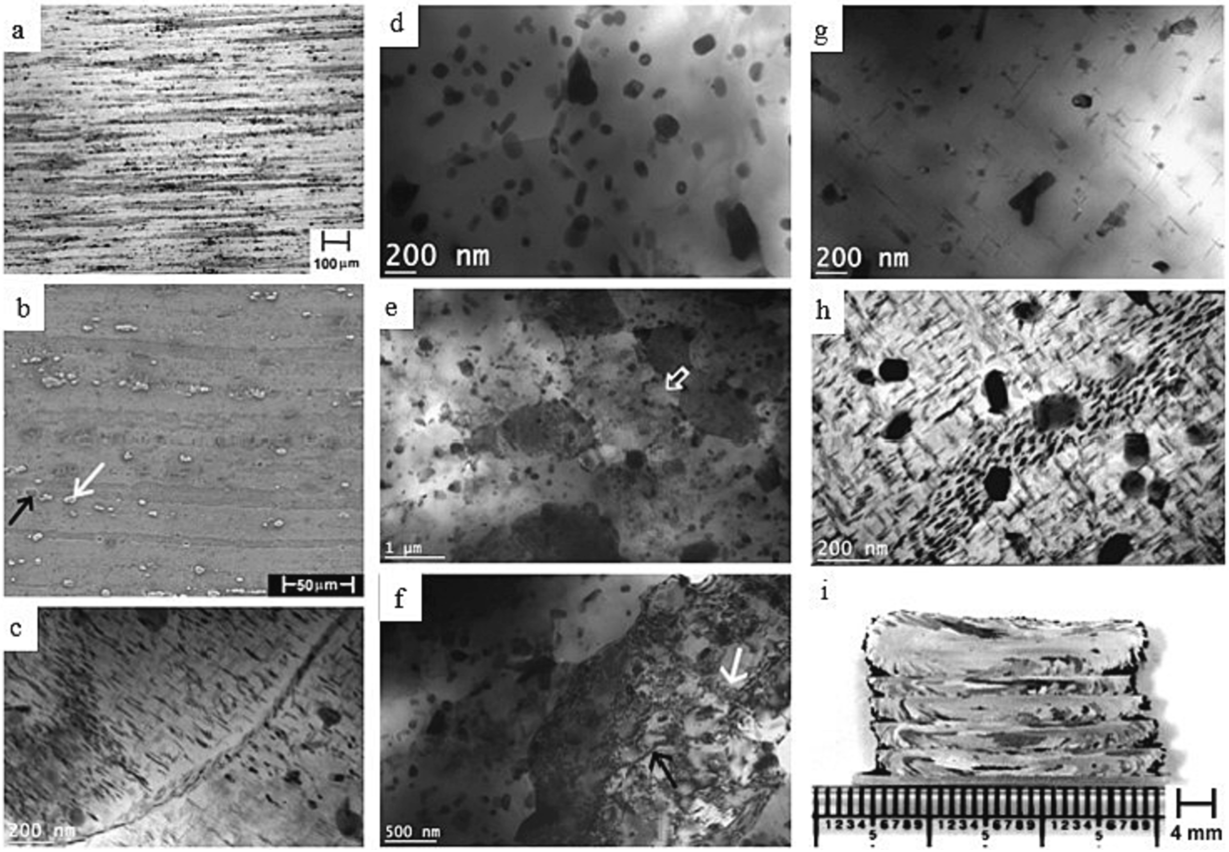

Fig. 39. Microstructure of the consumable AA2014 rod: (a) optical microscope, (b) SEM, and (c) TEM. TEM microstructure images of the deposit with: (d) over-aged precipitates, (e) cell formation in a grain, and (f) further cell formation in a grain. Microstructure of the deposits after different heat treatments: (g) TEM images for the deposit in direct aged condition, (h) TEM images for the deposit in solution treated + aged condition, and (i) macrograph of the abnormal grain growth in the deposit in solution treated + aged condition [26].

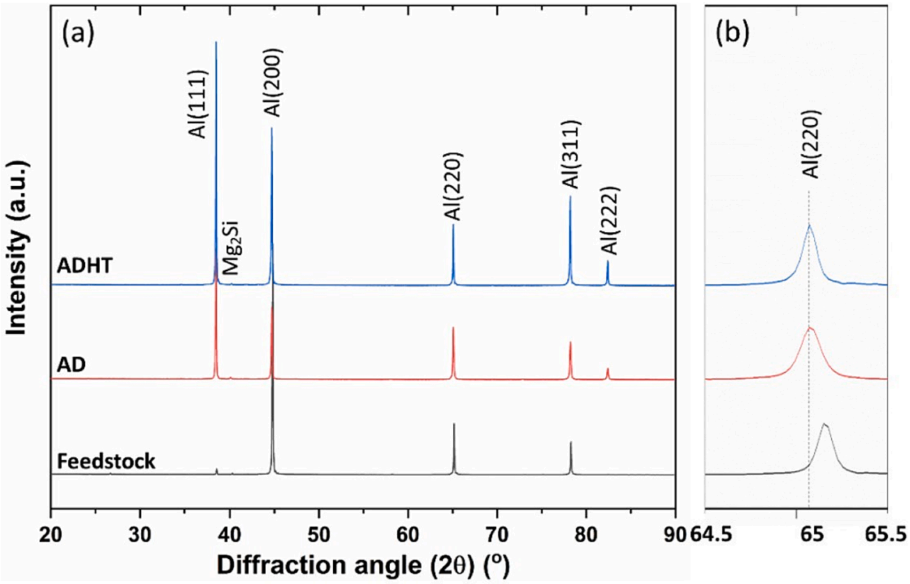

Fig. 40. XRD patterns of (a) AFSDed AA6061 deposits in as deposited sample after heat treatment, as-deposited, and as-received conditions, and (b) samples over a narrow diffraction angle range [71].

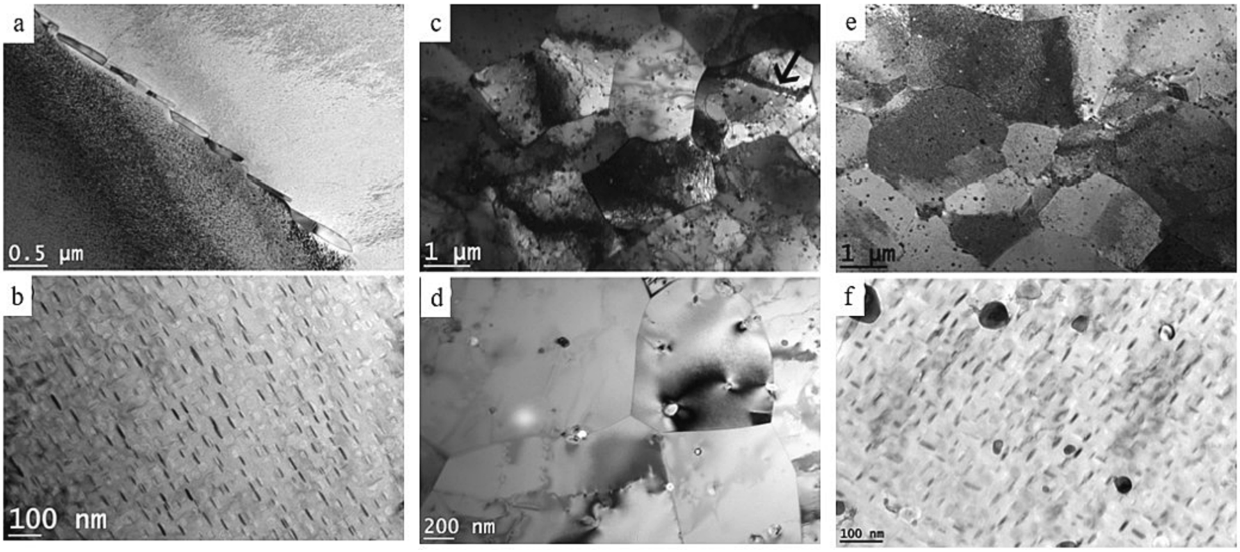

Fig. 41. Bright-field TEM micrographs of solution-treated and aged Inconel 718 rods: (a) plate-like δ phase precipitates at grain boundaries and (b) disk-shaped γ'' strengthening precipitates. TEM micrographs of the deposits: (c) fine recrystallized grains with varying dislocation densities and numerous carbides particles with a developing cell boundary indicated by the arrow. And (d) the absence of γ'' strengthening precipitates and δ grain boundary precipitates. TEM micrographs of the deposits after direct aging at (e) low and (f) high magnifications and γ'' strengthening precipitation is apparent with fine carbides in the shape of dark spherical particles [33].

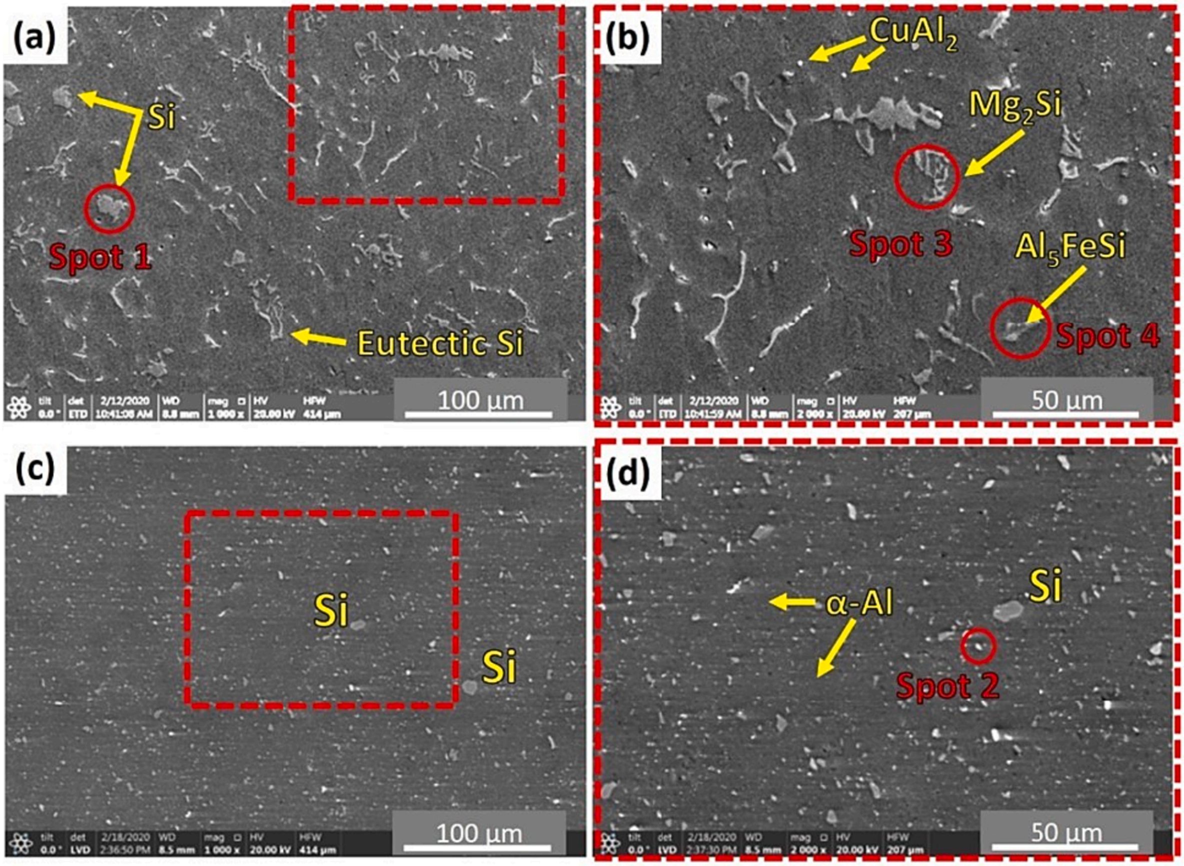

Fig. 42. SEM micrographs of the as cast alloy (a) low magnification and (b) high magnification; of the deposit (c) low magnification and (d) high magnification [77].

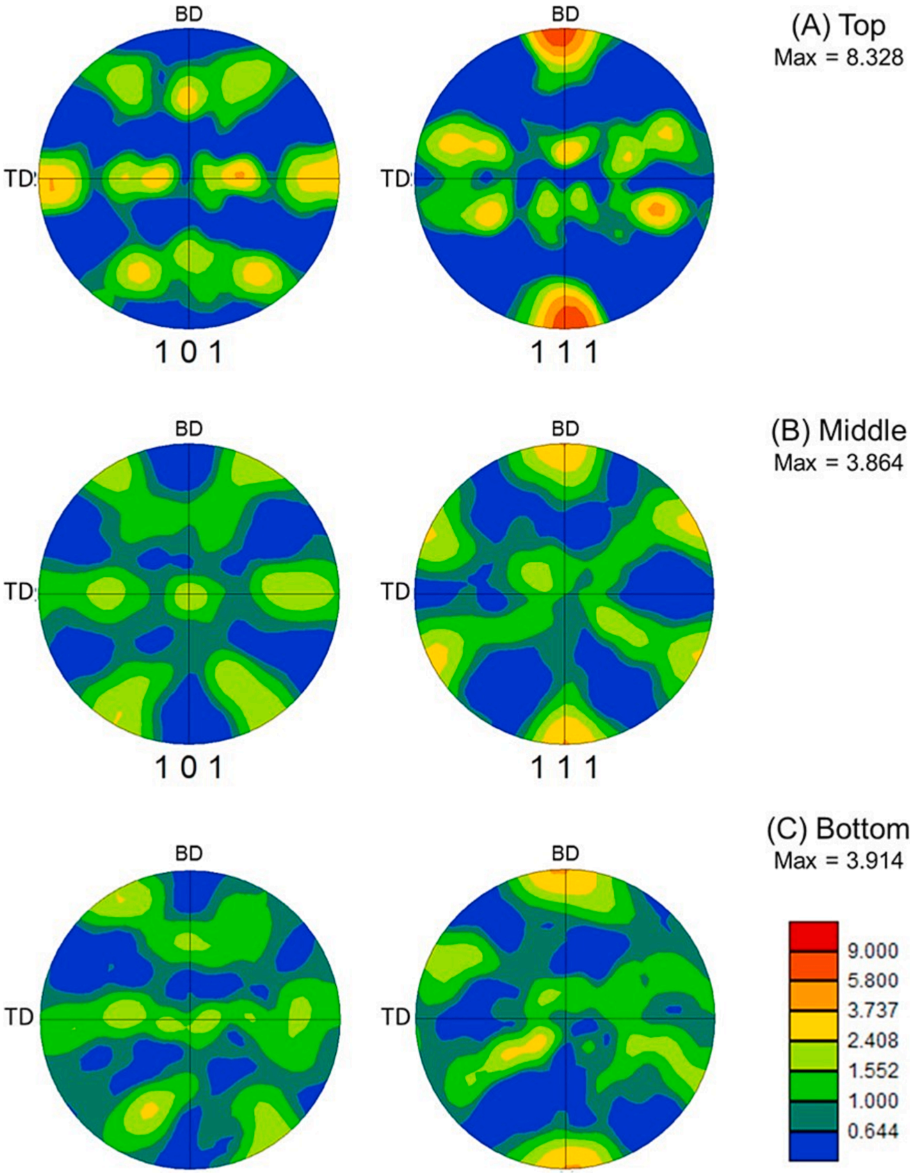

Fig. 43. EBSD texture plots of the as-deposited AA2219 in (A) the top, (B) the middle, and (C) the bottom of the deposit [72].

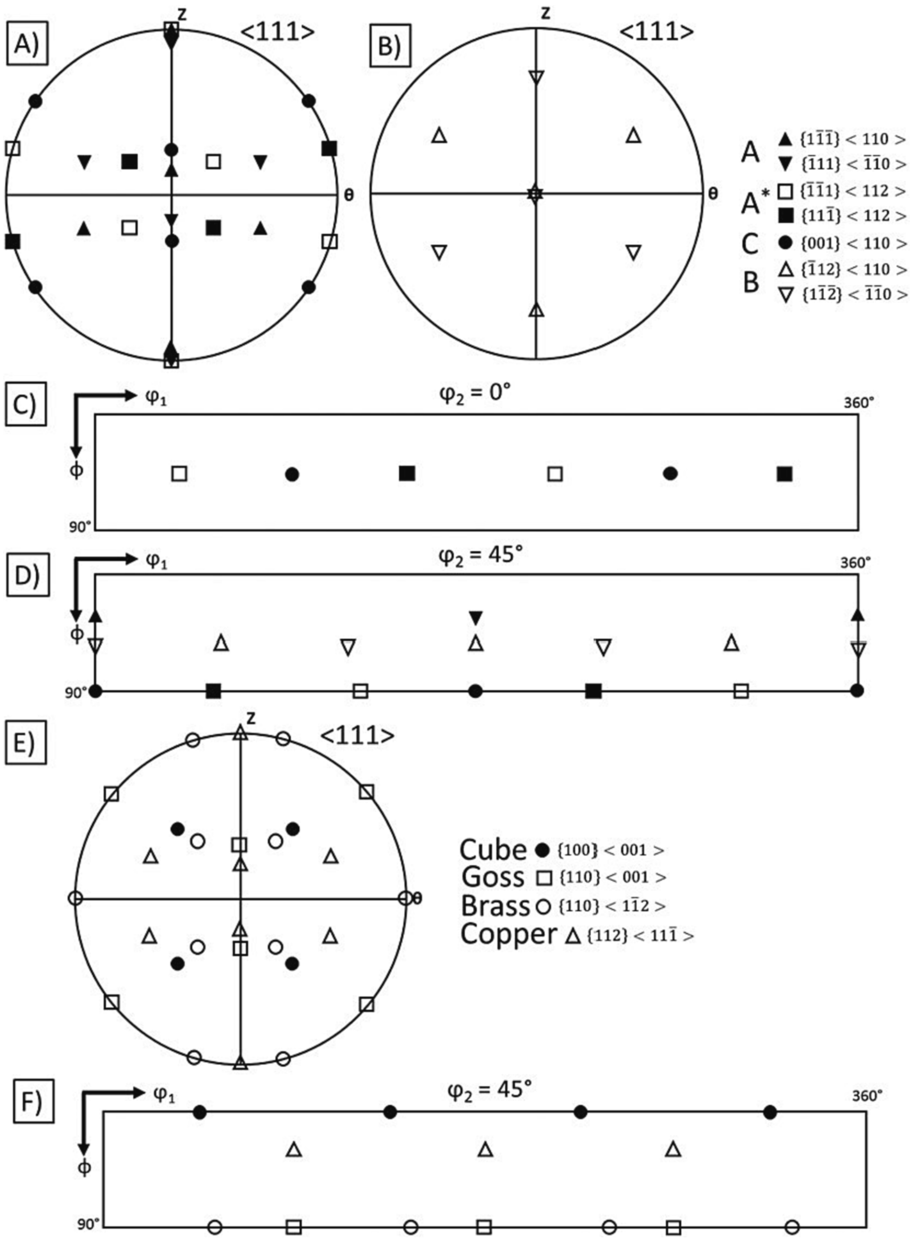

Fig. 44. Schematic diagrams of common texture orientations for FCC aluminum reported in [81,82]. (A) PF representing the ideal torsional textures for FCC aluminum components A, A*, and C. (B) PF representing the ideal torsional texture for FCC aluminum component B. (C) ODF at $\phi_2 = 0^\circ$ showing the ideal torsional texture components locations. (D) ODF at $\phi_2 = 45^\circ$ showing the ideal torsional texture components locations. (E) PF representing the common rolling and recrystallization texture components for FCC aluminum. (F) ODF at $\phi_2 = 45^\circ$ displaying the common rolling and recrystallization texture components location.

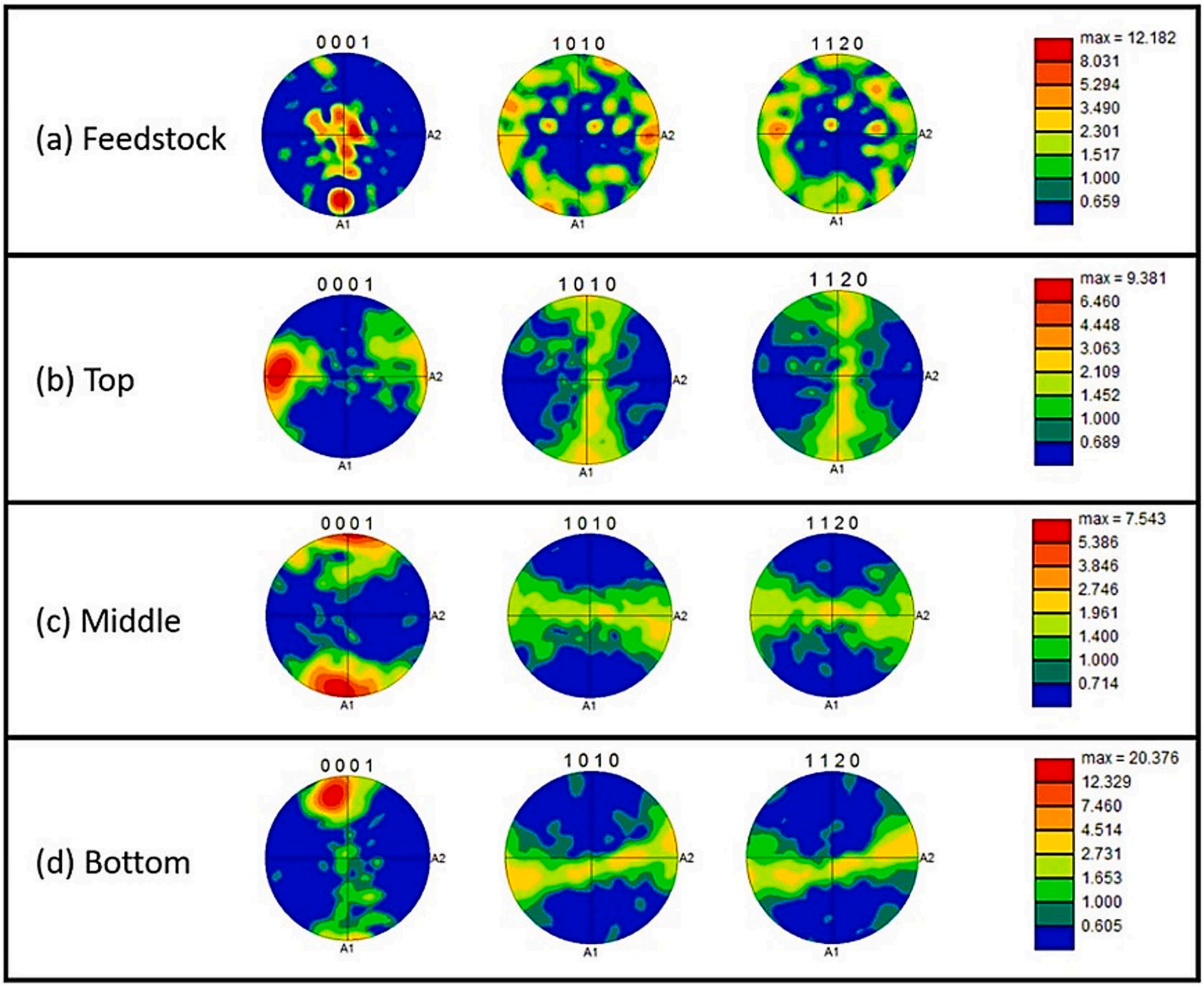

Fig. 45. Representative texture plots for the (a) WE43-T5 feedstock material, as well as for the (b) top, (c) middle, and (d) bottom of the deposit [32].

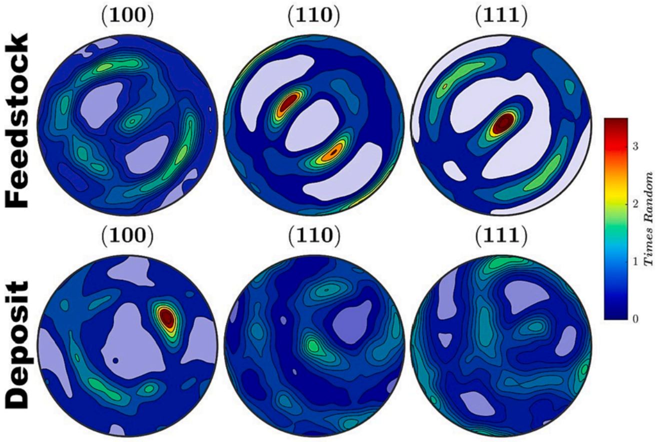

Fig. 46. PFs for the Cu feedstock and the deposit [34].

hardness approaches a steady value. They assume that YS and UTS are expected to follow the same trend [91]. Still, more researches are needed to better understand the property homogeneity of AFSDed parts.

Magnesium alloys, another common lightweight alloy, have also been used in AFSD. A similar reduction in property has been observed in deposited WE43 samples (Fig. 52). The coarsening of strengthening precipitates is the cause of the decreased mechanical properties when compared to wrought feedstock [32]. However, in work-hardened magnesium AZ31 alloys, grain refinement can compensate for the loss of strength, as shown in Table 4 [28]. For as-deposited magnesium alloys, the property difference along building direction is also reported [87].

In addition to lightweight alloys, superalloys such as nickel-based and titanium-based have been studied in AFSD. AFSD has successfully deposited higher strength Inconel 625 and 718. The tensile properties of Inconel 625 manufactured by various processes are summarized in Table 5. As a result of its refined, full-equiaxed microstructure, AFSD samples have the highest tensile properties [70]. Superior strength at high strain rate has been demonstrated for as-deposited Inconel 625 samples in Fig. 53. Similar property enhancement results have been demonstrated in as-deposited Inconel 718 (Fig. 54). However, at 923 K, the as-deposited Inconel 718 samples exhibit poorer stress rupture behaviors, which can be overcome with additional solution and aging treatment [33].

Due to the wide application in the aerospace industry, Ti-6Al-4V is currently being studied among the many Titanium alloys. Fig. 55 shows the engineering stress–strain curve for Ti-6Al-4V deposits sampled at different directions, layers, and process variables. As shown in Fig. 55 (a), the deposited samples have YS in the range of 1025 ± 25 MPa, UTS in the range of 1140 ± 20 MPa, and elongation in the range of 7 ± 1 %.

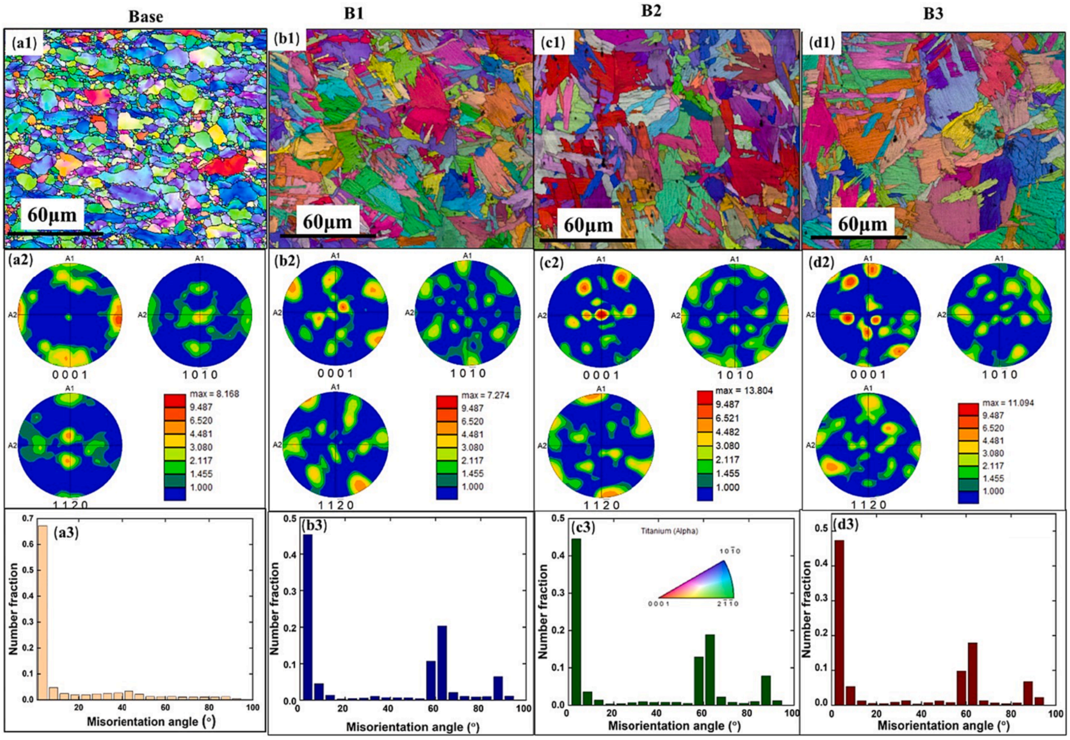

Fig. 47. The first row images (a1), (b1), (c1), and (d1) show IPFs; the second row plots (a2), (b2), (c2), and (d2) show PFs; and the third row plots (a3), (b3), (c3), and (d3) show misorientation angle profiles for an as-received Ti-6Al-4V sample and three deposits under different process variables, respectively [27].

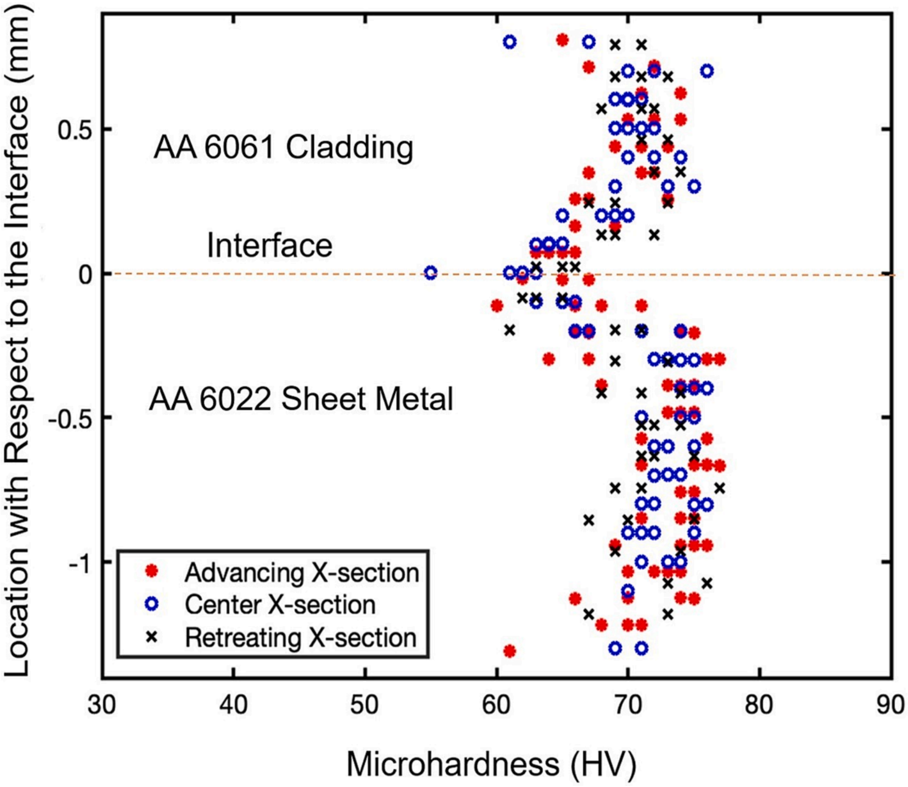

Fig. 48. Vickers hardness plotted along several LD-ND cross-sections, including data from the centerline, advancing, and retreating sides of the deposit [51].

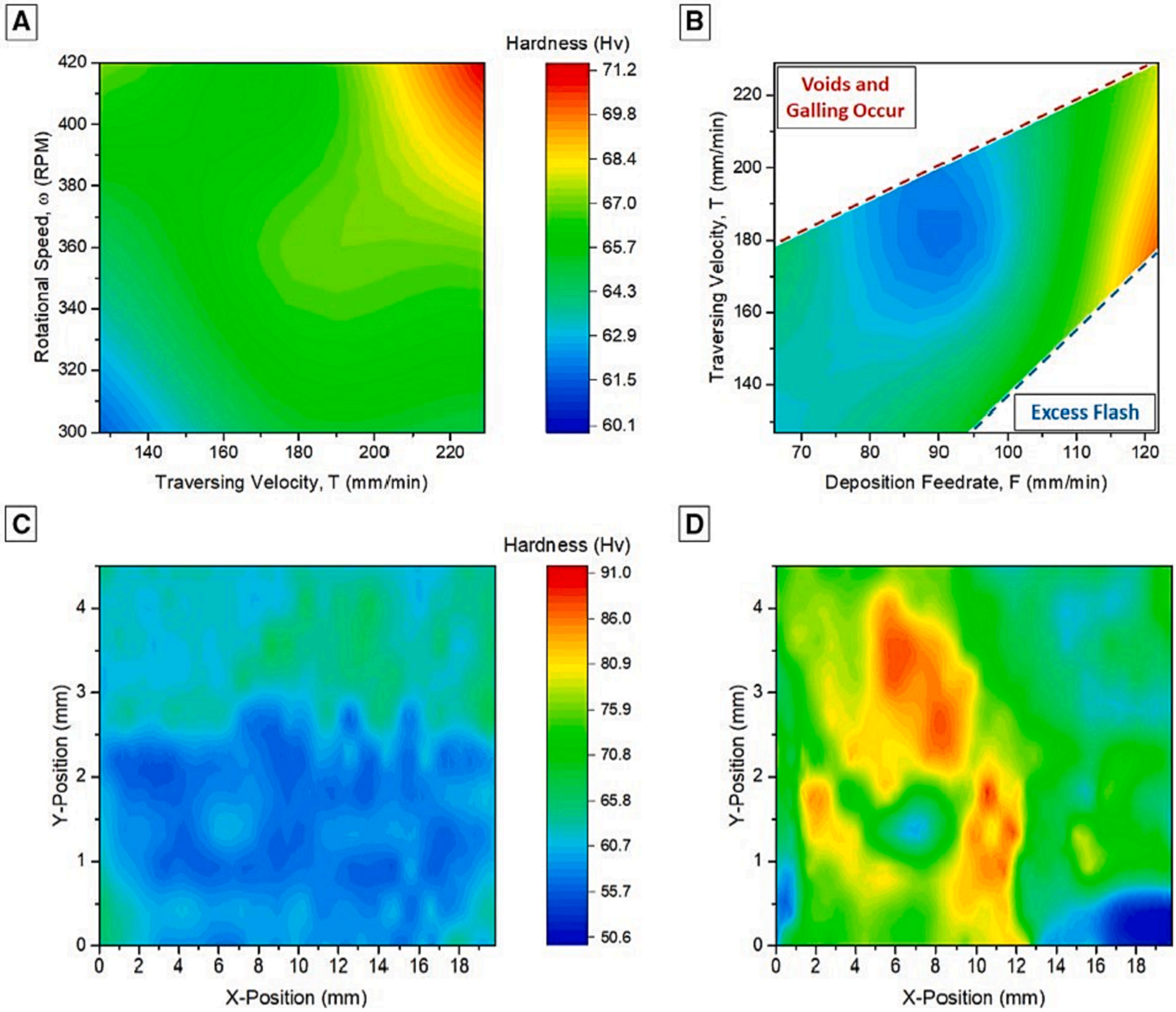

Fig. 49. Parameter contour plots relating (A) tool rotational and traversing speed to average deposition hardness and (B) tool traversing speed and deposition feed rate to average deposition hardness. (C) A Vickers hardness plot of a low-parameter AFSD deposit. (D) A Vickers hardness plot of a rapid-parameter deposit [68].

The forged Ti-6Al-4V has a YS of 799 MPa, a UTS of 894 MPa, and an elongation of 18.6 % [75]. This increase in tensile strength is due to grain refinement caused by the severe deformation in AFSD. Given the interfacial microstructural inhomogeneity, the sample along longitudinal direction has a higher YS (1200 ± 5 MPa) than the sample along building direction (1060 ± 8 MPa) (Fig. 55(b)). As shown in Fig. 55(c), specimens taken from different layers exhibit different stress strain curves as a result of microstructural variation along the building direction [27]. As with nickel and titanium alloys, as-deposited steel alloys such as SS304 [20] and St-52 low carbon steel [88] have improved strength. Different mechanisms are at work, as the improvement for as-deposited steel samples is caused by strain-induced martensitic deformation under severe deformation in AFSD.

It can be concluded that as-deposited samples have inferior properties to as-received samples for aluminum alloys, whereas as-deposited samples have superior properties for titanium alloys, nickel alloys and ferrous alloys. This phenomenon is caused by the different strengthening mechanisms used by different alloys. The main mechanism for Al alloys is precipitate strengthening, and the as-received Al feedstock is frequently provided in its optimal solutionizing condition. Precipitates in the feedstock resolve during deformation at high temperatures in AFSD. The re-precipitation during cooling is not optimal, resulting in a softening effect for deposit properties. However, for alloys whose primary strengthening mechanism is Hall-Petch or interfacial strengthening, grain refinement caused by recovery and recrystallization during AFSD results in better properties in as-deposited samples. As shown in Eq. 1, multiple factors contribute to the YS of a material. The properties of alloys with different primary strengthening mechanisms respond differently to AFSD. The competition or balance between grain boundary strengthening (Hall-Petch strengthening) and precipitation strengthening mechanism in AFSD necessitates additional research in order to achieve tailored properties aimed at realistic applications.

$$\sigma_Y = \sigma_O + \sigma_{SSS} + \sigma_{WH} + \sigma_{HP} + \sigma_P + \sigma_{TXTR} \qquad (1)$$

where σ_Y is the material YS, σ_O is the Peierls-Nabarro stress [92], σ_{SSS} is the solid solution strengthening [93], σ_{WH} is the work hardening based upon dislocation density [94], σ_{HP} is the Hall-Petch strengthening [95], σ_P is the precipitation strengthening [96], and σ_{TXTR} is the texture strengthening [97].

4.3. Fatigue behavior and impact toughness

Fatigue behavior has long been a research priority, particularly for components used in industries such as transportation, aviation, and

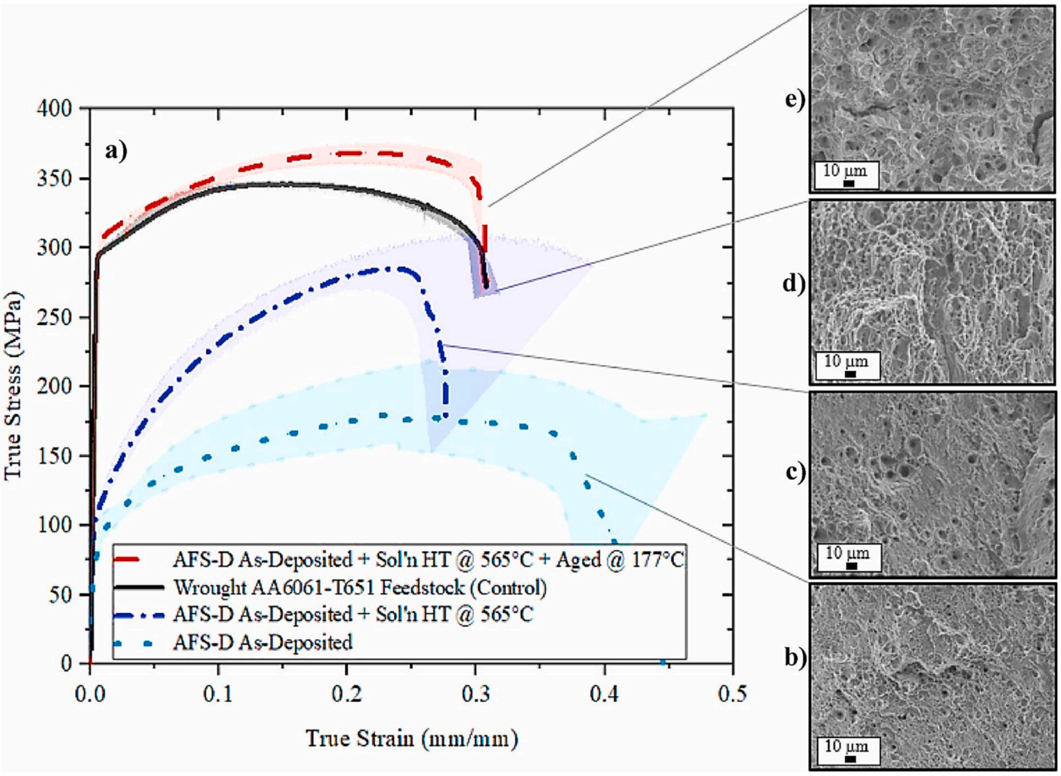

Fig. 50. (a) Averaged true tensile stress–strain curves of wrought AA6061-T651 (3 specimens), AFS-D AD (3 specimens), AFS-D SQ (3 specimens), and SQA (4 specimens) accompanied with (b-e) representative fracture surfaces [76].

Table 2
Tensile properties for different aluminum alloys under different conditions (BD-building direction, LD-longitudinal direction).

Alloys	Condition	YS/MPa	UTS/MPa	ϵ_f/%	Reference
AA5083	As-deposited	170.4 ± 7.5	368.0 ± 13.7	~ 18	[89]
AA7075	Wrought	502.1	575.5	10.5	[31]
	As deposited + solution treatment and aging	477	541	8.2	
AA5083	As-received	273.7 ± 1	410 ± 6.1	15 ± 2.4	[53]
	As-deposited, LD	151.3 ± 1.7	431.3 ± 1.9	30 ± 0.5	
	As-deposited, BD	157.7 ± 1.2	246.2 ± 45.9	8 ± 4.5	
AA6061	Wrought	295.8 ± 1.8	316.5 ± 2.2		[90]
	As-deposited, LD	61.3 ± 6.4	137.1 ± 14.8		
	As-deposited, BD	63.9 ± 2.7	129.9 ± 3.5		
AA1060	As-received	75.8	82.7	16	[60]
	As-deposited, LD	78	112.5	24.7	

automation. Because of the severe plastic deformation, as stated in Section 3, AFSD achieves significant grain refinement. Despite the fact that the grains in AFSD AA7075 samples are mostly refined, the fatigue life decreases from the feedstock data, as shown in Fig. 56. This decrease is due to the increased size of the strengthening phases [69]. The total fatigue life is strongly dependent on inclusion size, grain size, yield strength, ultimate strength, and cyclic properties, according to the microstructure-sensitive fatigue (MSF) model [98] and its application in AFSD aluminum alloy [69,90,99].

As-deposited WE43 alloy exhibits a similar reduction in fatigue life. The results of the stress-controlled fatigue tests for the WE43-T5 feedstock, as well as longitudinal and building direction for the AFSD WE43 deposition, are shown in Fig. 57. The strong relationship using normalized stress elucidates the reason for the reduction in life. It is because low life for building direction samples is tested at > 90 % of its UTS level while high life for feedstock samples is tested at < 60 % of its UTS level. It can be understood that the decrease in as-deposited fatigue life is caused by the same factor that causes the decrease in monotonic properties. It is worth mentioning that, despite the fact that the as-deposited samples have inferior fatigue and monotonic strength, both properties along the longitudinal direction are better than along the building direction [32].

The coarsening of strengthening precipitates is responsible for the reduction of as-deposited properties. Yet, further reduction along the building direction is believed to be related to oxidation and carbides from the graphite coatings on the feedstock becoming entrapped in layer interfaces [59,100]. Thus, process optimization and post heat treatment improve both monotonic properties and fatigue life [76]. Superior fatigue life along longitudinal direction is observed in strain-controlled fatigue tests at low strain amplitudes of 0.2 % and 0.3 %, as shown in Fig. 58. This improvement in fatigue properties is the result of particle refinement caused by large particle fracture under plastic deformation [90].

Therefore, investigations into crack nucleation and growth may be a future direction. This is because the unique microstructure displayed in AFSD samples (as stated in Section 3) opens up new possibilities for crack behaviors. The fatigue nucleation and growth mechanisms in AFSD, as investigated in [90], are likely to be driven by constituent

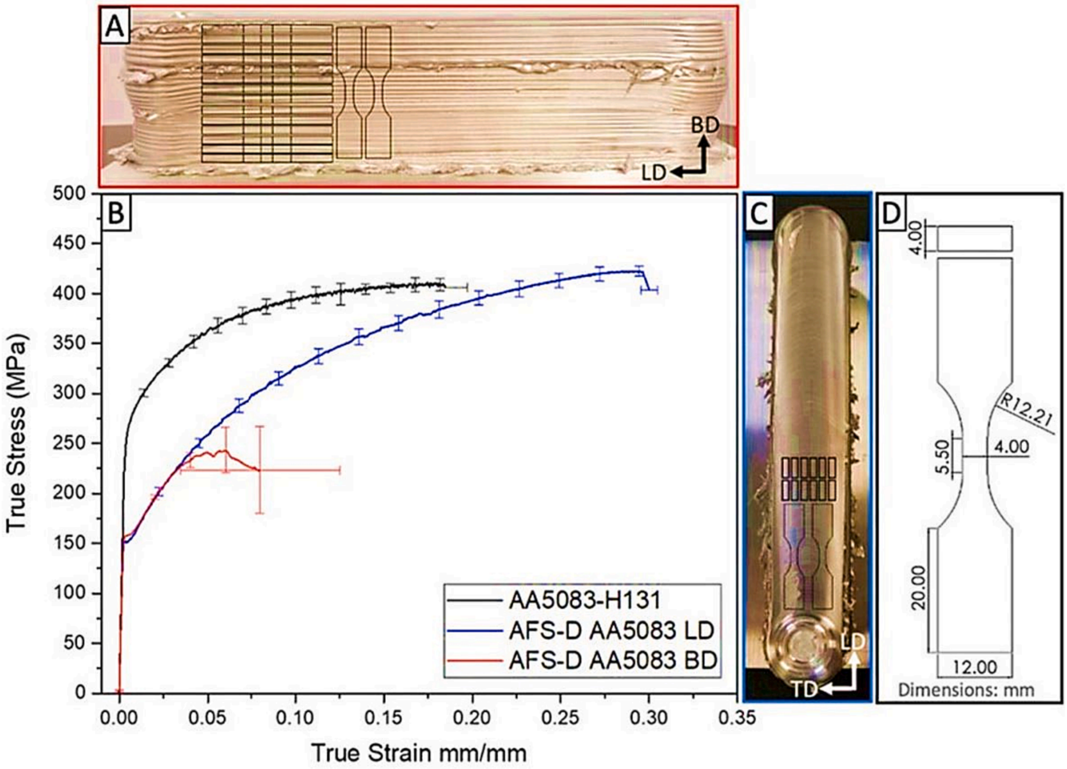

Fig. 51. (A) Side view of the AFS-D AA5083 deposit showing the sampling locations. (B) Tensile stress strain curves of the wrought AA5083-H131 feedstock and as-deposited AA5083. (C) Top view of the AFS-D AA5083 deposit; and (D) sample geometry used [53].

Table 3

Comparison of YS, TS, and ϵ_f of as-deposited AA2219 at various locations and strain rates [72].

Location	Top		Middle		Bottom	
Strain rate	0.001/s	2500/s	0.001/s	2500/s	0.001/s	2500/s
YS(MPa)	159 ± 0.7	275 ± 0.6	140 ± 1.0	242 ± 4.2	125 ± 3.5	225 ± 4.2
TS(MPa)	390 ± 2.1	283 ± 1.4	364 ± 5.2	245 ± 1.4	335 ± 7.1	236 ± 8.5
ϵ_f(%)	25 ± 0.7	37 ± 0.7	27 ± 2.1	41 ± 0.7	28 ± 1.4	42 ± 2.1

particles. The latter differs from the porosity-based fatigue mechanisms in fusion-based AM techniques.

Impact toughness is another focus for engineering practice, particularly in the vehicle and mold industries. The impact toughness of magnesium WE43 alloys has been studied by Calver et al. [87]. The average impact results are shown in Table. 6, and the fracture surface topography results are shown in Fig. 59. Although the as-deposited samples show similar or slightly higher results than the as-received samples, the fracture surface topography differs between them. The fracture surfaces are smooth and flat in the as-received samples with slightly lower impact toughness as observed in Fig. 59(c-d). In the magnified topography images (Fig. 59(c-d)), there are also signs of brittle and ductile fracture, as well as *trans*-granular cleavage and ductile tears joining cleavage planes.

The fracture surfaces of as-deposited samples with higher impact toughness exhibit fine trans-granular tearing features with sizes that match well with grain size and no clear intergranular facets (Fig. 59(e-f)). According to the fracture topography results, the slightly improved impact toughness for as-deposited samples is the result of grain refinement. However, there is no discernible improvement from grain strengthening, which could be attributed to the lack of precipitate strengthening. There are currently few studies on the impact behaviors of AFSD parts, and further research into the improvement of impact toughness is required in the future.

To sum up, the mechanical properties of AFSDed components are highly dependent on the deposited microstructure. Refined grain size and re-precipitated precipitates are two major characteristics of as-deposited microstructure. Regardless of the impact of different processing conditions, for alloys whose primary strengthening mechanism is Hall-Petch strengthening like titanium alloys, the as-deposited samples exhibit superior properties compared to as received samples. But for those alloys that precipitation strengthening mechanism plays a vital role in like aluminum alloys, the balance between different strengthening mechanisms makes it difficult to predict the properties of as-deposited samples. Another important thing about properties is anisotropy. On the whole, the properties along building direction are inferior to other directions due to the weaker bonding strength among layers.

5. AFSD vs fusion-based AM

Fusion-based AM technologies adopt high energy beams such as laser beam and electron beam to melt alloy powder or wire. Components with predefined features are being manufactured concurrently with the subsequent solidification process. The temperature inside the molten pool can be significantly higher than the melting temperatures of the alloys. The peak temperature of Inconel alloy in directed energy deposition (DED) reaches as high as 2500 K [101], while the peak temperature of aluminum alloy can exceed 3000 K [102].

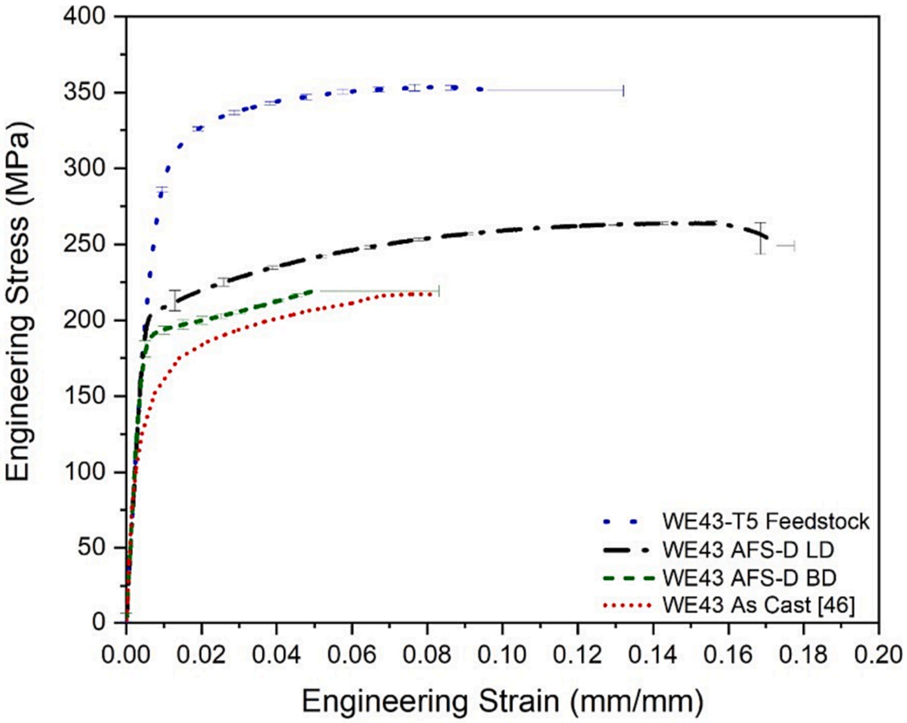

Fig. 52. Stress–strain plot comparing the quasi-state tensile test results of the WE43-T5 feedstock, longitudinal direction, and building direction of the bulk WE deposition [32].

Table 4
Tensile properties of a magnesium block and deposit along different directions. L, T, and ST stand for longitudinal, transverse, and short transverse, respectively [28].

Condition	TS/MPa	Engineering strain/%
Base metal AZ31B-H24 (L)	264 ± 1	20 ± 1
Base metal AZ31B-H24 (T)	267 ± 2	19 ± 3
Base metal AZ31B-H24 (ST)	293 ± 5	23 ± 1
Deposit (L)	254 ± 4	14 ± 2
Deposit (T)	264 ± 2	18 ± 1
Deposit (ST)	333 ± 2	19 ± 1

Table 5
Comparison of the tensile properties of Inconel 625 manufactured using different processing techniques [70].

Condition	YS/MPa	UTS/MPa	ϵ_f/%
Cast	350	710	48
Wrought	490	965	30 ~ 50
AFSD	730	1072	32

Rapid melting and solidification are also involved in fusion-based AM technologies, resulting in a high temperature gradient ($10^2 \sim 10^4$ K/mm) and fast cooling rate ($10^3 \sim 10^6$ K/s). However, due to its solid-state temperature, AFSD does not melt or solidify. The peak temperature is in the 50 % ~ 90 % range of the melting temperature. And the heating and cooling rates for AFSD are approximately $10^1 \sim 10^2$ K/s and 10^1 K/s, respectively. These distinctions cause these two types of AM technologies to differ in process physics, structure and property, and so on.

5.1. Process

Fusion-based additive manufacturing techniques have been around for over 30 years with decades of focused research and are now widely accepted as a new paradigm for the design and production of high performance metallic components in the aerospace, aviation, automation, medical, and energy industries. Porosity and cracks are common flaws in fusion-based AM techniques. The main impediment preventing fusion-based AM from achieving wider application in metals such as aluminum alloys is the solidification cracking. AFSD, unlike fusion-based AM, can potentially fabricate fully-dense and crack-free components due to the solid-state nature of the process. In essence, the printability of AFSD material is unlimited.

However, AFSD has its own issue, which is the low accuracy of as-made parts. Typically, AFSDed parts require CNC machining before they can be used. The feedstock rod in AFSD is around 10 mm, whereas the feedstock material in fusion-based AM is around 10~100 μm (powder) or 1 mm (wire). As shown in Fig. 1, the building rate of AFSD is approximately ten times that of fusion-based AM. In comparison to LPBF, AFSD can deposit large-scale components as large as possible without the constraint of a chamber. In comparison to DED, AFSD has a higher building rate and can deposit larger components due to its larger feedstock material.

Despite its advantage in large-scale part manufacturing, AFSD cannot produce components with highly complex structures and small feature sizes. While fusion-based AM can capture features as small as 10 μm, AFSD can only capture features as the layer thickness (over 1 mm). The maximum overhang angle and highest aspect ratio are limited in AFSD due to the compressive force applied to the deposit. Furthermore, the loss of alloying element that occurred in fusion-based AM [103] does not occur in AFSD.

5.2. Microstructure

During the rapid melting and solidification of fusion-based AM, the melt pool conducts heat into the substrate, forming a curved solid–liquid interface. During solidification, crystals grow competitively from the substrate or previously deposited layers. In polycrystalline materials, competitive growth occurs among dendrites with different crystallographic orientations [104]. Dendrites with easy-growth directions grow along the maximum heat flow direction at the solid–liquid interface.

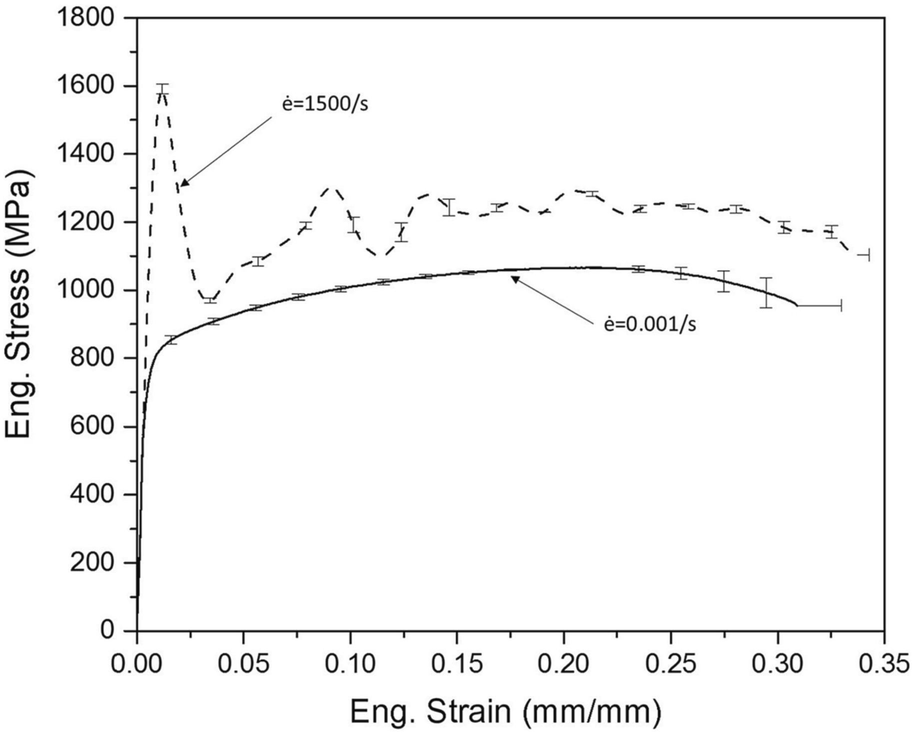

Fig. 53. Tensile results of the AFSDed Inconel 625 samples comparing the quasi-static (0.001/s) to the high rate (1500/s). For the quasi-static rate case, the YS, UTS, and strain to failure for the quasi-static case are 730 MPa, 1072 MPa, and 0.32, respectively. For the high-rate case, the YS, UTS, and strain to failure are 1587 MPa, 1592 MPa, and 0.34, respectively [70].

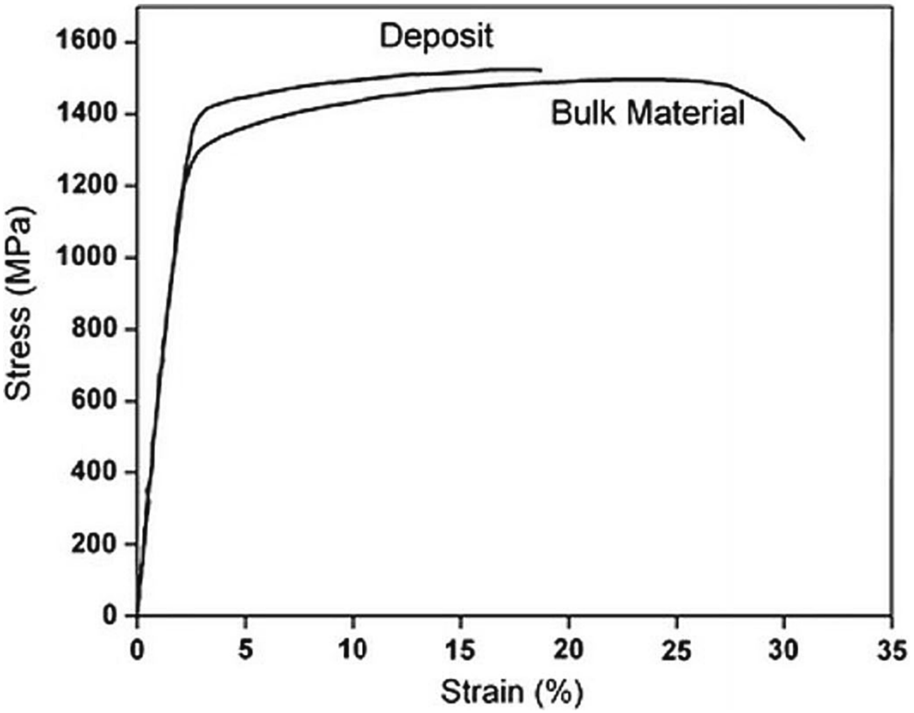

Fig. 54. Stress–strain curves for Inconel 718 produced through AFSD process (Deposit) and standard wrought-processed along with heat-treatment (Bulk Material). For the Deposit case, the 0.2 % proof stress, UTS, and elongation are 1200 MPa, 1440 MPa, 14 %, respectively. For the Bulk Material case, the 0.2 % proof stress, UTS, and elongation are 1150 MPa, 1410 MPa, 22 %, respectively [26].

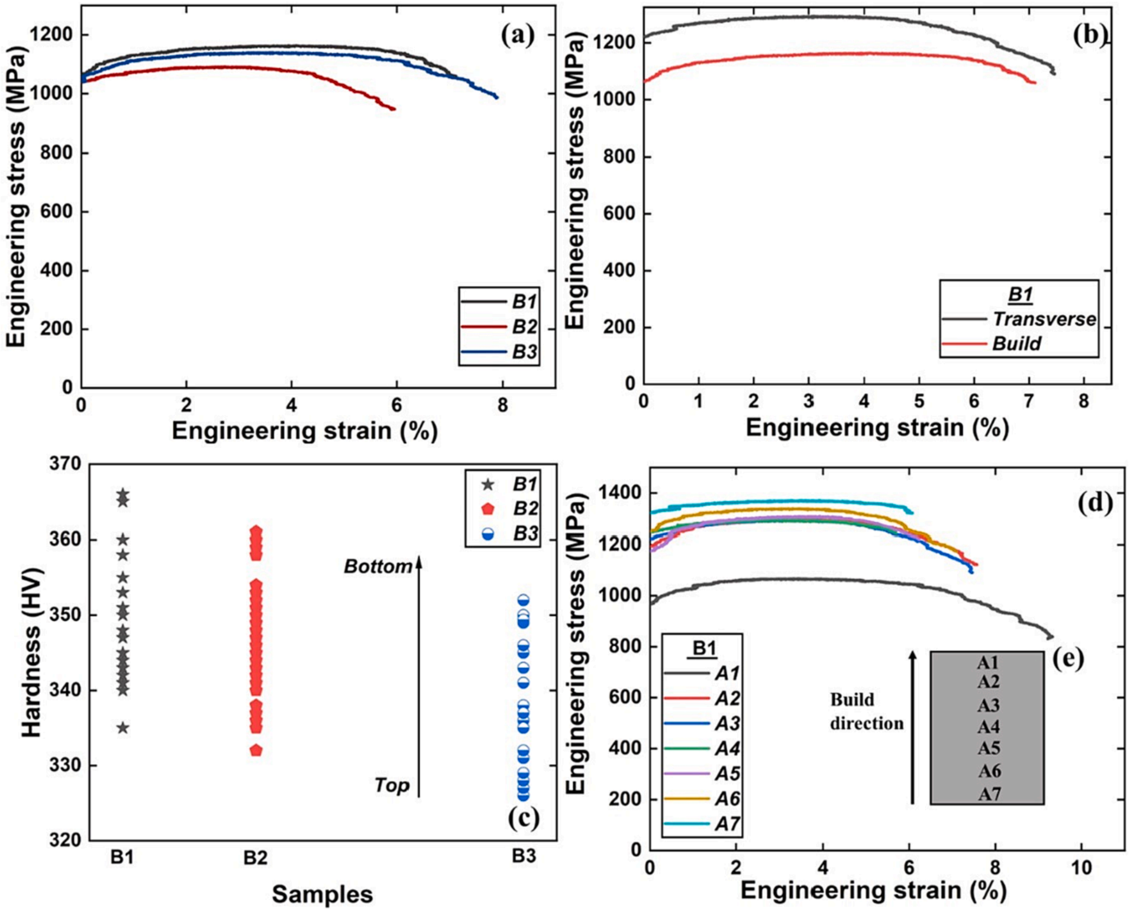

Fig. 55. (a) Engineering tensile stress–strain curves for Ti-6Al-4 V samples deposited at different deposition parameters. (b) Engineering stress–strain curves for samples taken from the building and transverse direction. (c) Hardness variation with deposition parameters. (d) Engineering stress–strain curves for samples taken from different locations; and (e) schematic diagrams of sample A1-A7 location along the building direction [27].

Finally, columnar structures form when dendrites that are more aligned with the temperature gradient outgrow slower-growing misaligned dendrites [85,86]. Several approaches have been explored to achieve columnar to equiaxed grain transition in fusion-based AM, such as adding ceramic nanoparticles into the metal matrix [4].

Unlike fusion-based AM, the as-deposited components in AFSD show a refined, fully equiaxed structure because it is deformed and evolved due to dynamic recovery and DRX, as stated in Section 3. Aside from the morphology of dendrites, precipitates and intermetallic particles differ between these two technologies. Precipitates in alloys first dissolve into the matrix during AFSD plastic deformation, and re-precipitation occurs during cooling. In fusion-based AM, however, the precipitates dissolve into the matrix due to melting, and re-precipitation rarely occurs due to rapid cooling. In AFSD, intermetallic particles are fragmented along with the deformation, whereas no such phenomenon occurs in fusion-based AM technologies.

Fig. 60 depicts the tensile strength and elongation of various AM technologies. In general, for magnesium (Fig. 60 (b)) and Inconel alloys (Fig. 60 (c)), the AFSDed samples have higher tensile strength but lower ductility than the fusion-based AMed samples. As for aluminum alloys (Fig. 60(a)), the AFSDed samples exhibit higher strength and better ductility than the fusion-based AMed samples. What worths to mention is that processing parameters play an important role in mechanical properties, which is the reason why the same alloys exhibit distinct mechanical properties. Essentially, the differences in strength and ductility are due to the various structures described in Section 5.2.

Given the difficulty to apply commercial aluminum alloy compositions developed for casting or wrought directly to fusion-based AM, data and research in aluminum alloys for fusion-based AM technologies is limited. The ability of AFSD to fabricate alloys unprintable in fusion-based AM, such as aluminum alloys, is a distinct advantage for additive manufacturing. Anisotropic properties are observed in both techniques, but for different reasons. The anisotropic columnar crystals in as-made parts cause anisotropic properties in fusion-based AM. However, the anisotropic layer difference due to defects in the layer-by-layer process and the deformed texture cause anisotropic properties in AFSD.

5.3. Summary

Fusion-based AM technologies involve rapid melting and solidification at high temperatures and relatively short time intervals (~ 10 ms). AFSD is a long-term (~ s) solid-state deformation process that occurs below the melting temperature. Despite the rapid development and widespread application of fusion-based AM technologies, AFSD has demonstrated significant potential in the production of large-scale parts and alloys that are not printable in fusion-based AM due to the presence of cracks and pores. The challenge for AFSD is to produce components with small feature sizes and complex geometrical properties and relative high strengths for fusion-based AM, particularly LPBF. Choosing the best-suited AM technology for a specific application allows for optimizing process selection for requirements.

6. Future perspectives

Despite all the benefits of the AFSD technique, research into it is still in its early stages. There is a significant gap between scientific research

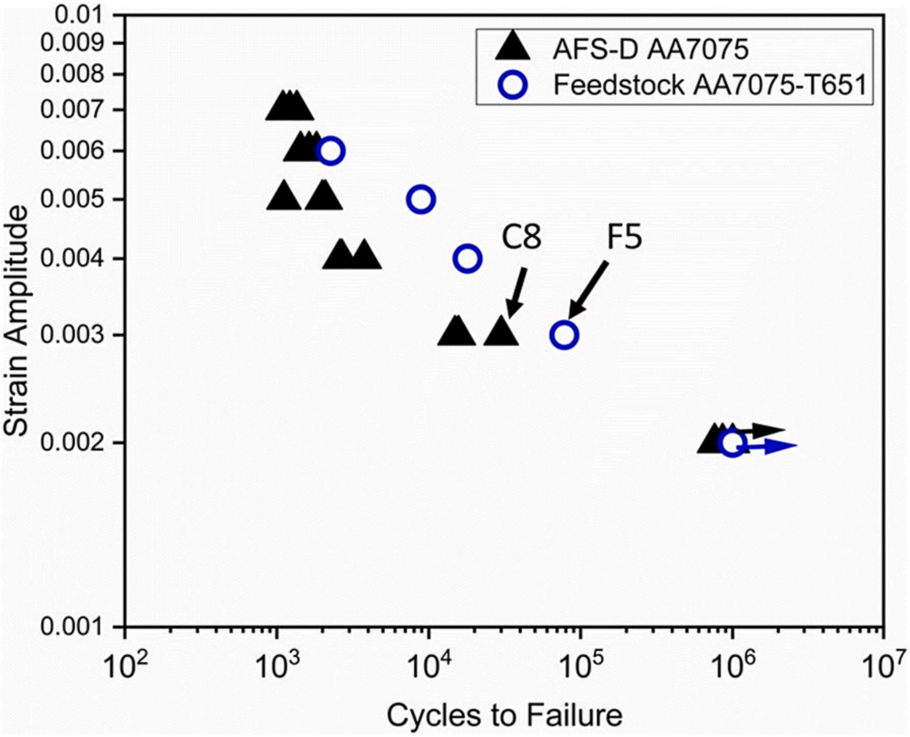

Fig. 56. Comparison of strain-life fatigue results for AFSDed and feedstock AA7075 [69].

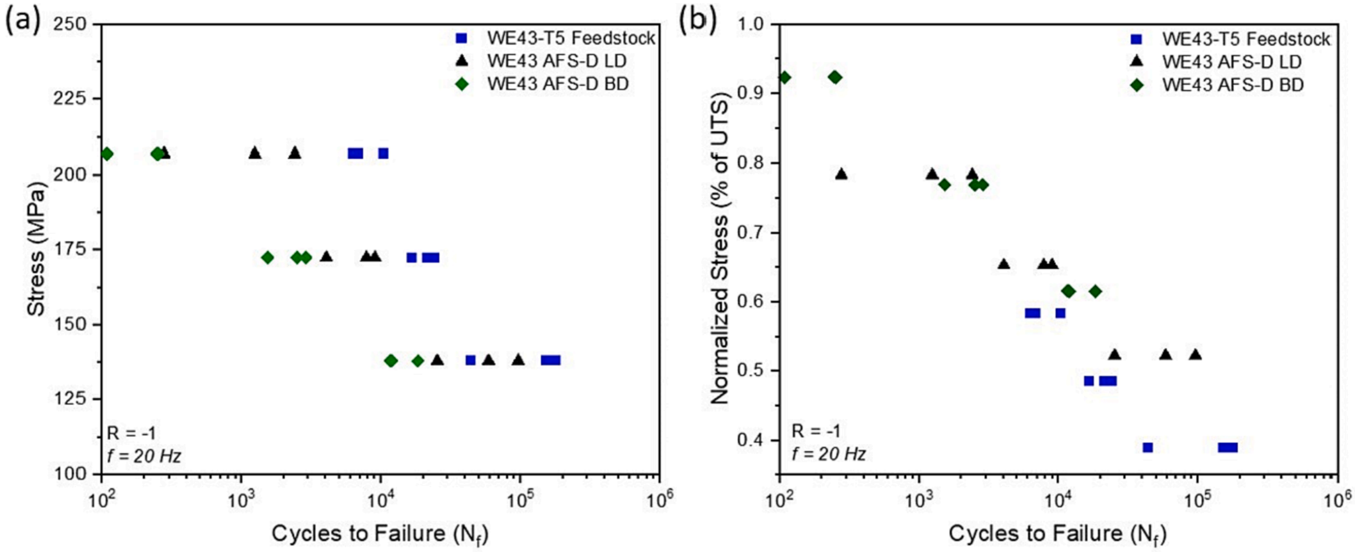

Fig. 57. (a) S-N plot and (b) S-N plot normalized by UTS for load-controlled fatigue tests of the bulk WE43 deposits along building direction, longitudinal direction, and WE43 T-5 feedstock samples at three stress levels [32].

and engineering practice, which necessitates the efforts of researchers and engineers from mechanics, physics, materials science and engineering, and other disciplines.

6.1. Defects

One of the main disadvantages of AFSD is the low spatial resolution, which includes low accuracy and surface finish due to the larger part size and increased building rate. While laser powder bed fusion can produce parts with feature sizes on the order of 10 µm, AFSD produces parts with feature sizes on the order of 1 mm or greater [17]. To quantify defects in large parts made by AFSD, neutron beam based testing can be performed. As opposed to X-ray beam, neutron beam can penetrate deep into most of high-Z materials and is a suitable choice for non-destructive evaluation of internal features of large objects. The High Flux Isotope Reactor (HFIR) at Oak Ridge National Lab (ORNL) is a reactor-based neutron source, which operates at 85 MW and provides a high-flux cold neutron beam from a liquid hydrogen moderator [118]. In order to capture small features inside metallic parts, the neutron imaging beamline has recently been enhanced with a Talbot-Lau interferometer similar to that developed at the Paul Scherrer Institute [119]. Some layer-by-layer structures of AFSDed components are detectable by neutron interferometry transmission imaging [120]. Two strategies are proposed to achieve the transition from near-net shape to true net shape:

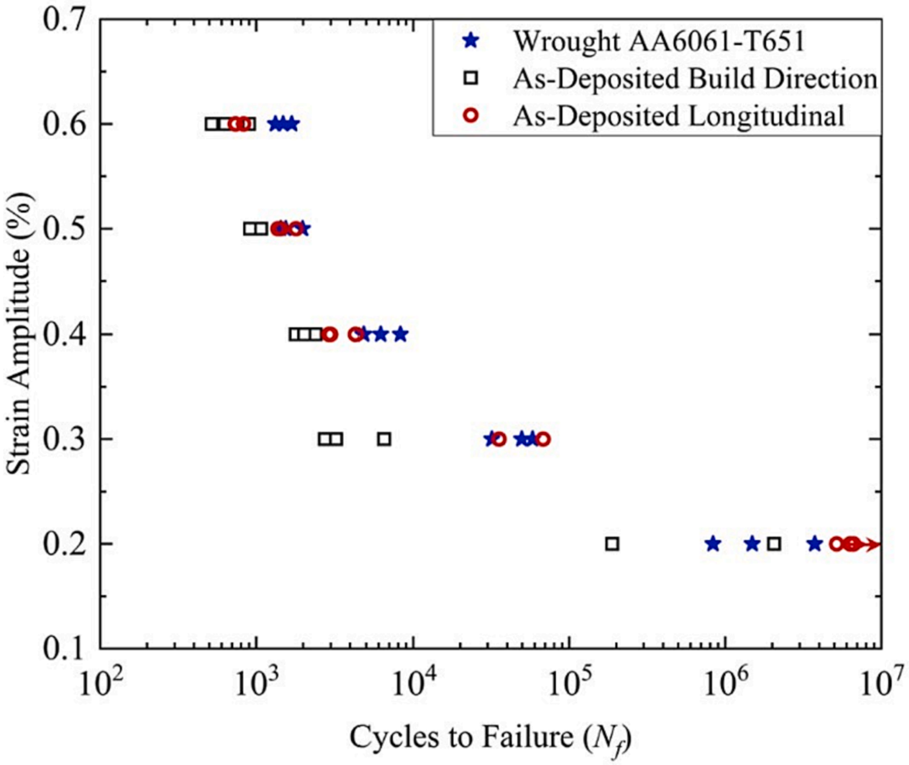

Fig. 58. Strain amplitude versus cycles to failure plot of AA6061-T651 feedstock, AA6061 deposit along the longitudinal direction, and AA6061 deposit along the building direction [90].

Table 6
Charpy impact results for WE43 deposit [87].

Condition	Rolled plate	Deposit 1	Deposit 2	Deposit 3
Impact energy/J	3.8 ± 0.5	3.8 ± 0.6	4.8 ± 0.2	4.5 ± 0.6

incorporating an additional subtractive process similar to that used in ultrasonic additive manufacturing, or scaling down the tool size and filler material [5].

For the first strategy, it is necessary to investigate the performance of samples in subsequent subtractive steps, such as structure evolution and property control. However, it is also difficult to develop equipment that combines additive and subtractive manufacturing on a single platform. For the second strategy, the “bigger” advantage of AFSD over other AM technologies is weakened, and the efficiency of the AFSD technique is reduced. Improving the resolution of as-deposited parts by investigating the relationship between processing conditions and accuracy is better suited to control the in-plane resolution of AFSDed components. In-situ process monitoring and control can further improve quality.

AFSD cannot manufacture complex geometries with overhangs due to the axial and shear forces applied to the feedstock material and substrate. Although, due to the solid-state nature of AFSD, there is less concern about material flowing off during AFSD compared to fusion-based AM techniques [17]. A component with a large overhang angle of 54° is successfully produced without support material, as shown in Fig. 61. Due to mechanical instability caused by the applied forces, there is still a limit for the maximum self-supporting overhang angle for AFSD. Buckling is another potential issue caused by mechanical instability when fabricating high-aspect-ratio components. The overhang angle limit and the aspect-ratio limit are important issues for future research.

6.2. *Microstructure control and property improvement*

Although the AFSD process is capable of producing components with fully-equiaxed microstructure, no fully-equiaxed crystal can be guaranteed. The proportion of equiaxed grains is strongly influenced by process variables. The relationship between process variables and microstructure evolution must be clarified in order to achieve full-equiaxed microstructure. In order to achieve homogeneous and high mechanical properties, sub-micron level structure characteristics such as precipitates, intermetallic particles, and even nano-level structure characteristics such as grain boundaries and dislocations must be carefully controlled. All of the aforementioned aspects of structure evolution in AFSD require further investigation. Furthermore, the evolution of structure across multiple length scales allows researchers to develop materials with improved properties.

Although the as-deposited parts have a refined, equiaxed microstructure, the mechanical properties of AFSDed samples are often inferior to heat-treated wrought alloys due to precipitate strengthening weakening. This phenomenon is particularly severe in aluminum alloys [121]. The dissolution of θ’ precipitates in AA2219 [72] or β and β’ precipitates in AA6061 [68] often results in lower tensile strength in AFSDed samples. The absence of strengthening precipitates causes softening in AFSDed components, particularly those made from consumable rods in optimal heat treated wrought condition. Some researchers believe that AFSD is best performed with hot-rolled or as-cast feedstock [33,77].

Although post-thermal processing can improve the properties, it is impractical to perform heat treatment on the large-scale components manufactured by AFSD. This is due to the lack of large-scale furnaces for heat treatment, which would be both expensive and energy intensive. Process strategy optimization to improve the as-made properties is

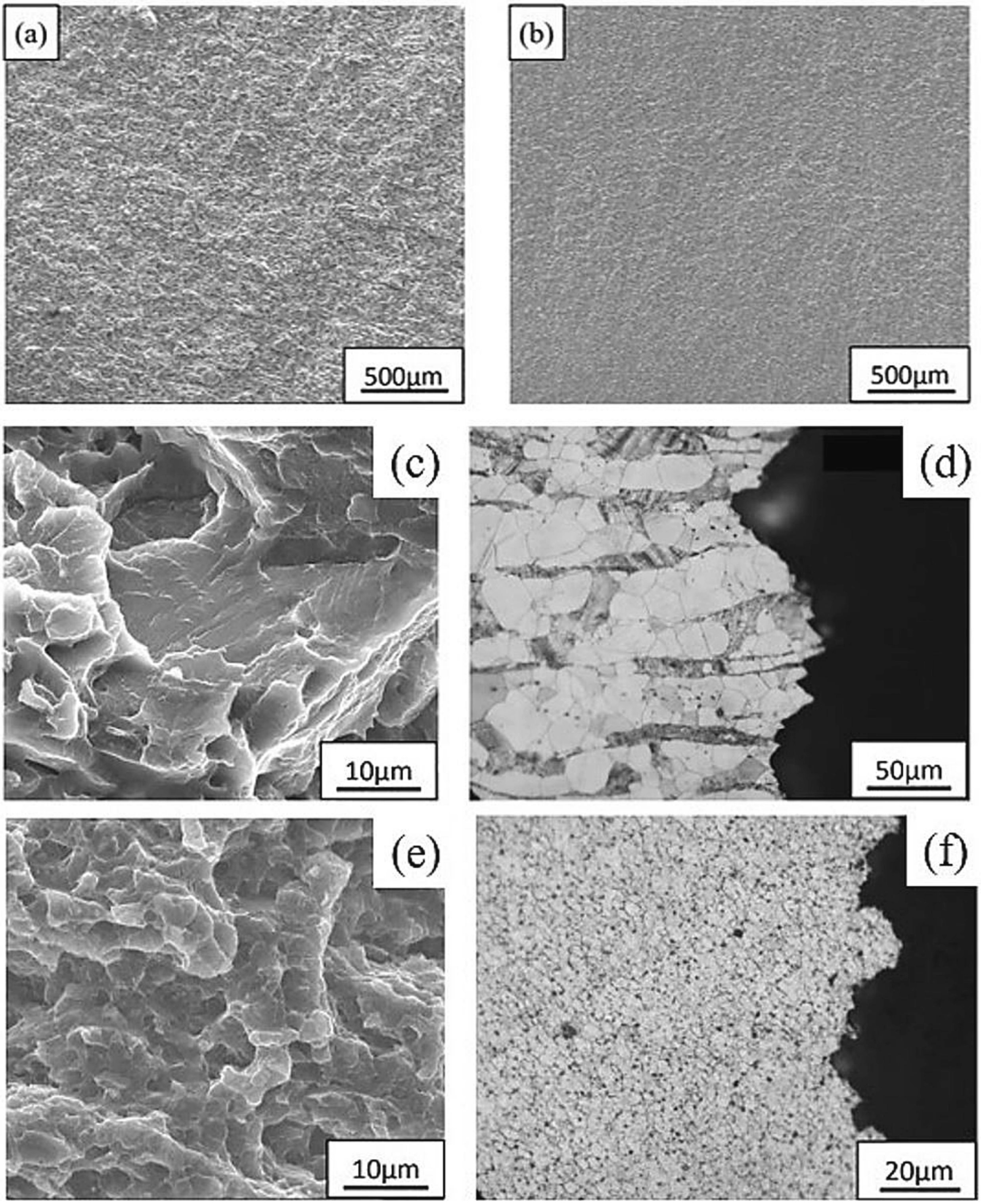

Fig. 59. Topography of the fracture surfaces of WE43 alloys (a) feedstock, (b) deposit. Higher magnification of the (c) fractograph and (d) fracture surface of the feedstock, as well as the (e) fractograph and (f) fracture surface of the deposit [87].

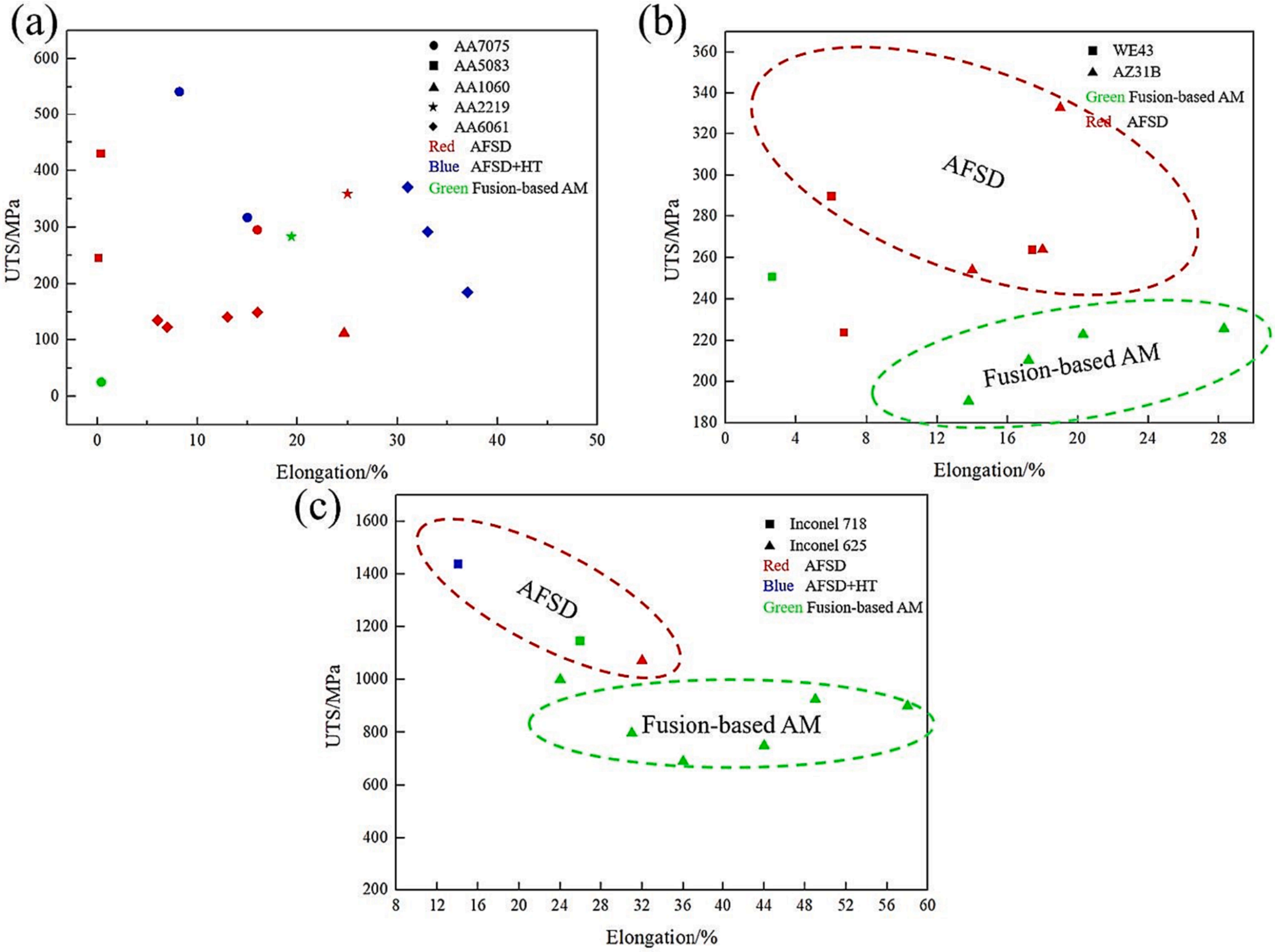

Fig. 60. Tensile strength versus elongation of (a) aluminum alloys [4,28,31,53,60,69,72,76,89,105–107], (b) magnesium alloys [28,32,108–110], and (c) nickel-based superalloys [10,33,70,111–117] in feedstock, AFSDed, and fusion-based AMed conditions.

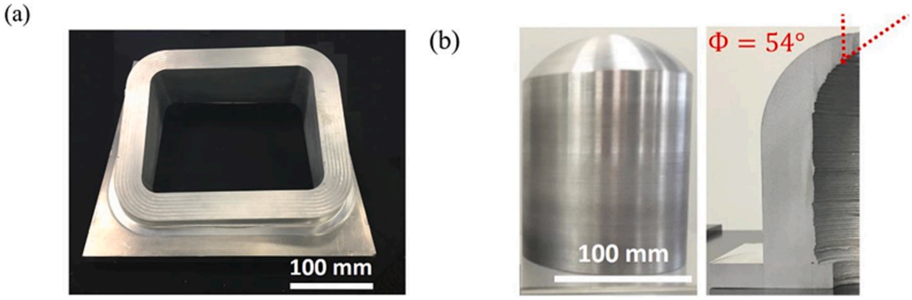

Fig. 61. Examples of manufactured parts. (a) A large AA 6061 window frame. (b) (Left) A large AA 6061 pressure vessel deposited in less than 2 h and machined to final surface finish and (Right) the internal structure of the pressure vessel showing an overhang angle as high as 54° [17].

critical, which necessitates a thorough understanding of the physics at work (detailed information can be found in Section 6.3). There are several strengthening mechanisms in metallic alloys, as described in Section 4. Different processes must be designed for alloys with different primary strengthening mechanisms. Aside from quasi-state, room temperature tensile mechanical properties, other properties and performances of as-deposited parts, such as fatigue behavior, impact properties, and creep properties at high temperatures, require further investigation. In addition, the corresponding standards and criteria are needed to be established.

6.3. *Integrated process-structure–property model with data-driven approaches*

Fundamentally, the "Processing-Structure-Property" relationship in AFSD technique must be established. It is critical to establish a quantitative understanding of the influences of processing parameters (such as tool rotation rate, transverse scanning speed, and feedstock feeding rate, layer thickness) and material physical properties on temperature evolution and material deformation. Furthermore, it is imperative to connect the thermal history and material flow process with structure evolution and property control. An integrated "Process-Structure-

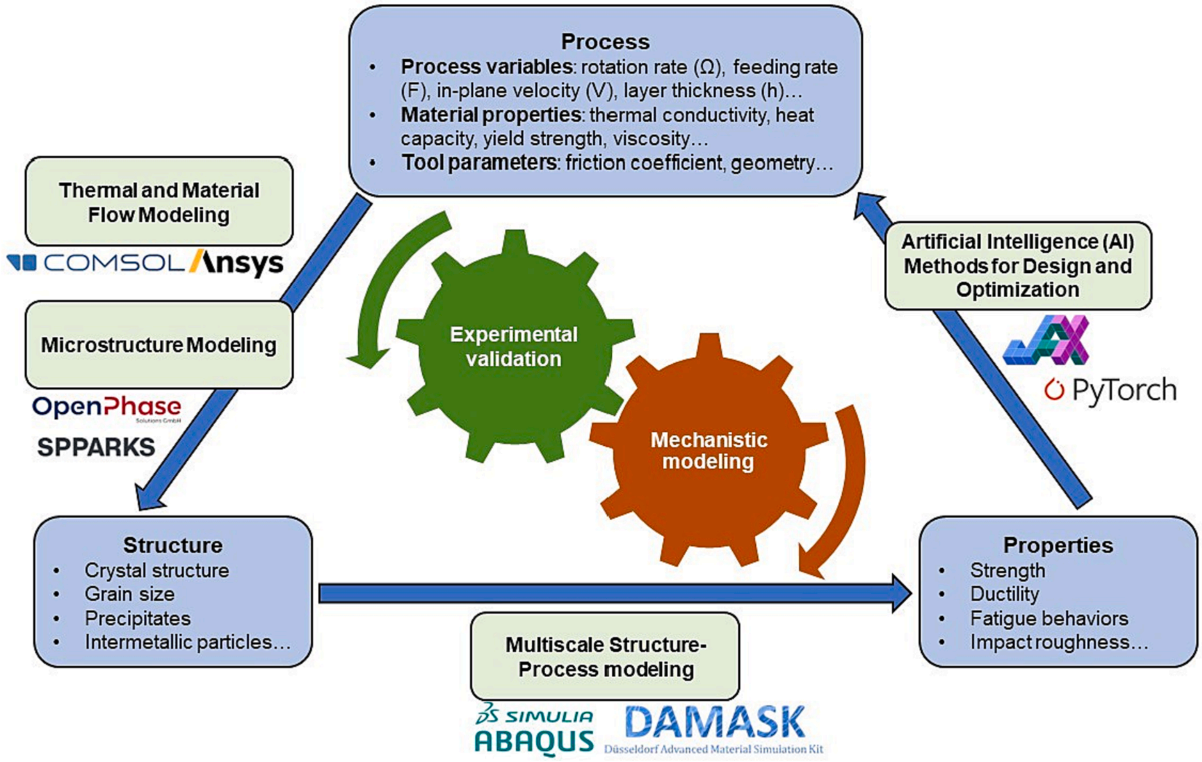

Fig. 62. Diagram illustrating the process-structure–property correlation, as well as their features, for parts manufactured using the AFSD technique. The role of various modeling methods and software in these research areas is illustrated.

Property" modeling framework for AFSD is proposed to achieve process parametric optimization with minimal experimental runs (Fig. 62).

Thermal modeling can clarify thermal conditions such as heat generation mechanisms, cooling rate, thermal gradient, and thermal cycles. Material flow behaviors such as plastic strain, strain rate, velocity field, and stress can also be captured using Computational Fluid Dynamics (CFD). Commercial CFD software such as COMSOL Multiphysics and Ansys Fluent can be used to simulate thermal and deformation evolution. The phase field method [122,123], Cellar Automaton [124,125] and the Monte Carlo method [126] can each be used to simulate microstructure evolution in AFSD. DAMASK [127] and ABAQUS subroutines based on crystal plasticity finite element (CPFE) approaches can be used to correlate structure with properties.

The integration of artificial intelligence methods is motivated by the critical need for modeling, prediction, and control of AFSD. Eren et al. [128] summarized the benefits of using artificial intelligence techniques to establish end-to-end predictions from process parameters (e.g., welding speed) to properties for friction stir welding (e.g., tensile strength). Interdisciplinary studies combining artificial intelligence or machine learning have become a rapidly developing field in recent years in the context of additive manufacturing [129–132]. Several user-friendly machine learning libraries, such as Google JAX and PyTorch, have been developed for general use. We believe that combining artificial intelligence (AI) methods for modeling and design (both traditional and modern deep learning based) with AFSD can be a viable and promising future research direction. Han et al. [133], for example, proposed a dimension reduction method combined with a regeneration neural network for quantitative microstructure analysis in AFSD. A review paper [134] on AI methods in advanced manufacturing is provided for interested readers.

6.4. *Repair and re-manufacturing*

Aside from manufacturing, AFSD can be used for repair [135], re-manufacturing, and cladding [51]. AFSD technique has the potential to repair a variety of geometries including surface layering or shallow divot repair (Fig. 63(a)), volumetric fill of deep features (Fig. 63(b)), feature reconstruction (Fig. 63(c)), and crack (Fig. 63(d)) [136]. Due to its solid-state nature, AFSD can repair both weldable and non-weldable materials, unlike fusion based AM technologies. Furthermore, due to the friction stirring effect, sufficient material mixing and strong interfacial bonding can be achieved. Oxides, surface dirt, and corroded materials can be removed by friction. A fine, equiaxed microstructure with breakup of potential brittle intermetallic phases can be obtained at the microscopic level.

Despite these benefits, the use of AFSD in repair is still in the early stage. Several studies have been conducted to demonstrate these possibilities [135,136]. AFSD has been successfully applied to the repair of holes and grooves in AA7075 [99,135]. With sufficient material mixing, there is no discernible interface or defect between the substrate plate and the repaired deposition. Notably, underwater repair by AFSD is another recent topic of study. Finally, potential future research direction is related to the AFSD tool. Researchers have long been concerned about the abrasion of hollow tools. New tool materials with improved wear resistance must be developed specifically for AFSD.

7. Conclusions

AFSD is free of the thorny crack and pore defects that plague fusion-based AM due to its solid-state nature. Furthermore, AFSD provides a method for producing full-equiaxed microstructure. The ability to control and innovate the microstructure across multiple length scales, from

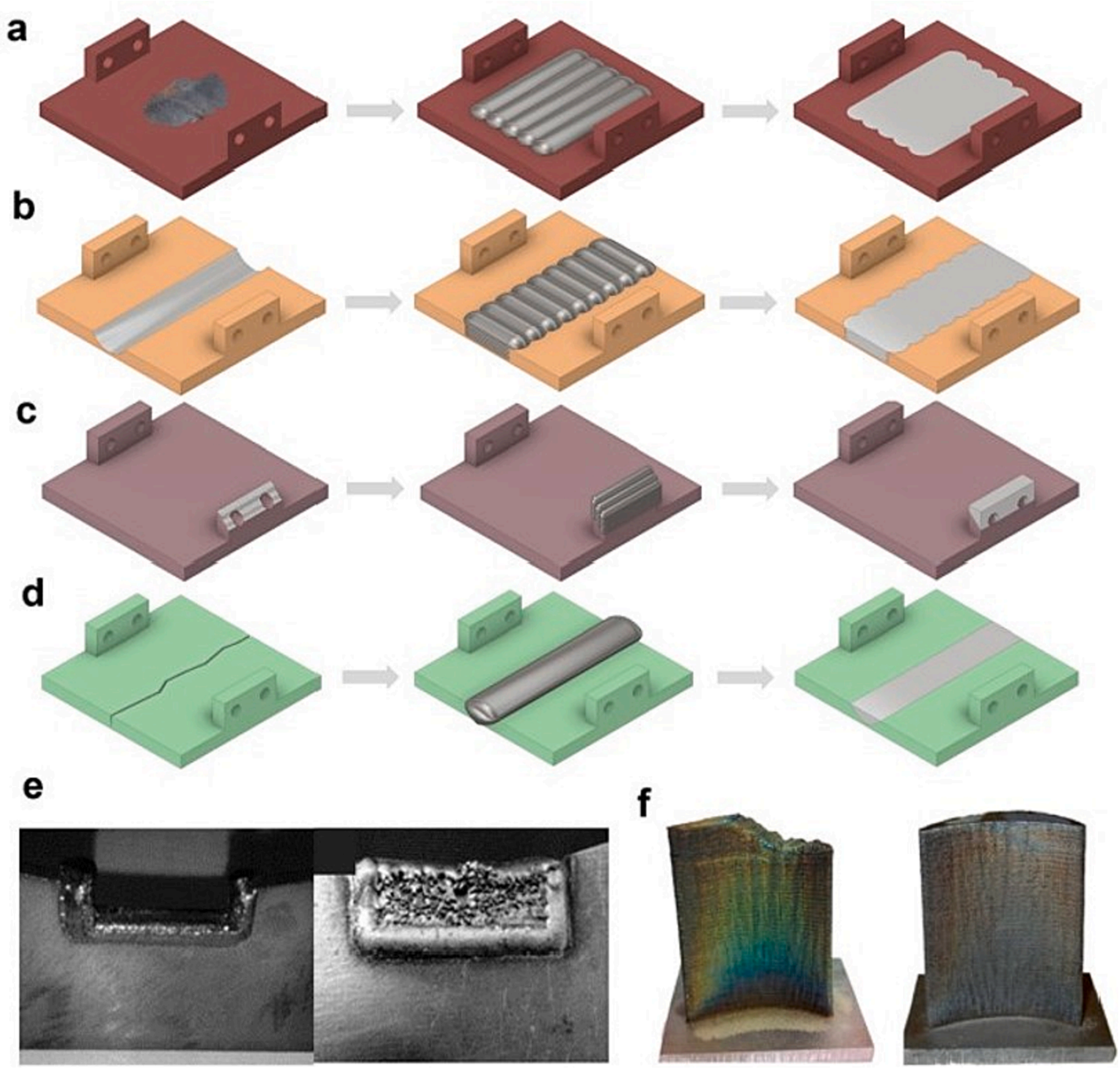

Fig. 63. Repaired geometries using fusion-based techniques. Schematic diagrams of (left) original damage, (center) immediately following repair, and (right) surface after final grinding for four types of repairs: (a) surface layering or shallow divot repair, (b) volumetric fill, (c) feature reconstruction, and (d) crack repair [136]. Examples of (e) volumetric fill repair [137], and (f) feature reconstruction [138] are repaired by laser metal deposition.

micron (~ μm) crystal growth to nanometer (~ nm) precipitate evolution, is also enabled by the severe plastic deformation. Due to the wrought-like microstructure, the mechanical properties of the deposited parts are comparable to wrought alloys or even better for alloys like superalloys. AFSD is also known for increased building rate and large building size, which renders AFSD ideal for large-scale applications in the aerospace, aviation, automation, and energy industries. This paper also discusses its potential uses in repair, re-manufacturing, and cladding.

Despite its enormous potential, AFSD is still in its early stages, and many issues must be resolved before being applied in production. Limitations include reduced spatial resolution and geometrical complexity. Flash, weak material bonding, local melting, and oxidation are challenging defects. Furthermore, a sub-optimal microstructure, such as unfavorable precipitates in aluminum alloys and increased texture intensity, results in decreased strength and increased anisotropy of mechanical properties. The physics underlying deformation behaviors, heat generation, temperature history, and the corresponding microstructure evolution and property responses all need to be clarified in order to broaden the industrial application of AFSD. A data-driven approach combined with an integrated process-structure–property model is a promising solution.

Declaration of Competing Interest

The authors declare that they have no known competing financial interests or personal relationships that could have appeared to influence the work reported in this paper.

Data availability

No data was used for the research described in the article.

Acknowledgement

SG is supported by the U.S. National Science Foundation under grant number OIA1946231 and the Louisiana Board of Regents for the Louisiana Materials Design Alliance (LAMDA).

References

[1] T. DebRoy, H.L. Wei, J.S. Zuback, T. Mukherjee, J.W. Elmer, J.O. Milewski, A. M. Beese, A. Wilson-Heid, A. De, W. Zhang, Additive manufacturing of metallic components - process, structure and properties, Prog. Mater Sci. 92 (2018) 112–224.

[2] K. Kempen, L. Thijs, B. Vrancken, S. Buls, J. P. Kruth, Producing crack-free, high density M2 HSS parts by selective laser melting: Pre-heating the baseplate, utwired.engr.utexas.edu (2013).

[3] L. N. Carter, M. M. Attallah, R. C. Reed, Laser Powder Bed Fabrication of Nickel-Base Superalloys: Influence of Parameters; Characterisation, Quantification and Mitigation of Cracking, Superalloys 2012, 2012.

[4] J.H. Martin, B.D. Yahata, J.M. Hundley, J.A. Mayer, T.A. Schaedler, T.M. Pollock, 3d printing of high-strength aluminium alloys, Nature 549 (2017) 365.

[5] R.J. Griffiths, M.E.J. Perry, J.M. Sietins, Y.H. Zhu, N. Hardwick, C.D. Cox, H. A. Rauch, H.Z. Yu, A perspective on solid-state additive manufacturing of aluminum matrix composites using MELD, J. Mater. Eng. Perform. 28 (2019) 648–656.

[6] J. P. Schultz, K. D. Creehan, US8636194 b2, 2014.

[7] J. P. Schultz, K. D. Creehan, US20160107262, 2016.

[8] D. Wang, S. Wu, F. Fu, S. Mai, Y. Yang, Y. Liu, C. Song, Mechanisms and characteristics of spatter generation in slm processing and its effect on the properties, Mater. Des. 117 (2017) 121–130.

[9] J.Y. Son, H.S. Yoon, K.Y. Lee, S.H. Park, D.S. Shim, Investigation into high-temperature interfacial strength of heat-resisting alloy deposited by laser melting process, Met. Mater. Int. 26 (2020) 384–394.

[10] H.Y. Gao, H.J. Li, Friction additive manufacturing technology: A state-of-the-art survey, Adv. Mech. Eng. 13 (2021).

[11] A.K. Srivastava, N. Kumar, A.R. Dixit, Friction stir additive manufacturing - an innovative tool to enhance mechanical and microstructural properties, Mater. Sci. Eng. B-Adv. Funct. Solid-State Mater. 263 (2021).

[12] H.Z. Yu, R.S. Mishra, Additive friction stir deposition: a deformation processing route to metal additive manufacturing, Mater. Res. Lett. 9 (2021) 71–83.

[13] V. Gopan, L.D.K. Wins, A. Surendran, Innovative potential of additive friction stir deposition among current laser based metal additive manufacturing processes: A review, CIRP J. Manuf. Sci. Technol. 32 (2021) 228–248.

[14] A. Mukhopadhyay, P. Saha, A critical review on process metrics-microstructural evolution-process performance correlation in additive friction stir deposition (AFS-D), J. Braz. Soc. Mech. Sci. Eng. 44 (2022).

[15] H. Venkit, S. K. Selvaraj, Review on latest trends in friction-based additive manufacturing techniques, Proceedings of the Institution of Mechanical Engineers Part C – Journal of Mechanical Engineering Science 236 (2022) 10090–10121.

[16] D.A.P. Prabhakar, A.K. Shettigar, M.A. Herbert, G.C.M. Patel, D.Y. Pimenov, K. Giasin, C. Prakash, A comprehensive review of friction stir techniques in structural materials and alloys: challenges and trends, J. Mater. Re. Technol. - JMR&T 20 (2022) 3025–3060.

[17] H.Z. Yu, M.E. Jones, G.W. Brady, R.J. Griffiths, D. Garcia, H.A. Rauch, C.D. Cox, N. Hardwick, Non-beam-based metal additive manufacturing enabled by additive friction stir deposition, Scr. Mater. 153 (2018) 122–130.

[18] Meld brochure — Aeroprobe corporation, 2018.

[19] S. Palanivel, R.S. Mishra, Building without melting: a short review of friction-based additive manufacturing techniques, Internat. J. Add. Sub. Mater. Manuf. 1 (2017) 82.

[20] N. Gotawala, N.K. Mishra, A. Shrivastava, Solid-state depositions of multilayer SS304 by friction stir metal deposition, Mater. Lett. 314 (2022).

[21] J.J.S. Dilip, G.D.J. Ram, B.E. Stucker, Additive manufacturing with friction welding and friction deposition processes, Int. J. Rapid Manuf. 3 (2012) 56–69.

[22] M. Seleman, S. Ataya, M.M.Z. Ahmed, A.M.M. Hassan, F.H. Latief, K. Hajlaoui, A. E. El-Nikhaily, M.I.A. Habba, The additive manufacturing of aluminum matrix nano Al2O3 composites produced via friction stir deposition using different initial material conditions, Materials 15 (2022).

[23] R.S. Mishra, Z.Y. Ma, Friction stir welding and processing, Mater. Sci. Eng. R-Rep. 50 (2005) 1–78.

[24] S. Palanivel, P. Nelaturu, B. Glass, R.S. Mishra, Friction stir additive manufacturing for high structural performance through microstructural control in an Mg based WE43 alloy, Mater. Des. 65 (2015) 934–952.

[25] H.A. Derazkola, F. Khodabakhshi, A.P. Gerlich, Friction-forging tubular additive manufacturing (fftam): A new route of solid-state layer-upon-layer metal deposition, J. Mater. Res. Technol. - JMR&T 9 (2020) 15273–15285.

[26] J.J.S. Dilip, G.D.J. Ram, Microstructure evolution in aluminum alloy AA 2014 during multi-layer friction deposition, Mater Charact 86 (2013) 146–151.

[27] P. Agrawal, R.S. Haridas, S. Yadav, S. Thapliyal, S. Gaddam, R. Verma, R. S. Mishra, Processing-structure-property correlation in additive friction stir deposited Ti-6Al-4V alloy from recycled metal chips, Addit. Manuf. 47 (2021).

[28] K. Kandasamy, L.E. Renaghan, J.R. Calvert, K.D. Creehan, J.P. Schultz, Solid-state additive manufacturing of aluminum and magnesium alloys, Mater. Sci. Technol. (2013) 59–69.

[29] R.J. Griffiths, D. Garcia, J. Song, V.K. Vasudevan, H.Z. Yu, Solid-state additive manufacturing of aluminum and copper using additive friction stir deposition: Process-microstructure linkages, Materialia 15 (2021), 100967.

[30] E. Elfishawy, M. M. Z. Ahmed, M. Seleman, M. Minerals, S. Mat, Additive manufacturing of aluminum using friction stir deposition, in: Nanoscience and Nanotechnology in Advanced Composites Symposium held at TMS 149th Annual Meeting and Exhibition, Minerals Metals & Materials Series, 2020, pp. 227–238. URL: <GotoISI>://WOS:000674707900021. doi:10.1007/978-3-030-36296-6_21.

[31] J.K. Yoder, R.J. Griffiths, H.Z. Yu, Deformation-based additive manufacturing of 7075 aluminum with wrought-like mechanical properties, Mater. Des. 198 (2021).

[32] M.B. Williams, T.W. Robinson, C.J. Williamson, R.P. Kinser, N.A. Ashmore, P. G. Allison, J.B. Jordon, Elucidating the effect of additive friction stir deposition on the resulting microstructure and mechanical properties of magnesium alloy WE43, Metals 11 (2021).

[33] J.J.S. Dilip, G.D.J. Ram, Friction freeform fabrication of superalloy Inconel 718: Prospects and problems, Metallurgical and Materials Transactions B-Process Metallurgy and Materials Processing, Science 45 (2014) 182–192.

[34] J.L. Priedeman, B.J. Phillips, J.J. Lopez, B.E.T. Roper, B.C. Hornbuckle, K. A. Darling, J.B. Jordon, P.G. Allison, G.B. Thompson, Microstructure development in additive friction stir-deposited Cu, Metals 10 (2020).

[35] J.J.S. Dilip, S. Babu, S.V. Rajan, K.H. Rafi, G.D.J. Ram, B.E. Stucker, Use of friction surfacing for additive manufacturing, Mater. Manuf. Process. 28 (2013) 189–194.

[36] H.S. Park, T. Kimura, T. Murakami, Y. Nagano, K. Nakata, M. Ushio, Microstructures and mechanical properties of friction stir welds of 60%Cu-40%Zn copper alloy, Mater. Sci. Eng. A-Struct. Mater. Propert. Microstruct. Process. 371 (2004) 160–169.

[37] R. Nandan, T. DebRoy, H. Bhadeshia, Recent advances in friction-stir welding - process, weldment structure and properties, Prog. Mater Sci. 53 (2008) 980–1023.

[38] M. Perry, H.A. Rauch, R.J. Griffiths, D. Garcia, H.Z. Yu, Tracing plastic deformation path and concurrent grain refinement during additive friction stir deposition, Materialia 18 (2021), 101159.

[39] P. Colegrove 3 dimensional flow and thermal modelling of the friction stir welding process, Thesis University of Adelaide 2001 https://hdl.handle.net/2440/122087.

[40] S. Rathee, M. Srivastava, P.M. Pandey, A. Mahawar, S. Shukla, Metal additive manufacturing using friction stir engineering: A review on microstructural evolution, tooling and design strategies, CIRP J. Manuf. Sci. Technol. 35 (2021) 560–588.

[41] R.S. Mishra, R.S. Haridas, P. Agrawal, Friction stir-based additive manufacturing, Sci. Technol. Weld. Join. 27 (2022) 141–165.
[42] R. Nandan, G.G. Roy, T.J. Lienert, T. Debroy, Three-dimensional heat and material flow during friction stir welding of mild steel, Acta Mater. 55 (2007) 883–895.
[43] D. Garcia, W.D. Hartley, H.A. Rauch, R.J. Griffiths, R.X. Wang, Z.Y.J. Kong, Y. H. Zhu, H.Z. Yu, In situ investigation into temperature evolution and heat generation during additive friction stir deposition: A comparative study of Cu and Al-Mg-Si, Addit. Manuf. 34 (2020).
[44] F.C. Liu, Y. Hovanski, M.P. Miles, C.D. Sorensen, T.W. Nelson, A review of friction stir welding of steels: Tool, material flow, microstructure, and properties, J. Mater. Sci. Technol. 34 (2018) 39–57.
[45] G.G. Stubblefield, K. Fraser, B.J. Phillips, J.B. Jordon, P.G. Allison, A meshfree computational framework for the numerical simulation of the solid-state additive manufacturing process, additive friction stir-deposition (AFS-D), Mater. Des. 202 (2021).
[46] S. Liu, T.C. Bor, A.A. Van der Stelt, H.J.M. Geijselaers, C. Kwakernaak, A. M. Kooijman, J.M.C. Mol, R. Akkerman, A.H. van den Boogaard, Friction surface cladding: An exploratory study of a new solid state cladding process, J. Mater. Process. Technol. 229 (2016) 769–784.
[47] H.G. Yang, Numerical simulation of the temperature and stress state on the additive friction stir with the smoothed particle hydrodynamics method, Strength Mater. 52 (2020) 24–31.
[48] A.P. Reynolds, Flow visualization and simulation in FSW, Scr. Mater. 58 (2008) 338–342.
[49] X.C. He, F.S. Gu, A. Ball, A review of numerical analysis of friction stir welding, Prog. Mater Sci. 65 (2014) 1–66.
[50] C.J.T. Mason, R.I. Rodriguez, D.Z. Avery, B.J. Phillips, B.P. Bernarding, M. B. Williams, S.D. Cobbs, J.B. Jordon, P.G. Allison, Process-structure-property relations for as-deposited solid-state additively manufactured high-strength aluminum alloy, Addit. Manuf. 40 (2021).
[51] W.D. Hartley, D. Garcia, J.K. Yoder, E. Poczatek, J.H. Forsmark, S.G. Luckey, D. A. Dillard, H.Z. Yu, Solid-state cladding on thin automotive sheet metals enabled by additive friction stir deposition, J. Mater. Process. Technol. 291 (2021).
[52] M.E.J. Perry, R.J. Griffiths, D. Garcia, J.M. Sietins, Y.H. Zhu, H.Z. Yu, Morphological and microstructural investigation of the non-planar interface formed in solid-state metal additive manufacturing by additive friction stir deposition, Addit. Manuf. 35 (2020).
[53] B.J. Phillips, C.J. Williamson, R.P. Kinser, J.B. Jordon, K.J. Doherty, P.G. Allison, Microstructural and mechanical characterization of additive friction stir-deposition of aluminum alloy 5083 effect of lubrication on material anisotropy, Materials 14 (2021).
[54] Z.T. Gan, Y.P. Lian, S.E. Lin, K.K. Jones, W.K. Liu, G.J. Wagner, Benchmark study of thermal behavior, surface topography, and dendritic microstructure in selective laser melting of Inconel 625, Integrating Materials and Manufacturing, Innovation 8 (2019) 178–193.
[55] AM-bench 2018-test-data, 2018. doi:https://www.nist.gov/ambench/benchmark-test-data/.
[56] X. Cao, M. Jahazi, Effect of welding speed on butt joint quality of Ti-6Al-4V alloy welded using a high-power Nd:YAG laser, Opt. Lasers Eng. 47 (2009) 1231–1241.
[57] M. Vaezi, P. Drescher, H. Seitz, Beamless metal additive manufacturing, Materials 13 (2020).
[58] B.V. Kumar, G.M. Reddy, T. Mohandas, Identification of suitable process parameters for friction surfacing of mild steel with AA6063 aluminium alloy, Int. J. Adv. Manuf. Technol. 74 (2014) 433–443.
[59] B.J. Phillips, C.J.T. Mason, S.C. Beck, D.Z. Avery, K.J. Doherty, P.G. Allison, J. B. Jordon, Effect of parallel deposition path and interface material flow on resulting microstructure and tensile behavior of Al-Mg-Si alloy fabricated by additive friction stir deposition, J. Mater. Process. Technol. 295 (2021).
[60] A. Mukhopadhyay, P. Saha, Mechanical and microstructural characterization of aluminium powder deposit made by friction stir based additive manufacturing, J. Mater. Process. Technol. 281 (2020).
[61] J. Humphreys M. Hatherly . second, Recrystallization and Related Annealing Phenomena 2004 Elsevier Oxford 10.1016/B978-008044164-1/50023-2.
[62] W. Blum, Q. Zhu, R. Merkel, H. J. McQueen, Geometric dynamic recrystallization in hot torsion of al-smg-0.6mn (AA5083), Materials Science and Engineering A-Structural Materials Properties Microstructure and Processing 205 (1996) 23–30.
[63] T. Sakai, A. Belyakov, R. Kaibyshev, H. Miura, J.J. Jonas, Dynamic and post-dynamic recrystallization under hot, cold and severe plastic deformation conditions, Prog. Mater Sci. 60 (2014) 130–207.
[64] K. Huang, R.E. Loge, A review of dynamic recrystallization phenomena in metallic materials, Mater. Des. 111 (2016) 548–574.
[65] M. Muzyk, Z. Pakiela, K.J. Kurzydlowski, Generalized stacking fault energies of aluminum alloys - density functional theory calculations, Metals 8 (2018).
[66] Y.H. Zhao, X.Z. Liao, Y.T. Zhu, Z. Horita, T.G. Langdon, Influence of stacking fault energy on nanostructure formation under high pressure torsion, Mater. Sci. Eng. A-Struct. Mater. Propert. Microstruct. Process. 410 (2005) 188–193.
[67] G.R. Canova, U.F. Kocks, J.J. Jonas, Theory of torsion texture development, Acta Metall. 32 (1984) 211–226.
[68] B.J. Phillips, D.Z. Avery, T. Liu, O.L. Rodriguez, P.G. Allison, Microstructure-deformation relationship of additive friction stir-deposition Al-Mg-Si, Materialia 7 (2019), 100387.
[69] D.Z. Avery, B.J. Phillips, C.J.T. Mason, M. Palermo, M.B. Williams, C. Cleek, O. L. Rodriguez, P.G. Allison, J.B. Jordon, Influence of grain refinement and microstructure on fatigue behavior for solid-state additively manufactured Al-Zn-Mg-Cu alloy, Metallurgical and Materials Transactions a-Physical Metallurgy and Materials, Science 51 (2020) 2778–2795.
[70] O.G. Rivera, P.G. Allison, J.B. Jordon, O.L. Rodriguez, L.N. Brewer, Z. McClelland, W.R. Whittington, D. Francis, J. Su, R.L. Martens, N. Hardwick, Microstructures and mechanical behavior of Inconel 625 fabricated by solid-state additive manufacturing, Mater. Sci. Eng. A-Struct. Mater. Propert. Microstruct. Process. 694 (2017) 1–9.
[71] C.Y. Zeng, H. Ghadimi, H. Ding, S. Nemati, A. Garbie, J. Raush, S.M. Guo, Microstructure evolution of Al6061 alloy made by additive friction stir deposition, Materials 15 (2022).
[72] O.G. Rivera, P.G. Allison, L.N. Brewer, O.L. Rodriguez, J.B. Jordon, T. Liu, W. R. Whittington, R.L. Martens, Z. McClelland, C.J.T. Mason, L. Garcia, J.Q. Su, N. Hardwick, Influence of texture and grain refinement on the mechanical behavior of AA2219 fabricated by high shear solid state material deposition, Mater. Sci. Eng. A-Struct. Mater. Propert. Microstruct. Process. 724 (2018) 547–558.
[73] M.R. Rokni, A. Zarei-Hanzaki, H.R. Abedi, Microstructure evolution and mechanical properties of back extruded 7075 aluminum alloy at elevated temperatures, Mater. Sci. Eng. A-Struct. Mater. Propert. Microstruct. Process. 532 (2012) 593–600.
[74] A. Simar, Y. Brechet, B. de Meester, A. Denquin, C. Gallais, T. Pardoen, Integrated modeling of friction stir welding of 6xxx series Al alloys: Process, microstructure and properties, Prog. Mater Sci. 57 (2012) 95–183.
[75] M. Murayama, K. Hono, Pre-precipitate clusters and precipitation processes in Al-Mg-Si alloys, Acta Mater. 47 (1999) 1537–1548.
[76] S.C. Beck, B.A. Rutherford, D.Z. Avery, B.J. Phillips, H. Rao, M.Y. Rekha, L. N. Brewer, P.G. Allison, J.B. Jordon, The effect of solutionizing and artificial aging on the microstructure and mechanical properties in solid-state additive manufacturing of precipitation hardened Al-Mg-Si alloy, Mater. Sci. Eng. A-Struct. Mater. Propert. Microstruct. Process. 819 (2021).
[77] B. Alzahrani, M. Seleman, M.M.Z. Ahmed, E. Elfishawy, A.M.Z. Ahmed, K. Touileb, N. Jouini, M.I.A. Habba, The applicability of die cast A356 alloy to additive friction stir deposition at various feeding speeds, Materials 14 (2021).
[78] D.H. Choi, Y.H. Kim, B.W. Ahn, Y.I. Kim, S.B. Jung, Microstructure and mechanical property of A356 based composite by friction stir processing, Trans. Nonferrous Met. Soc. Chin. 23 (2013) 335–340.
[79] J.K. Mackenzie, 2nd paper on statistics associated with the random disorientation of cubes, Biometrika 45 (1958) 229–240.
[80] J.K. Mason, C.A. Schuh, The generalized Mackenzie distribution: Disorientation angle distributions for arbitrary textures, Acta Mater. 57 (2009) 4186–4197.
[81] F. Montheillet, M. Cohen, J.J. Jonas, Axial stresses and texture development during the torsion testing of Al, Cu and alpha-Fe, Acta Metall. 32 (1984) 2077–2089.
[82] F. Barlat, O. Richmond, Prediction of tricomponent plane-stress yield surfaces and associated flow and failure behavior of strongly textured fcc polycrystalline sheets, Mater. Sci. Eng. 95 (1987) 15–29.
[83] W. Yuan, R.S. Mishra, Grain size and texture effects on deformation behavior of AZ31 magnesium alloy, Mater. Sci. Eng. A-Struct. Mater. Propert. Microstruct. Process. 558 (2012) 716–724.
[84] A.M. Jamili, A. Zarei-Hanzaki, H.R. Abedi, P. Minarik, R. Soltani, The microstructure, texture, and room temperature mechanical properties of friction stir processed Mg-Y-Nd alloy, Mater. Sci. Eng. A-Struct. Mater. Propert. Microstruct. Process. 690 (2017) 244–253.
[85] H.L. Wei, J.W. Elmer, T. DebRoy, Origin of grain orientation during solidification of an aluminum alloy, Acta Mater. 115 (2016) 123–131.
[86] H.L. Wei, J.W. Elmer, T. DebRoy, Three-dimensional modeling of grain structure evolution during welding of an aluminum alloy, Acta Mater. 126 (2017) 413–425.
[87] J.R. Calvert, Microstructure and Mechanical Properties of WE43 Alloy Produced Via Additive Friction Stir Technology, Virginia Polytechnic Institute and State University, Thesis, 2015.
[88] H.A. Derazkola, F. Khodabakhshi, A.P. Gerlich, Fabrication of a nanostructured high strength steel tube by friction-forging tubular additive manufacturing (FFTAM) technology, J. Manuf. Process. 58 (2020) 724–735.
[89] J.B. Jordon, P.G. Allison, B.J. Phillips, D.Z. Avery, R.P. Kinser, L.N. Brewer, C. Cox, K. Doherty, Direct recycling of machine chips through a novel solid-state additive manufacturing process, Mater. Des. 193 (2020).
[90] B. Rutherford, D.Z. Avery, B.J. Phillips, H.M. Rao, K.J. Doherty, P.G. Allison, L. N. Brewer, J.B. Jordon, Effect of thermomechanical processing on fatigue behavior in solid-state additive manufacturing of Al-Mg-Si alloy, Metals 10 (2020).
[91] H. Ghadimi, H. Ding, S. Emanet, M. Talachian, C. Cox, M. Eller, S. Guo, Hardness distribution of Al2050 parts fabricated using additive friction stir deposition, Materials 16 (2023).
[92] F.R.N. Nabarro, Fifty-year study of the Peierls-Nabarro stress, Mater. Sci. Eng. A-Struct. Mater. Propert. Microstruct. Process. 234 (1997) 67–76.
[93] O. Ryen, O. Nijs, E. Sjolander, B. Holmedal, H.E. Ekstrom, E. Nes, Strengthening mechanisms in solid solution aluminum alloys, Metallurgical and Materials Transactions a-Physical Metallurgy and Materials, Science 37A (2006) 1999–2006.
[94] R.D. Doherty, D.A. Hughes, F.J. Humphreys, J.J. Jonas, D.J. Jensen, M.E. Kassner, W.E. King, T.R. McNelley, H.J. McQueen, A.D. Rollett, Current issues in recrystallization: a review, Mater. Sci. Eng. A-Struct. Mater. Propert. Microstruct. Process. 238 (1997) 219–274.
[95] N. Hansen, Hall-Petch relation and boundary strengthening, Scr. Mater. 51 (2004) 801–806.

[96] M.E. Fine, Precipitation hardening of aluminum-alloys, Metall. Trans. A 6 (1975) 625–630.

[97] U.F. Kocks, C. Tome, W. h. r.,, Texture and Anisoropy: Preferred Orientations in Polycrystals and their Effect on Materials Properties, Cambridge University Press, 1998.

[98] D.L. McDowell, K. Gall, M.F. Horstemeyer, J. Fan, Microstructure-based fatigue modeling of cast A356–T6 alloy, Eng. Fract. Mech. 70 (2003) 49–80.

[99] D.Z. Avery, C.E. Cleek, B.J. Phillips, M.Y. Rekha, R.P. Kinser, H.M. Rao, L. N. Brewer, P.G. Allison, J.B. Jordon, Evaluation of microstructure and mechanical properties of Al-Zn-Mg-Cu alloy repaired via additive friction stir deposition, J. Eng. Mater. Technol. 144 (2022).

[100] N. Zhu, D.Z. Avery, B.A. Rutherford, B.J. Phillips, P.G. Allison, J.B. Jordon, L. N. Brewer, The effect of anodization on the mechanical properties of AA6061 produced by additive friction stir deposition, Metals 11 (2021).

[101] S.J. Wolff, Z.T. Gan, S. Lin, J.L. Bennett, W.T. Yan, G. Hyatt, K.F. Ehmann, G. J. Wagner, W.K. Liu, J. Cao, Experimentally validated predictions of thermal history and microhardness in laser-deposited Inconel 718 on carbon steel, Addit. Manuf. 27 (2019) 540–551.

[102] Z.T. Gan, O.L. Kafka, N. Parab, C. Zhao, L.C. Fang, O. Heinonen, T. Sun, W.K. Liu, Universal scaling laws of keyhole stability and porosity in 3d printing of metals, Nat. Commun. 12 (2021).

[103] T. Mukherjee, J.S. Zuback, A. De, T. DebRoy, Printability of alloys for additive manufacturing, Sci. Rep. 6 (2016).

[104] M. Rappaz, C.A. Gandin, Probabilistic modeling of microstructure formation in solidification processes, Acta Metall. Mater. 41 (1993) 345–360.

[105] D. E. 755-2, Aluminium and aluminium alloys - Extruded rod/bar, tube and profiles – Part 2: Mechanical properties; German version EN 755- 2, 2008.

[106] K. M. B. Taminger, R. A. Hafley, Electron beam freeform fabrication: A rapid metal deposition process, in: Proceedings of the 3rd Annual Automotive Composites Conference, 2003, pp. 9–10.

[107] J. Kaufman, Introduction to Aluminum Alloys and Tempers, ASM International, 1st edition, Materials Park, OH, 2000.

[108] H. Hyer, L. Zhou, G. Benson, B. McWilliams, K. Cho, Y. Sohn, Additive manufacturing of dense WE43 mg alloy by laser powder bed fusion, Addit. Manuf. 33 (2020).

[109] P. Wang, H.Z. Zhang, H. Zhu, Q.Z. Li, M.N. Feng, Wire-arc additive manufacturing of AZ31 magnesium alloy fabricated by cold metal transfer heat source: Processing, microstructure, and mechanical behavior, J. Mater. Process. Technol. 288 (2021).

[110] X.W. Fang, J.N. Yang, S.P. Wang, C.B. Wang, K. Huang, H.N. Li, B.H. Lu, Additive manufacturing of high performance AZ31 magnesium alloy with full equiaxed grains: Microstructure, mechanical property, and electromechanical corrosion performance, J. Mater. Process. Technol. 300 (2022).

[111] K. Amato, J. Hernandez, L.E. Murr, E. Martinez, S.M. Gaytan, P.W. Shindo, S. Collins, Comparison of microstructures and properties for a Ni-base superalloy (alloy 625) fabricated by electron beam melting, Journal of Materials Science Research 1 (2012).

[112] Z.M. Wang, K. Guan, M. Gao, X.Y. Li, X.F. Chen, X.Y. Zeng, The microstructure and mechanical properties of deposited-IN718 by selective laser melting, J. Alloy. Compd. 513 (2012) 518–523.

[113] L.E. Murr, E. Martinez, S.M. Gaytan, D.A. Ramirez, B.I. Machado, P.W. Shindo, J. L. Martinez, F. Medina, J. Wooten, D. Ciscel, U. Ackelid, R.B. Wicker, Microstructural architecture, microstructures, and mechanical properties for a nickel-base superalloy fabricated by electron beam melting, Metallurgical and Materials Transactions a-Physical Metallurgy and Materials, Science 42A (2011) 3491–3508.

[114] M. Rombouts, G. Maes, M. Mertens, W. Hendrix, Laser metal deposition of Inconel 625: Microstructure and mechanical properties, J. Laser Appl. 24 (2012).

[115] C.P. Paul, P. Ganesh, S.K. Mishra, P. Bhargava, J. Negi, A.K. Nath, Investigating laser rapid manufacturing for Inconel-625 components, Opt. Laser Technol. 39 (2007) 800–805.

[116] L. Xue, M.U. Islam, Free-form laser consolidation for producing metallurgically sound and functional components, J. Laser Appl. 12 (2000) 160–165.

[117] P. Ganesh, R. Kaul, C.P. Paul, P. Tiwari, S.K. Rai, R.C. Prasad, L.M. Kukreja, Fatigue and fracture toughness characteristics of laser rapid manufactured Inconel 625 structures, Mater. Sci. Eng. A-Struct. Mater. Propert. Microstruct. Process. 527 (2010) 7490–7497.

[118] https://neutrons.ornl.gov/hfir, 2022.

[119] F. Pfeiffer, M. Bech, O. Bunk, P. Kraft, E.F. Eikenberry, C. Broennimann, C. Gruenzweig, C. David, Hard-X-ray dark-field imaging using a grating interferometer, Nat. Mater. 7 (2008) 134–137.

[120] S. Nemati, L.G. Butler, K. Ham, G.L. Knapp, C. Zeng, S. Emanet, H. Ghadimi, S. Guo, Y. Zhang, H. Bilheux, Neutron imaging of Al6061 prepared by solid-state friction stir additive manufacturing, Metals 13 (2023).

[121] J.L. Garcia-Hernandez, C.G. Garay-Reyes, I.K. Gomez-Barraza, M.A. Ruiz-Esparza-Rodriguez, E.J. Gutierrez-Castaneda, I. Estrada-Guel, M.C. Maldonado-Orozco, R. Martinez-Sanchez, Influence of plastic deformation and Cu/Mg ratio on the strengthening mechanisms and precipitation behavior of AA2024 aluminum alloys, Journal of Materials Research and Technology-JMR&T 8 (2019) 5471–5475.

[122] T. Xue, Z. Gan, S. Liao, J. Cao, Physics-embedded graph network for accelerating phase-field simulation of microstructure evolution in additive manufacturing, npj Comput. Mater. 8 (2022) 1–13.

[123] M. Tegeler, O. Shchyglo, R.D. Kamachali, A. Monas, I. Steinbach, G. Sutmann, Parallel multiphase field simulations with OpenPhase, Comput. Phys. Commun. 215 (2017) 173–187.

[124] F. Xiong, Z. Gan, J. Chen, Y. Lian, Evaluate the effect of melt pool convection on grain structure of In625 in laser melting process using experimentally validated process-structure modeling, J. Mater. Process. Technol. 303 (2022), 117538.

[125] Y. Lian, Z. Gan, C. Yu, D. Kats, W.K. Liu, G.J. Wagner, A cellular automaton finite volume method for microstructure evolution during additive manufacturing, Mater. Des. 169 (2019), 107672.

[126] T.M. Rodgers, J.D. Madison, V. Tikare, Simulation of metal additive manufacturing microstructures using kinetic Monte Carlo, Comput. Mater. Sci 135 (2017) 78–89.

[127] F. Roters, M. Diehl, P. Shanthraj, P. Eisenlohr, C. Reuber, S.L. Wong, T. Maiti, A. Ebrahimi, T. Hochrainer, H.-O. Fabritius, S. Nikolov, M. Friak, N. Fujita, N. Grilli, K.G.F. Janssens, N. Jia, P.J.J. Kok, D. Ma, F. Meier, E. Werner, M. Stricker, D. Weygand, D. Raabe, Damask – the düsseldorf advanced material simulation kit for modelling multi-physics crystal plasticity, damage, and thermal phenomena from the single crystal up to the component scale, Comput. Mater. Sci 158 (2019) 420–478.

[128] B. Eren, M.A. Guvenc, S. Mistikoglu, Artificial intelligence applications for friction stir welding: A review, Met. Mater. Int. 27 (2021) 193–219.

[129] X. Xie, J. Bennett, S. Saha, Y. Lu, J. Cao, W.K. Liu, Z. Gan, Mechanistic data-driven prediction of as-built mechanical properties in metal additive manufacturing, npj Comput. Mater. 7 (2021) 1–12.

[130] X. Qi, G. Chen, Y. Li, X. Cheng, C. Li, Applying neural-network-based machine learning to additive manufacturing: current applications, challenges, and future perspectives, Engineering 5 (2019) 721–729.

[131] C. Wang, X. Tan, S. Tor, C. Lim, Machine learning in additive manufacturing: State-of-the-art and perspectives, Addit. Manuf. 36 (2020), 101538.

[132] L. Meng, B. McWilliams, W. Jarosinski, H.-Y. Park, Y.-G. Jung, J. Lee, J. Zhang, Machine learning in additive manufacturing: a review, JOM 72 (2020) 2363–2377.

[133] Y. Han, R.J. Griffiths, Z.Y. Hang, Y. Zhu, Quantitative microstructure analysis for solid-state metal additive manufacturing via deep learning, J. Mater. Res. 35 (2020) 1936–1948.

[134] M. Mozaffar, S. Liao, X. Xie, S. Saha, C. Park, J. Cao, W.K. Liu, Z. Gan, Mechanistic artificial intelligence (mechanistic-ai) for modeling, design, and control of advanced manufacturing processes: Current state and perspectives, J. Mater. Process. Technol. 117485 (2021).

[135] R.J. Griffiths, D.T. Petersen, D. Garcia, H.Z. Yu, Additive friction stir-enabled solid-state additive manufacturing for the repair of 7075 aluminum alloy, Applied Sciences-Basel 9 (2019).

[136] R.B. Gottwald, R.J. Griffiths, D.T. Petersen, M.E.J. Perry, H.Z. Yu, Solid-state metal additive manufacturing for structural repair, Accounts of, Mater. Res. (2021).

[137] R. Raju, M. Duraiselvam, V. Petley, S. Verma, R. Rajendran, Microstructural and mechanical characterization of ti6al4v refurbished parts obtained by laser metal deposition, Mater. Sci. Eng. A-Struct. Mater. Propert. Microstruct. Process. 643 (2015) 64–71.

[138] J.M. Wilson, C. Piya, Y.C. Shin, F. Zhao, K. Ramani, Remanufacturing of turbine blades by laser direct deposition with its energy and environmental impact analysis, J. Clean. Prod. 80 (2014) 170–178.